CHAPTER 7

Lessons from deforming volcanoes

Whereas previous chapters are focused primarily on geodetic techniques, this one addresses specific applications of those techniques at a few well-studied volcanoes. Mount St. Helens, Kīlauea, Yellowstone, and Long Valley illustrate the tremendous diversity in terms of style, duration, dimensions, and mechanisms of ground movements. That is not to say that these four examples encompass the full range of deformation observed at volcanoes worldwide, or that other examples would not serve equally well. Rather, I chose these four because I know them personally, having worked at each for at least several years, and because they have been studied thoroughly with a variety of monitoring techniques, including geodesy. Therefore, the geodetic results can be placed in a rich context of other information to help interpret the processes responsible for ground deformation and other symptoms of unrest.

Geodesy provides tools for scientists to study processes as diverse as dome growth and edifice instability, over length scales of meters to kilometers, for periods of minutes to decades, across a wide spectrum of magmatic and tectonic settings. Most volcanoes, even during periods of no visible activity, are dynamic landforms that respond to magmatic, tectonic, or hydrothermal processes. Ground deformation provides a useful window into those processes that can be explored through an integrated program of geodetic monitoring. The next four sections highlight a few of the things that have been learned from geodetic investigations at four very different volcanic systems: Mount St. Helens (stratovolcano), Kīlauea (intraplate shield volcano), Yellowstone, and Long Valley (silicic calderas).

7.1 MOUNT ST. HELENS – EDIFICE INSTABILITY AND DOME GROWTH

In hindsight, the remarkable series of events at Mount St. Helens from 1980 to 1986 was not unprecedented in that volcano's relatively brief eruptive history or in the geologic records at other volcanoes, even during historical time. Nonetheless, the 1980–1986 activity at Mount St. Helens arguably had a disproportionate impact on volcanology and on the public's perceptions of volcano hazards in the USA. As a direct consequence of the Mount St. Helens experience, important strides were made during the 1980s in volcano monitoring, eruption prediction, and hazards assessment techniques. These gains have since been applied and extended during responses to numerous volcano emergencies around the world.

Geodetic measurements played an important role at Mount St. Helens, both before and after the 18 May 1980 eruption. During the pre-climactic phase, repeated EDM measurements of the famous 'bulge' tracked the growth of a cryptodome and increasing instability of the volcano's north flank. Following the explosive events of 1980, more than a dozen successful predictions of extrusive dome-growth episodes were issued on the basis of repeating patterns of ground deformation and seismicity. The following account highlights a few of the geodetic techniques used to study the 1980–1986 activity to illustrate how volcanologists were able to adapt their monitoring strategy to rapidly changing conditions at the volcano.

D. Dzurisin, *Volcano Deformation*

7.1.1 Precursory activity: the north flank 'bulge'

At 3:47 p.m. PST on 20 March 1980, an M 4.2 earthquake shook the snow-covered slopes of Mount St. Helens in southwest Washington. In hindsight, the quake was a wake-up call. More than a century of volcanic slumber was about to come to an explosive end. Many residents of the area were unaware that their 'mountain', which had not erupted in anyone's memory, was actually a volcano. But the mountain's true character was clearly recorded by its young and plentiful eruptive products, which tagged Mount St. Helens as the most active and explosive volcano in the Cascade Range. Five years earlier, United States Geological Survey (USGS) geologists Dwight R. 'Rocky' Crandell and Donal R. 'Don' Mullineaux, who had studied the volcano for nearly two decades, forecast that it would erupt again '*... within the next hundred years, perhaps even before the end of this century*' (Crandell *et al.*, 1975; Crandell and Mullineaux, 1978, p. C25).

The shallow earthquake swarm that began on 20 March 1980, and intensified during the next several days, was the first recognized precursor to the renewed volcanic activity that Rocky and Don had forecast. An electronic distance meter (EDM) network had been established on the volcano's flanks in 1972, but the bench marks lay deeply buried under snow. When the endpoints of one of the EDM lines on the east side of the volcano (Smith Creek Butte and East Dome, located 10.5 km and 3 km, respectively, from the volcano's summit) were dug out and the line length remeasured in April 1980, it was discovered that there had been virtually no change since 1972 (Figure 7.1). No tiltmeters or other continuously recording instruments to measure ground deformation had been installed at the long-dormant volcano, so any geodetic precursors to the first earthquakes, if they occurred, went unnoticed.

Within a week, however, all that was needed to recognize the profound topographic and structural changes occurring at the volcano was a keen eye. A new crater formed during the first of many phreatic eruptions and the summit area was cut by an east–west-trending system of fractures. Most telling of all, the area north of the fractures appeared to be bulging outward and possibly upward, destabilizing the volcano's north flank (Christiansen and Peterson, 1981; Lipman *et al.*, 1981a) (Figure 7.2). USGS geologists who rushed to the scene had studied mainly the active volcanoes of Hawai'i or the deposits of long-quiescent volcanoes in the Cascade Range. At Mount St. Helens, they were confronted with the unfamiliar task of monitoring a reawakening stratovolcano. Those responsible for measuring ground deformation used traditional geodetic techniques and developed a few new ones to cope with the rapidly evolving situation.

The first priority was to ascertain whether the fractures and other obvious surface disturbances in the snow-covered summit area were caused primarily by earthquake-induced ground shaking or by intense deformation of the volcano. As is often the case during volcanic emergencies, circumstances conspired to make this task difficult. Phreatic eruptions starting on 27 March and poor weather in early April prevented geodetic measurements on the upper flanks of the volcano. Unable to pursue their first priority, scientists instead did what was possible under the circumstances. They deployed two continuously recording platform tiltmeters on the lower flanks of the volcano and three more around its base. In addition, they used the mostly ice-covered surface of Spirit Lake, about 10 km north of the summit (Figure 7.1), as a large 'natural' tiltmeter and established two single-setup leveling triangles on the volcano's north flank.

Water level measurements at Spirit Lake were simple, easy to make even in bad weather, and important for determining the spatial extent and magnitude of any ground deformation that might have been occurring (Lipman *et al.*, 1981a). Inexpensive wooden yardsticks were attached to fixed objects such as tree stumps or dock piers at six sites around the lakeshore where open water was present. Water levels were read in rapid succession, typically about 20 minutes, to reduce seiche effects. Through mid-April, while ice on most of the lake served to dampen wave action, water levels could be read with a precision of 1/16 of an inch (1.6 mm). Thereafter, precise measurements could only be made at times when the lake surface was relatively calm. Any tilt of the lake basin would have been manifest as a change in differential water levels around the lakeshore. The size of the lake and precision of the measurements combined to provide a detection threshold of about 1 part in 500,000, equivalent to a tilt of 2 microradians (μrad), at a distance of 9–12 km from the volcano's summit.

The differential water level measurements at Spirit Lake revealed no significant tilts during the first critical weeks of the unrest, which meant that any deformation source was either relatively small or

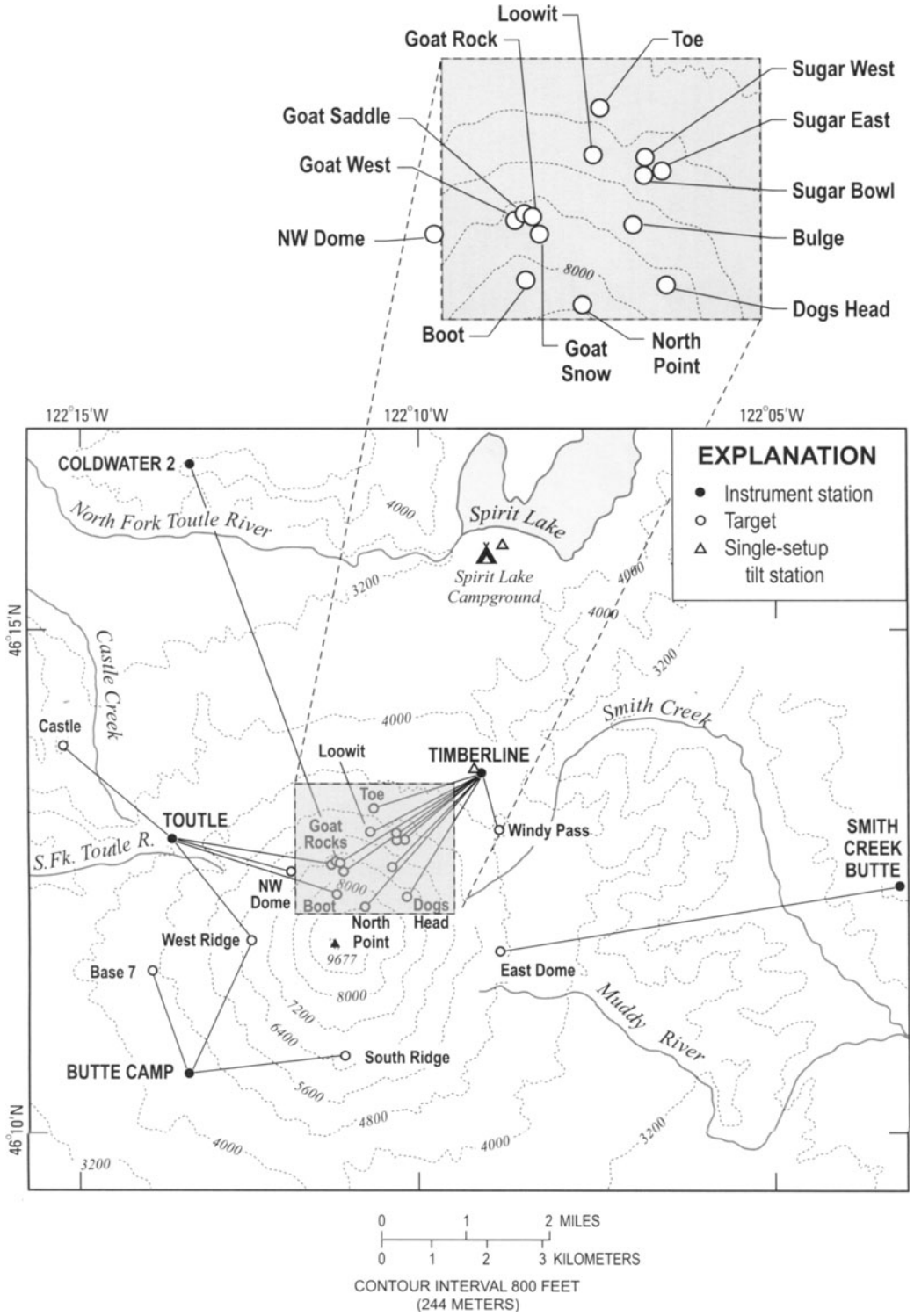

Figure 7.1. Stations used for measuring ground tilt and surface displacements at Mount St. Helens during April–May 1980 (Lipman *et al.*, 1981a). Six water-level stations (not shown) along the shore of Spirit Lake and a single-setup leveling array at Spirit Lake Campground (triangle), all 9–12 km from the summit, detected no significant tilt. Solid dots and open circles connected by lines represent places where vertical angles and slope distances were measured repeatedly using an EDM and theodolite, revealing a bulge centered near Goat Rock on the volcano's north flank. Instrument stations are shown as dots and labeled in uppercase, targets as circles and in lowercase. A single-setup leveling array at Timberline (triangle), 4 km from the summit, showed progressive tilt down to the northeast (i.e., summit uplift) and short-term, large tilt changes directed toward or away from the bulge (Figure 7.3).

Figure 7.2. Oblique aerial photograph taken on 7 April 1980, looking south at Mount St. Helens. Mount Hood, 100 km distant, is visible on the horizon at upper left. A thin layer of volcanic ash mantles fresh snow near the summit. A series of phreatic eruptions that began on 27 March 1980 deposited ash and formed the summit explosion crater seen here, which by this date had grown in diameter to about 500 m W–E and 300 m N–S. Dark streaks on the steep north flank are from fresh rockfalls. The intensely cracked 'blister' below and north of summit crater shows distension of the north flank at this early date. This feature enlarged gradually during the ensuing weeks. By 24 April, it became known as 'the bulge.'
USGS photograph by Richard B. Waitt.

shallow. In the crisis atmosphere that prevailed, this was vitally important information. If deformation was occurring beyond the disturbed summit area, it did not extend as far as Spirit Lake. Those responsible for monitoring the volcano moved closer.

Two single-setup leveling arrays (sometimes called 'dry tilt' arrays; see Yamashita, 1981, 1992; Section 2.5.2) were established in late March and early April in the parking lots of the Spirit Lake and Timberline campgrounds (Figure 7.1). The Spirit Lake array was occupied only once, because water level measurements at nearby Spirit Lake detected no significant tilting that far from the volcano. The Timberline station, on the other hand, was measured seven times between 30 March and 30 April. The results showed a generally consistent tilt of about 2 μrad day^{-1} down to the northeast (i.e., away from the summit of the volcano). The source was confirmed in various ways to be a bulge growing on the volcano's north flank.

In addition to progressive tilting away from the bulge, the measurements at Timberline revealed a remarkable pattern of short-term inflationary and deflationary tilt cycles. The first clue that such deformation might be occurring came from poor closures of the tilt-leveling array. After eliminating other possible sources of error, observers began measuring a 40-m line every few minutes for several hours. The measurements revealed that significant tilt changes were occurring over periods of a few minutes. Thereafter, a small (14 m) triangular array was used to reduce measurement errors and the time required for closure. Results showed both inflationary and deflationary tilts of as much as 50 μrad hr^{-1} directed away from or toward the center of the bulge, respectively (Figure 7.3). On 10 April, the bullseye bubble used for rough leveling of the instrument moved off level while the observers watched (Lipman *et al.*, 1981a, p. 146)!

I had a similar experience while making microgravity measurements at East Dome on the volcano's east flank. To my amazement, the meter's level bubbles moved well off center in a direction suggesting inflation several seconds before the start of a phreatic eruption in the summit area. By the time the

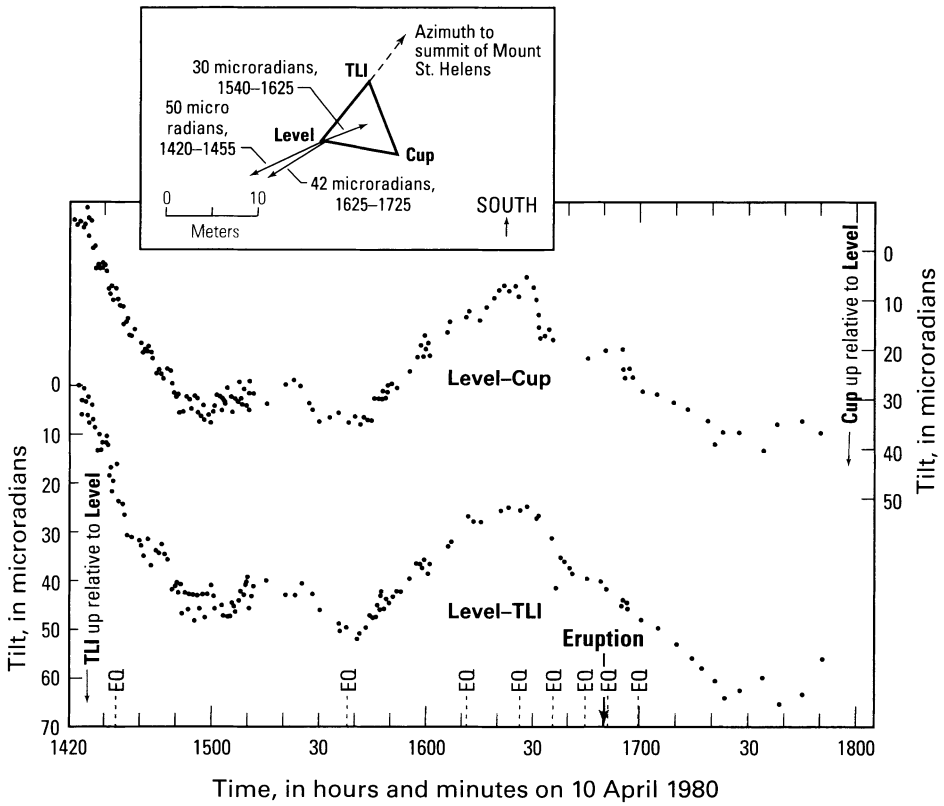

Figure 7.3. Short-term tilt fluctuations measured by single-setup leveling at Timberline, on the northeast flank of Mount St. Helens, from 14:20–17:50 PST on 10 April 1980 (Lipman *et al.* 1981a). Tilt vectors (*inset*) derived from elevation changes at TLI and Cup relative to Level. Vectors point toward or away from the center of a bulge growing on the volcano's north flank. Occurrences of felt earthquakes (EQ) and a phreatic eruption (Eruption) are also noted on the time axis. No consistent relationship was recognized among tilt changes, earthquakes, and eruptions.

eruption waned a few minutes later, the inflation episode was over and the bubbles were centered again. It was an adrenaline-charged experience that I'll never forget. Everyone who works near active volcanoes develops a personal threshold of acceptable risk. Maybe we were lucky that day on East Dome and on many subsequent occasions, but we were never capricious. Each of us assessed the risks and rewards as we understood them and made deliberate decisions about how to proceed within the boundaries established by those in charge. We did not always agree, but we respected each other's right to decide and act accordingly.

The source of the short-term tilt fluctuations at Mount St. Helens remains unclear even to this day. One plausible explanation is that they reflected pressurization–depressurization cycles in a shallow hydrothermal system driven by the intrusion of a cryptodome. The timing of inflation immediately before some of the phreatic eruptions, followed by deflation during the eruptions, supports this hypothesis. On the other hand, this pattern was not observed consistently and the orientation of short-term tilt vectors toward or away from the center of the bulge, rather than the summit area, suggests that the tilts might instead have been caused by jerky movement of magma intruding beneath the bulge (Lipman *et al.*, 1981a, p. 146).

Five continuously recording tiltmeters were installed around Mount St. Helens during late April and early May 1980 at distances of 3–15 km from the summit (Dvorak *et al.*, 1981). The biaxial, platform-type instruments, with ~0.1-μrad resolution, were secured with expansion bolts to cast-concrete base plates that were cemented to rock outcrops. Surface installations are quick and can be useful during a crisis or where ground tilts are large and rapid, but they are subject to large diurnal fluctuations and other noise sources that limit their effectiveness in most situations (Dzurisin, 1992a). At Mount St. Helens, they provided important information about ground deformation on a continuous

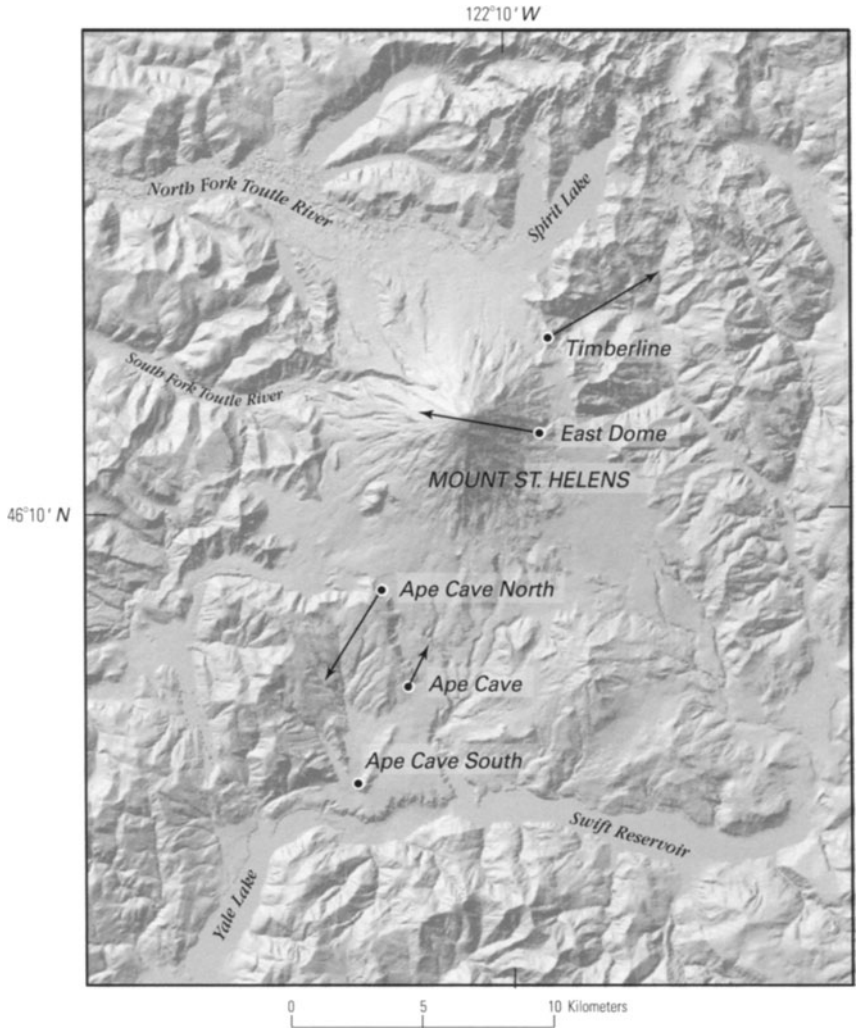

Figure 7.4. Locations of electronic tiltmeters around Mount St. Helens prior to the landslide and eruption of 18 May 1980, and net ground-tilt vectors for the period from 6 May to 18 May 1980 (Dvorak *et al.*, 1981). Tilt changes are represented by arrows that point away from an uplift source or toward a subsidence source. In this case, the Timberline and Ape Cave North stations tilted away from the summit area, while the East Dome station tilted toward it. Tilt changes at the Ape Cave and Ape Cave South stations were small enough to be considered not statistically significant. Dvorak *et al.* (1981) interpreted these trends as a general inflation of the volcano plus formation of a graben across the summit area, the latter to explain the East Dome result.

basis, including times when other geodetic observations were impossible owing to darkness or poor weather.

Two of the three tiltmeters within 6 km of the summit recorded net inflationary trends (i.e., points closer to the volcano moved up relative to points farther away) from the time they were installed until the onset of the eruption on 18 May (Figure 7.4). The third, at East Dome on the volcano's east flank, recorded an apparent deflationary trend of approximately the same magnitude (10–15 μrad). Two tiltmeters located more than 6 km from the summit recorded only minor tilt changes. In hindsight, Dvorak *et al.* (1981) attributed this tilt pattern to a general inflation of the volcano plus formation of an east–west-trending graben across the summit area. Unfortunately, the data are too sparse to convincingly test this idea or distinguish among alternative models. Imagine the frustration felt by scientists in the midst of the crisis, when the volcano was often shrouded in clouds and the tiltmeters were telling an ambiguous story.

The tiltmeter results at Mount St. Helens emphasize the need for as much geodetic information as possible during a volcanic crisis (Chapter 11). The

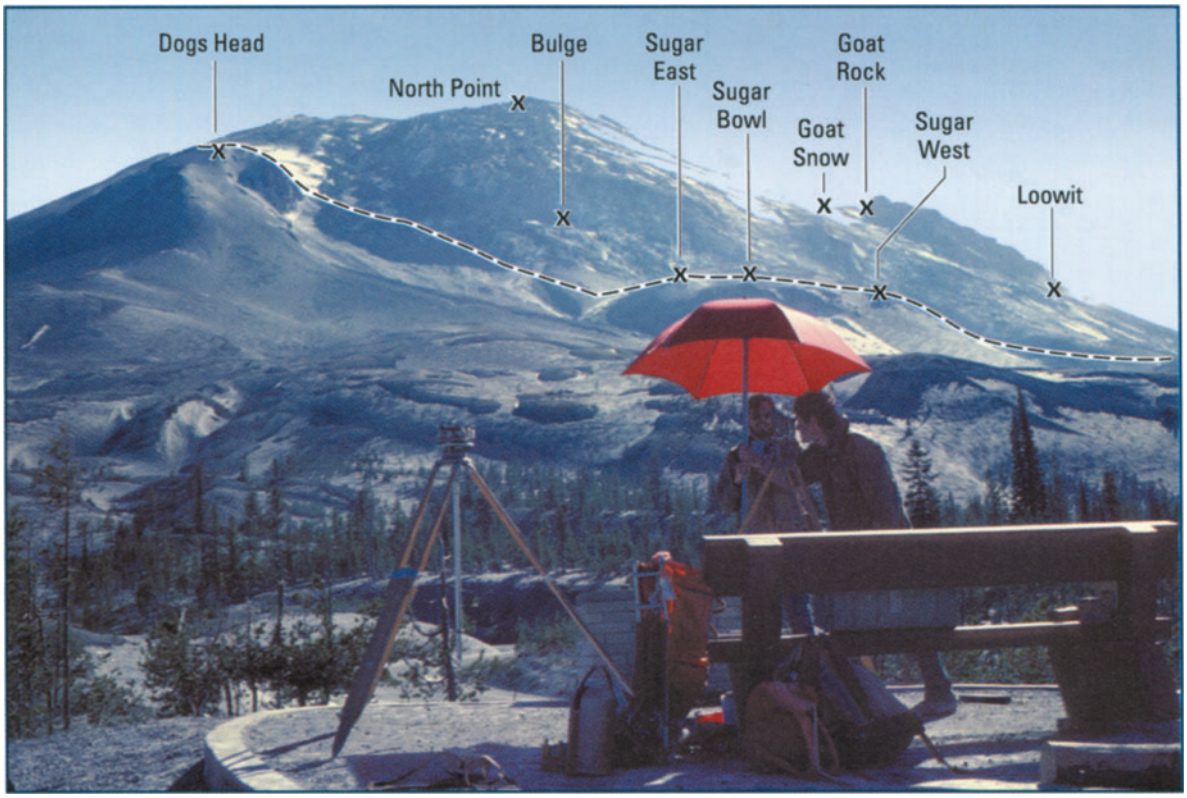

Figure 7.5. Timberline theodolite and EDM station on 1 May 1980 (Lipman *et al.*, 1981a). Named features are sites of fixed reflectors. Dashed line indicates approximate limits of the deforming bulge and of rock subsequently removed during the 18 May debris avalanche and lateral volcanic blast.
USGS photograph by P.W. Lipman.

surface deformation field is likely to be complex in both space and time, especially if more than one deformation source is involved (e.g., an inflating magma reservoir, opening dike, pressurizing or depressurizing hydrothermal system, or slipping faults). To distinguish among these possibilities with any real confidence, the spatial and temporal evolution of the deformation field must be known in considerable detail. This is especially difficult during a rapidly evolving crisis, when hazards to field personnel and limited resources must also be considered. Scientists facing this dilemma at Mount St. Helens during the spring of 1980 did what they could under trying circumstances, with generally good results.

The most revealing geodetic dataset during the two-month precursory period from 20 March to 18 May came from repeated measurements of horizontal angles, vertical angles, and slope distances among an array of bench marks on the flanks of the volcano and around its base (Lipman *et al.*, 1981a). Every 1–3 days, weather permitting, theodolite and EDM measurements were made from 5 instrument stations around the volcano to as many as 19 fixed targets on the edifice (Figures 7.1 and 7.5). The data were combined to calculate displacement vectors for the targets relative to the instrument stations.

The geodetic results were alarming. From 23 April through the early morning of 18 May, several targets located within an elliptical area about 1.5 km × 2.0 km in size were observed to move steadily northward at rates of 1.5–2.5 m day^{-1} (Figures 7.6–7.9). The movements were subhorizontal, indicating that the deforming area was not simply sliding downslope under the influence of gravity, but rather was being forced laterally outward by intrusion of a cryptodome (Figure 7.10). Stations outside the rapidly deforming area, including Dogs Head, East Dome, South Ridge, and West Ridge, were remarkably stable. Especially notable were the results from East Dome, which was first measured from Smith Creek Butte in 1972. No significant changes were observed during re-occupations of that line on 10

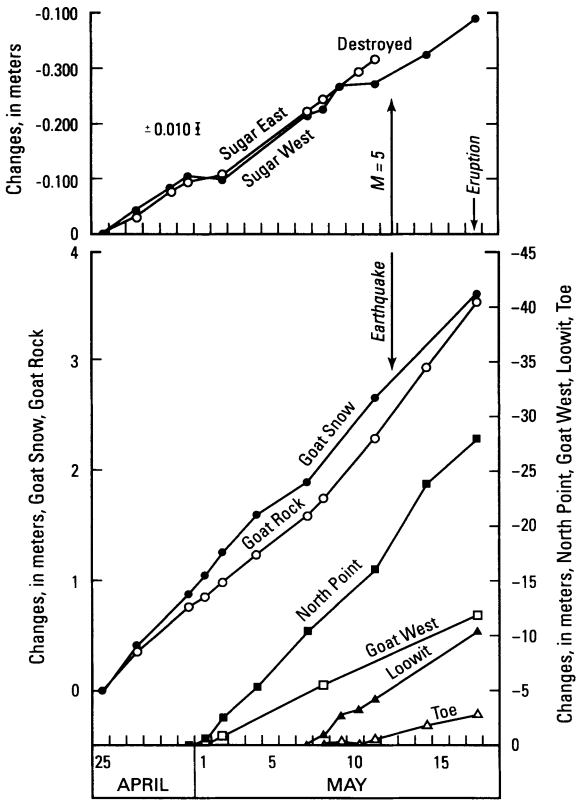

Figure 7.6. Slope-distance changes between two instrument stations and several targets on the bulge measured with an EDM, 25 April to 18 May 1980 (Lipman *et al.*, 1981a). Goat West was measured from Toutle, all others from Timberline. See Figure 7.1 for locations.

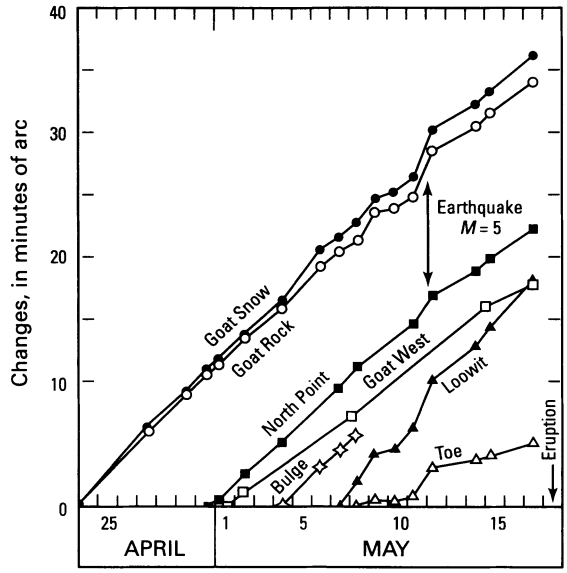

Figure 7.7. Horizontal-angle changes to several points on the bulge measured by theodolite, 23 April to 18 May 1980 (Lipman *et al.*, 1981a). Goat West and Bulge targets were measured from Toutle, all other targets from Timberline. See Figure 7.1 for instrument and target locations.

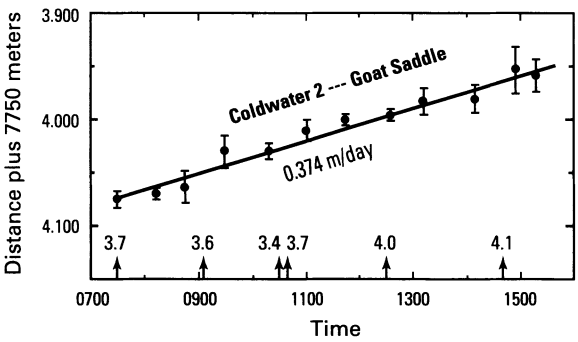

Figure 7.8. Changes in slope distance between Coldwater 2 and Goat Saddle (Figure 7.1) measured with an EDM for approximately 8 hours on 4 May 1980 (Lipman *et al.*, 1981a). Error bars indicate spread among measurements at three different frequencies. Arrows indicate times of earthquakes under Mount St. Helens with magnitudes greater than 3.5. The deformation rate increased from about 0.4 m day^{-1} on 4 May to an average of 1.4 m day^{-1} between 4 May and 16 May, and then slowed to about 0.5 m day^{-1} until the landslide and eruption on 18 May.

April, 25 April, or even after the 18 May eruption (Lipman *et al.*, 1981a). The significance of this null result is explored further in Chapter 11.

By mid-May 1980, the increasing instability of the north flank was apparent to all concerned, prompting the question: What would be the outcome, and when? The geologic record at Mount St. Helens included deposits from numerous plinian eruptions in the past few thousand years, so a vertically directed explosive eruption seemed the most likely scenario. The volcano had also produced several young dacite domes, including an amalgamation of domes called the Summit Dome that comprised the upper third of the edifice. Given the compelling evidence for a cryptodome actively growing beneath the bulge, a relatively non-explosive dome-building eruption was also a distinct possibility. Outcomes regarded as less likely included the extrusion of a lava flow, like those exposed in several places on the volcano's flanks, or a debris avalanche triggered by failure of the north flank. Ironically, no evidence for previous large debris avalanches at Mount St. Helens was exposed at the volcano until the crater that formed on 18 May 1980, was eroded by subsequent lahars and seasonal stream flow. Only then were deposits from two earlier debris avalanches exposed for study (Hausback and Swanson, 1990). Of course, another possible scenario was that the 1980 unrest would simply stop

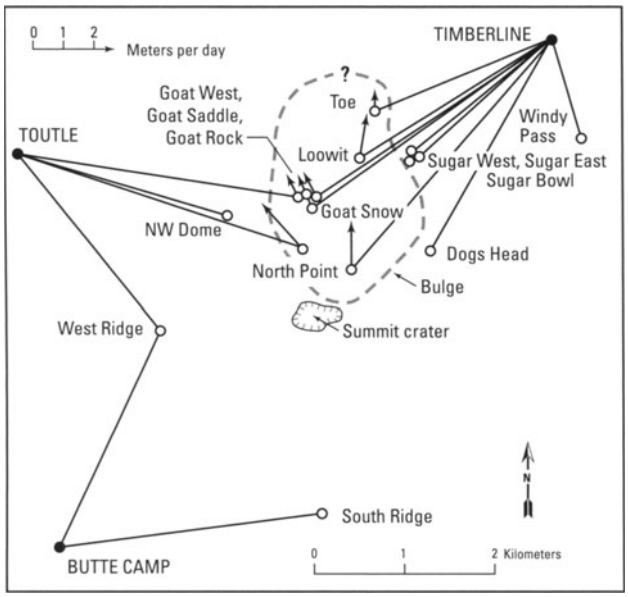

Figure 7.9. Typical daily displacement vectors in the area of the bulge on the north flank of Mount St. Helens during the first half of May 1980 (Lipman *et al.*, 1981a). Instrument stations are in uppercase, targets in lowercase. Targets without vectors showed displacements too small to plot. Dashed line represents approximate limit of the bulge.

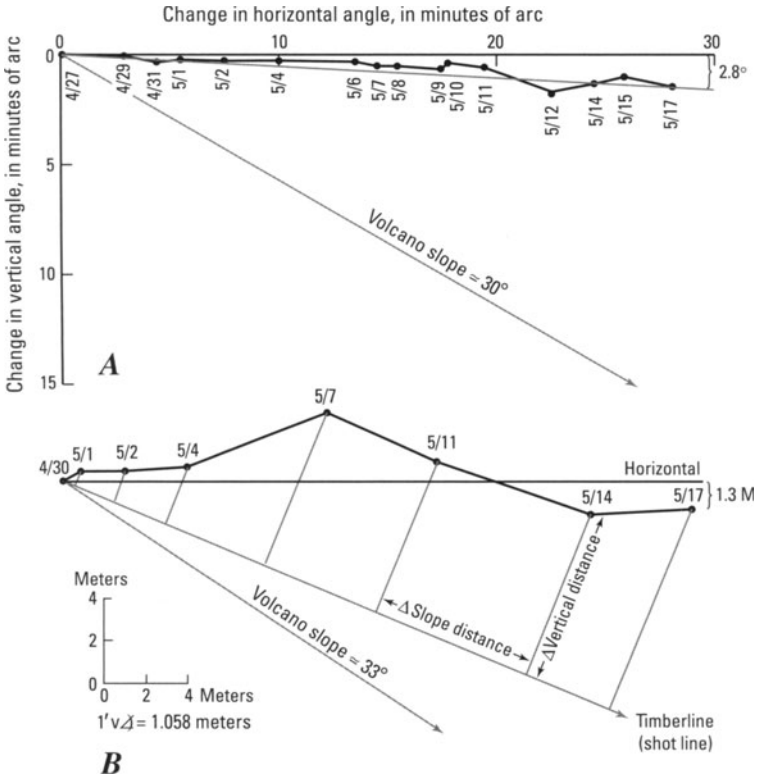

Figure 7.10. Vertical changes at stations Goat Rock and North Point (Lipman *et al.*, 1981a). (A) Changes in vertical angle versus changes in horizontal angle for Goat Rock from 27 April to 17 May. Average local slope of the volcano near the target is about 30°, much steeper than the displacement vector. (B) Vertical angle versus slope distance for the North Point target from 30 April to 17 May. For each measurement interval, the change in slope distance is scaled along the shot line, and the change in vertical angle is converted into a length (1 minute vertical angle = 1.058 m for the 3.65 km line) and plotted perpendicular to the shot line. Again, the average volcano slope is much steeper than the displacement vector. Therefore, points on the bulging north flank were being shoved outward, in hindsight by a growing cryptodome, not merely sliding downslope under the influence of gravity.

and the volcano would resume its century long slumber.

Aware as they were of these diverse possibilities and of the increasing hazard to observers near the volcano, scientists wrestled with the conflicting requirements for personal safety and better information about what was happening. No single source of geodetic data was sufficient to adequately monitor the rapidly evolving situation, so in addition to the continuously recording tiltmeters, microgravity and EDM–theodolite surveys were continued through 9 May and the morning of 18 May, respectively. EDM measurements from Coldwater 2 to Goat Rock on 16 and 17 May, and at 6:53 a.m. PDT on 18 May showed that the deformation rate slowed from an average of 1.4 m day^{-1} from 4 May to 16 May to 0.5 m day^{-1} from 16 May to the last measurement an hour and a half before the north flank failed catastrophically at 8:32 a.m. PDT on 18 May.

Faced with the same situation today, observers might try to install continuously recording tiltmeters, strainmeters, and Global Positioning System (GPS) receivers on the bulge as a substitute for geodetic surveys that require field personnel to go repeatedly in harm's way. At Mount St. Helens in 1980, the window during which such installations would have been possible in relative safety, as determined by weather and activity at the volcano, was very narrow. Less than two weeks elapsed between the onset of unusual seismicity beneath the volcano (15 March) and the first phreatic eruption (27 March). Theory suggests that deformation of the bulge might have accelerated rapidly in the final minutes before failure of the north flank, but there is no evidence for this in the distal tiltmeter records. The use of radar interferometry to study the bulge would have been hindered by coherence loss caused by the spring snow pack and by the relatively long orbital repeat cycles of present-day radar satellites. Even in hindsight and with the benefit two more decades of geodetic sophistication and experience, obtaining this critical piece of information without exposing field crews to substantial risk would have been difficult at best. A solution to a similar dilemma emerged in 2004 – in the form of a 'spider' – during another period of intense surface deformation at Mount St. Helens (Section 11.3.4).

A lesson to be learned from the 1980 experience is that geodetic monitoring of dangerous volcanoes is best accomplished by installing continuously recording instruments at key sites as early and robustly as possible, in order to minimize subsequent visits when conditions might be more hazardous. If the unrest persists for several months, aerial photogrammetry or satellite radar interferometry can sometimes provide additional information without exposing field crews to the restless volcano. On the other hand, even as continuous monitoring and remote-sensing techniques continue to improve, trained observers are essential to provide context, analysis, and an assessment of the hazards.

7.1.2 Monitoring and predicting the growth of a lava dome

Another example that illustrates the importance of adapting geodetic monitoring techniques to changing volcanic conditions is the case of episodic dome growth at Mount St. Helens from 1980 to 1986. Following the catastrophic debris avalanche and eruption on 18 May, five smaller explosive eruptions occurred between 25 May and 18 October 1980 (Christiansen and Peterson, 1981). Dacite domes were emplaced on the floor of the 18 May crater in the waning stages of three of those eruptions, but the first two domes were mostly destroyed by subsequent explosive eruptions. The October 1980 dome survived as the core of the 1980s dome, which developed during a series of exogenous and endogenous growth episodes that ended in October 1986 (Swanson *et al.*, 1987).[1] Each of these episodes was successfully predicted tens of minutes to three weeks in advance, on the basis of a recurring pattern of seismicity and ground deformation in the crater and eventually on the dome itself.

A key ingredient for each of the successful predictions at Mount St. Helens was seismic monitoring that allowed the recognition of three main types of seismicity: (1) tectonic-like earthquakes with focal depths greater than 4 km beneath the volcano or at any depth away from the volcano, which produced high-frequency impulsive arrivals (i.e., volcano–tectonic (VT) earthquakes); (2) earthquakes at depths of less than 3 km beneath the dome, which produced medium- to low-frequency arrivals (including long-period (LP) earthquakes); and (3) surface events including rockfalls and gas bursts from the dome with complicated signatures and generally emergent onsets (Malone *et al.*, 1983).

The second and third types of seismicity were most

[1] A prolonged dome-building eruption at Mount St. Helens that began in September–October 2004 produced another dacite dome immediately south of the 1980s dome (Dzurisin *et al.*, 2005). The eruption was continuing in March 2006.

diagnostic of impending dome-growth episodes over periods of a few days to weeks. Typically, both the number of shallow earthquakes and the rate of seismic energy release increased progressively for several days to four weeks before dome-building episodes. A sudden pronounced increase in the occurrence of shallow quakes, usually a few hours before the onset of exogenous dome growth, was a reliable short-term indicator of impending activity. After magma reached the surface, shallow earthquakes essentially stopped and surface events dominated the seismic records. In some cases, when the onset of exogenous growth was unobserved owing to darkness or poor weather, the marked change from intense shallow earthquake activity to mostly rockfall activity was the only basis for concluding that magma had reached the surface and an eruption was underway (Malone *et al.*, 1983).

The pattern of seismic activity varied from episode to episode, partly as a result of the changing morphology of the dome. Endogenous growth became more prevalent as the dome grew larger; thus, in some cases, rockfalls from the dome increased dramatically several days before magma eventually appeared at the surface. Another factor that affected the timing and intensity of rockfall activity was the changing stability of the outer parts of the dome. Growth episodes that began when parts of the dome were gravitationally unstable, as was the case for some extrusive lobes that were perched on steep slopes and for large cliffs that formed on the dome as a result of intense deformation, were characterized by earlier and more intense rockfalls.

Now let us consider the geodetic data, which takes several forms. Electronic tiltmeters placed on the crater floor near the dome or on the dome itself were one source of useful information. Near-surface installations with detection thresholds of a few to several tens of microradians were adequate to monitor tilt changes within a few hundred meters of the dome starting several weeks before each growth episode (Dzurisin *et al.*, 1983) (Figure 7.11). Tilting was generally outward from the dome and started to accelerate rapidly a few hours to several days before the start of exogenous growth. The tilt direction often was affected by nearby cracks or faults, but typically reversed sharply from outward (i.e., away from the center of the dome) to inward several minutes to hours before magma reached the surface (Figure 7.12). These reversals may have reflected the combined effects of depressurization within the dome and increased surface loading as

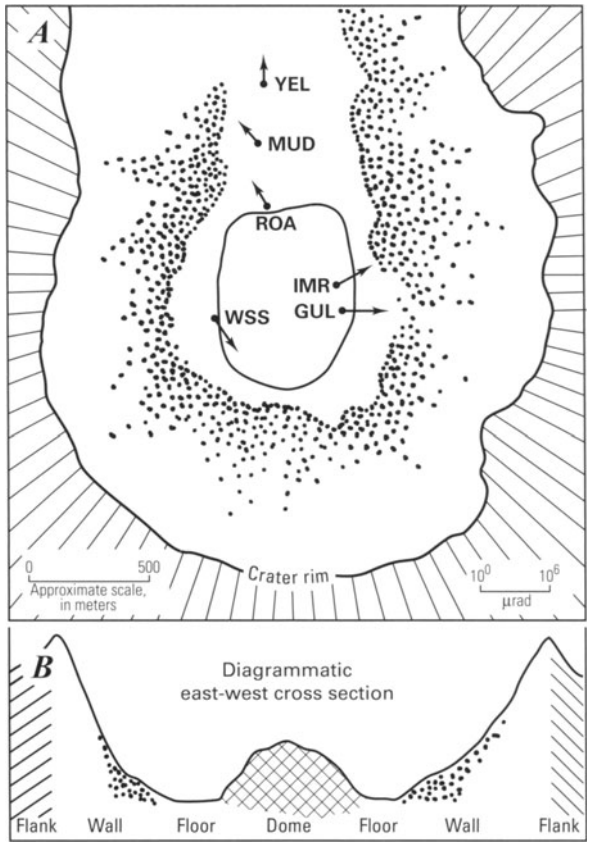

Figure 7.11. Sketch map of the 1980 crater and lava dome at Mount St. Helens (A) showing the locations of electronic tiltmeters from May 1981 to May 1982, and diagrammatic east--west cross section (B) (Dzurisin *et al.*, 1983). Net tilt vectors for periods that culminated in eruptions (i.e., dome growth episodes) are shown on a logarithmic scale to accommodate very large changes at some stations. Not all tiltmeters operated simultaneously; all were eventually destroyed by rockfalls or eruptive activity. Vectors for several periods are shown together to illustrate the typical pre-eruption pattern of tilting outward from the dome. Tilt data are for the following intervals: IMR, 29 May to 23 June 1981; GUL, 3 July to 6 September 1981; YEL, MUD, and ROA, 13 October to 31 December 1981; WSS, 29 April to 15 May 1982.

magma broke through to the surface and moved onto the exterior of the dome.

One of the more effective geodetic monitoring instruments used to predict dome-building eruptions at Mount St. Helens was decidedly low-tech (i.e., a common steel tape measure). Observers noted that the crater floor surrounding the dome often became cracked and wrinkled several weeks before dome-building eruptions (Figure 2.15). The cracks, which were mostly radial to the dome, were caused by uplift and extension of the crater floor as magma rose in the feeder conduit beneath the dome. The 'wrinkles' were shallow thrust faults that formed because the crater floor was being shoved outward against the

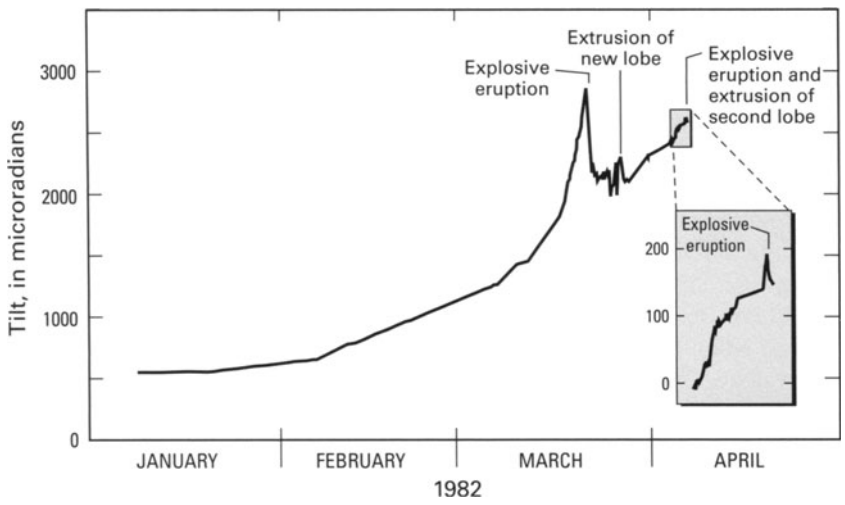

Figure 7.12. Tiltmeter data from station ROA (see Figure 7.11) for the period January–April 1982, which included an explosive eruption and lahar on 19 March, extrusion of a small lobe onto the lava dome during 20–24 March, and smaller explosions and extrusive of a second lobe during 5–10 April (Dzurisin *et al.*, 1983). Detectable radial uplift began in mid-January and accelerated sharply on 16 March. Rapid subsidence started 30 minutes before the 19 March explosion. Uplift resumed in late March and again reversed to subsidence 36 hours before extrusion resumed on 5 April (*inset*).

relatively rigid crater walls. To monitor the development of these features, observers needed to measure relative movements of up to several meters over timescales of several weeks. Risking expensive sensors was futile, because they were likely to be damaged or buried by frequent rockfalls from the growing dome or encircling crater walls. Experience showed that the survivability of equipment left in this dynamic, hazardous environment was measured in weeks to a few months at best.

The solution was both simple and elegant. Short sections of steel rebar or fence posts were driven into the crater floor to serve as markers, and the distances among them were measured periodically with a steel tape. A typical monitoring station consisted of one or two markers on each side of a developing crack or thrust fault (Figures 2.13–2.15). Taping required only two observers, who could visit several stations on foot in just a few hours. As a crack widened, the taped distance across it increased, usually in a regular and accelerating pattern. Conversely, as the upper plate of a thrust over-rode the lower, the distance between points on opposite sides of the fault decreased. Extrapolation of these trends helped to define a predictive window during which the eruption was expected to begin, in some cases as much as 2–3 weeks in advance (Figure 2.16).

Similar data were obtained using a different technique that partly avoided the problem caused by thick accumulations of snow on the crater floor during the winter. In this case, slope distances between a few instrument stations on the crater floor and several fixed targets on the flanks of the dome were measured repeatedly with an EDM. As the dome swelled prior to the start of exogenous growth, the data revealed a pattern of slope-distance contraction very similar to that already described for thrust faults on the crater floor (Figure 7.13). Based primarily on the combination of seismic, tiltmeter, thrust-fault, and slope-distance data, the onset of each exogenous growth episode at Mount St. Helens from December 1980 to October 1986 was successfully predicted a few days to three weeks in advance (Figure 7.14). In some cases, the prediction window was narrowed to just a few days (several days before the start of the eruption).

My point in describing the geodetic techniques used to predict dome-building eruptions at Mount

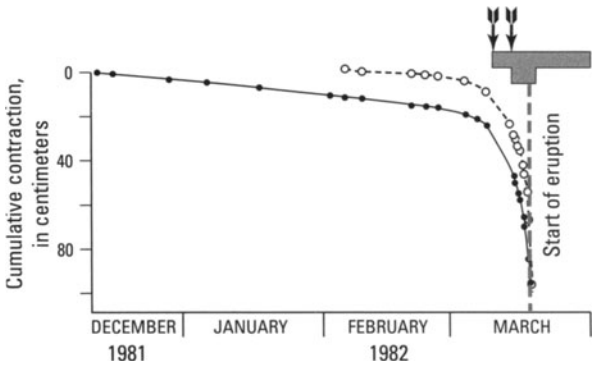

Figure 7.13. Cumulative contraction of slope distances between two points on the lava dome and a relatively stable point on the crater floor before the eruption of March–April 1982 (Swanson *et al.*, 1983). Left arrow indicates the date on which the USGS David A. Johnston Cascades Volcano Observatory (CVO) first issued an eruption prediction, and upper shaded box indicates the time window in which the eruption was predicted to occur (i.e., one to three weeks after the prediction was issued). An updated prediction with a shorter window was issued 3 days after the initial prediction, as indicated by the right arrow and lower box. Dashed line represents the start of the eruption on 19 March 1982.

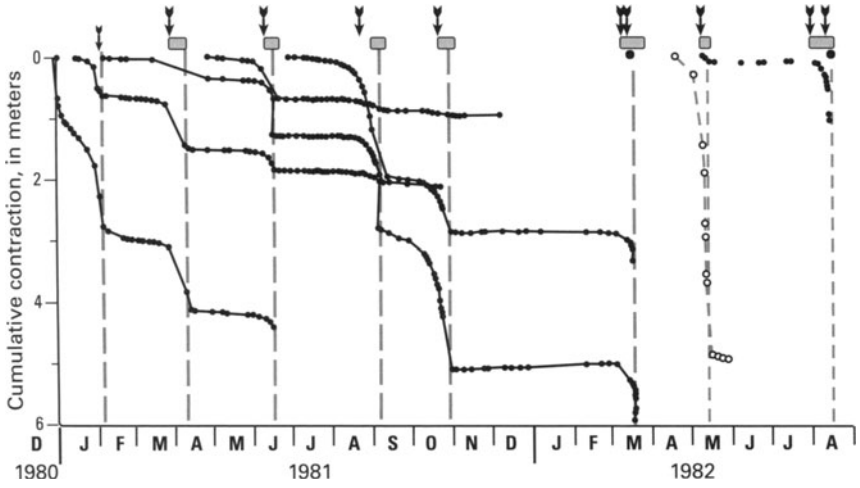

Figure 7.14. Summary of displacement data for thrust faults (solid circles) and a slope distance from the crater floor to the flank of the dome (open circles). Also shown is the timing of predictions and dome-building eruptions from late December 1980 to August 1982 (Swanson *et al.*, 1983). Symbols are as in Figure 7.13.

St. Helens is not to imply that exactly the same approach should be applied at other volcanoes with growing domes. In fact, success at Mount St. Helens depended on a favorable combination of uncommon factors (i.e., a repetitive process acting on viscous magma beneath a relatively open, easily accessible vent area, where substantial resources could be committed to volcano monitoring (Swanson *et al.*, 1983). Rather, I have included this example to illustrate the importance of frequent visits to a restless volcano by trained observers, and of adapting an effective monitoring strategy to the specific situation at hand. Considerable standardization of monitoring equipment and strategy is not only possible but also desirable, as evidenced by the experience of the USGS–USAID (US Agency for International Development) Volcano Disaster Assistance Program (VDAP) during numerous volcano-emergency responses since the program's inception in 1986 (Murray *et al.*, 1996a). Nonetheless, experience also shows that searching out special opportunities, such as the rapidly developing thrust faults at Mount St. Helens, and then finding innovative ways to take advantage of those opportunities, is sometimes key to a more effective monitoring strategy. In the words of a scientist who played a key role in monitoring and predicting eruptions at Mount St. Helens during the 1980s: '*Field observations go hand in hand with more sophisticated equipment and techniques to form a complete system for monitoring volcanoes. Monitoring programs should explicitly include provisions for geologic field observations and instill in field workers, scientists and technicians alike, the need to be flexible and clever in designing simple experiments and measurements to test important field observations on the spot.*' (Swanson, 1992, p. 219).

Mount St. Helens had more lessons to teach during an 18-year eruptive hiatus from October 1986 to September 2004, and especially during an extended period of new dome growth that began in October 2004. The story through early 2006 is told in Section 11.3.4.

7.2 KĪLAUEA VOLCANO, HAWAI′I – FLANK INSTABILITY AND GIGANTIC LANDSLIDES

7.2.1 The volcano's mobile south flank: Historical activity

The largest earthquake (M 7.2) in more than a century shook the Big Island of Hawai′i at 4:48 a.m. HST on 29 November 1975 (Tilling *et al.*, 1976; Ando, 1979; Lipman *et al.*, 1985). Most residents were accustomed to feeling small earthquakes during normal background activity at Kīlauea and Mauna Loa volcanoes, and many also had experienced moderate shocks (M 5–6.5) that occur beneath the island once every decade or so. But that morning's shaking was much worse than anything in recent memory. Not since 1868 had the ground heaved so hard and so long. In both 1868 and 1975, a local tsunami, meter-scale subsidence of the island's south coast, and an eruption of Kīlauea accompanied the intense shaking. What could possibly explain this recurring pattern of large earthquakes, coastal subsidence, and eruptions?

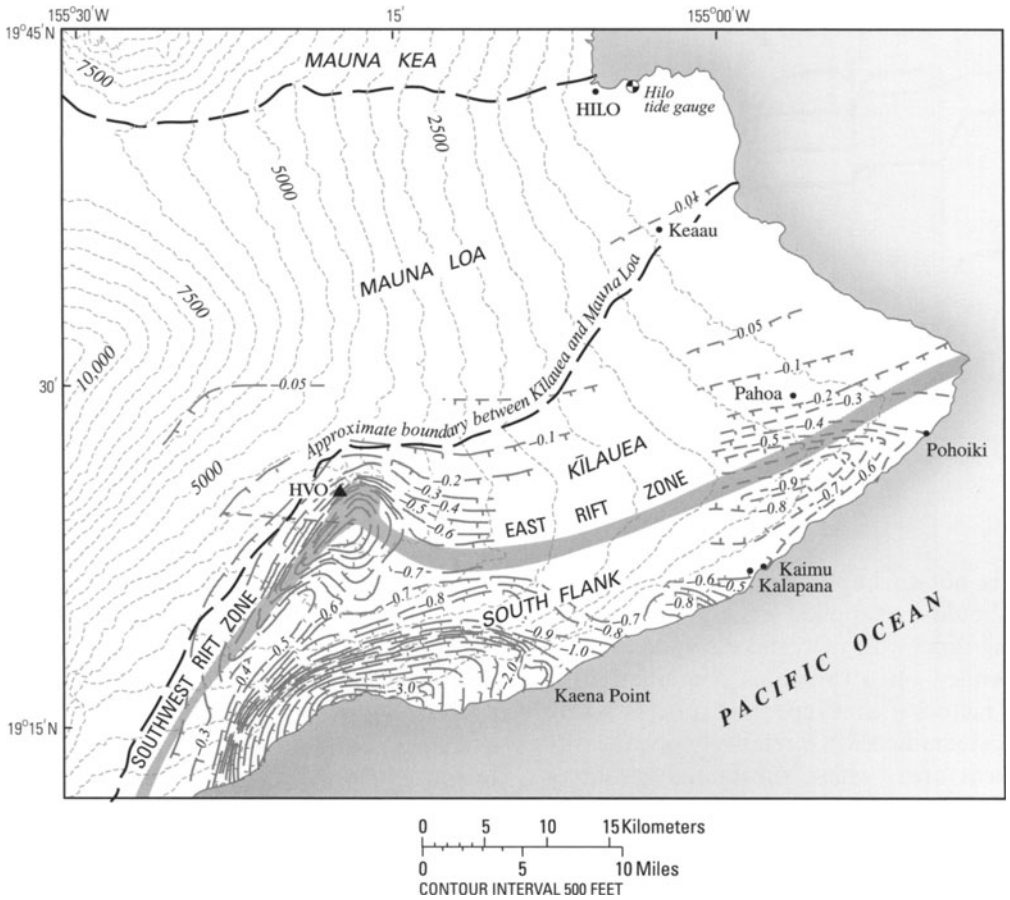

Figure 7.15. Interpreted contours of elevation changes (meters) associated with the *M* 7.2 Kalapana earthquake of 29 November 1975, based on repeated leveling surveys and coastal subsidence measurements (Lipman *et al.*, 1985). Rift zones and summit caldera are indicated by shaded pattern. Hachures show direction of relative movement.

Thanks in large part to a program of geodetic measurements by staff members of the USGS Hawaiian Volcano Observatory (HVO) dating back to 1912, we now understand that events like those in 1868 and 1975 occur when part of the gravitationally unstable south flank of Kīlauea or Mauna Loa slips and lurches toward the sea. Repeated measurements, especially EDM and leveling surveys, reveal a striking pattern of downward and seaward movements by up to several meters during the 1975 event (Figures 7.15 and 7.16). The sudden movements produce a tsunami where the coastline plunges seaward and extension across the summit area, which facilitates movement of stored magma toward the surface. Geodesy has played a key role in advancing our understanding of such events in Hawai'i and at many other island volcanoes around the world.

Even a cursory examination of the topography and structure of the Big Island of Hawai'i reveals the potentially unstable nature of Kīlauea's south flank, especially in light of the recent discovery of extensive landslide deposits surrounding many of the Hawaiian Islands (Figure 7.17). Dominating the skyline to the northwest is the massive edifice of Mauna Loa Volcano, the largest on the island. The buttressing effect of giant Mauna Loa on Kīlauea, its diminutive neighbor to the southeast, has long been recognized. Separating the two volcanoes is the Kaoiki seismic zone (Figure 7.18(B)) and fault system, a group of normal faults downthrown mainly to the southeast. Running sub-parallel to the boundary between the volcanoes are Kīlauea's two rift zones, the East Rift Zone and Southwest Rift Zone. Southeast and downslope from the rift zones is the Hilina fault system (Figures 7.18(A) and 7.25), another group of young normal faults downthrown mainly to the southeast. Seen from this perspective, the south flank appears to be clinging precariously to the rest of the island, separated from its bulk by two active fault systems and two active rift zones. The combined forces of gravity and magmatic intrusion along the rift zones have the effect of pulling and

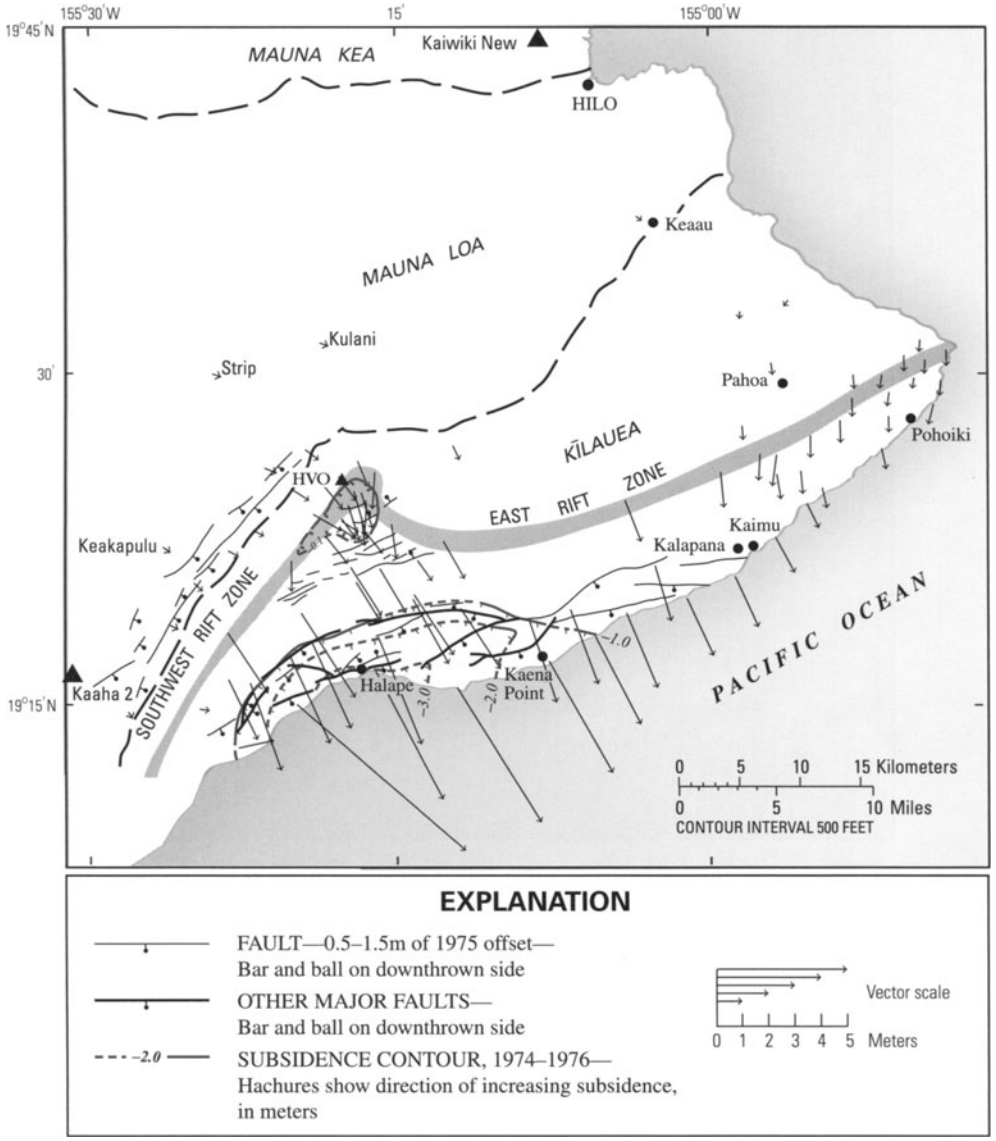

Figure 7.16. Horizontal displacements associated with the 1975 *M* 7.2 Kalapana earthquake derived from trilateration surveys in fall 1974 and spring 1976 (Lipman *et al.*, 1985). Arrow tails are at marks; lengths of arrows indicate amounts of displacement. Stations Kaaha 2 and Kaiwiki New (triangles) were assumed fixed. Solid dots (e.g., Hilo, Keaau) mark named geographic features or towns.

shoving the south flank toward the sea. Not surprisingly, seismic and geodetic data confirm the mobility of the south flank and suggest the possibility of future catastrophic collapse. Confirmation that such collapses have occurred in the recent geologic past involved contributions from geodesy, geology, and undersea exploration (e.g., Takahashi *et al.*, 2002) over the course of two decades, and makes for a compelling geologic detective story.

A strong clue that the south flank of Kīlauea is, in fact, moving seaward comes from a striking pattern of earthquakes beneath it. In plan view, the epicenters of most earthquakes at Kīlauea in the depth range 2–4 km correspond closely to the seismically active portions of the volcano's two rift zones (Figure 7.18(A)). Most of these earthquakes occur during swarms caused by lateral intrusion of basaltic magma along a rift zone from a reservoir beneath the summit area. At depths of 5–10 km, the pattern is distinctly different: most of these earthquakes occur not along the rift zones but beneath the volcano's south flank (Figure 7.18(B)). Viewed in cross section, the significance of this pattern is more apparent (Figure 7.19(A) and (B)). Earthquakes in the depth range 10–40 km clearly outline a vertical conduit system that delivers basaltic magma from

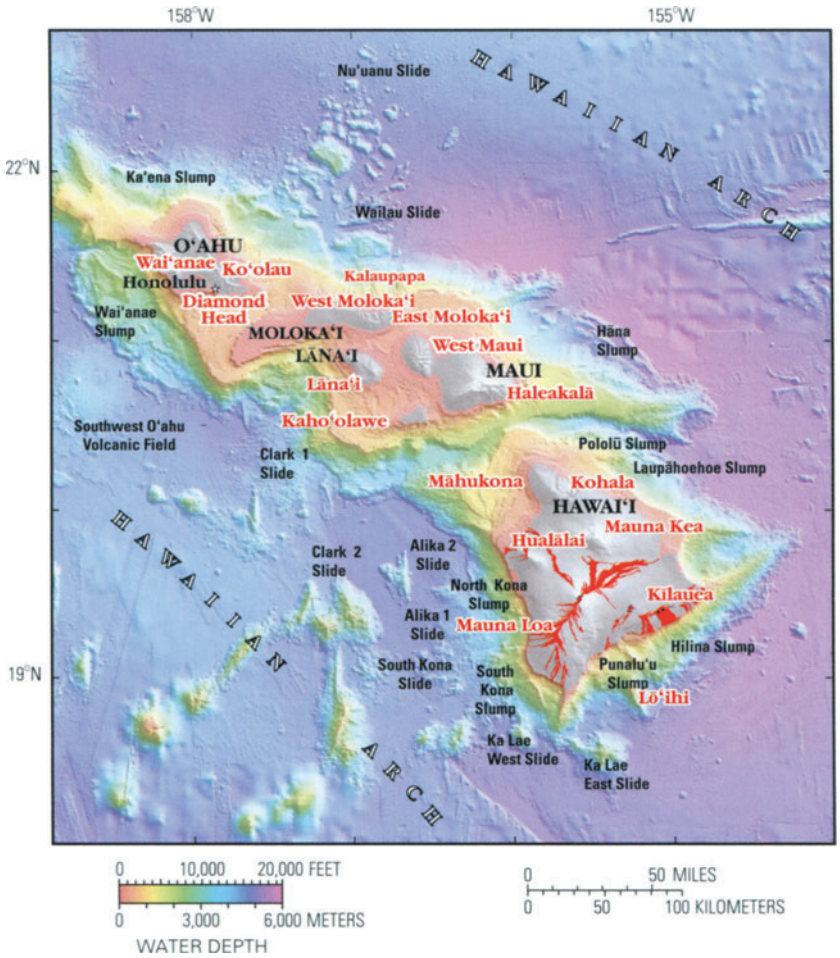

Figure 7.17. Shaded relief and bathymetry of the major Hawaiian Islands from Eakins *et al.* (2003). The islands are surrounded by deposits from gigantic landslides that originate on the unstable flanks of Hawai'i's volcanoes. Volcanic activity is now focused near the southeast tip of the island chain (i.e., at Kīlauea and Mauna Loa on the Big Island of Hawai'i and at nearby Lō'ihi). The steep submarine slopes of Mauna Loa and Kīlauea have been the source of several huge slides, which are partly responsible for the hummocky nature of the seafloor southwest and southeast of the Big Island. Historical lava flows are shown in red. North is at the top. Seafloor bathymetry derived in part from high-resolution multibeam-sonar surveys carried out by the Japan Marine Science and Technology Center (JAMSTEC), Yokosuka, Japan (*http://www.jamstec.go.jp/*). Additional sources for submarine bathymetry and subaerial topography: USGS, Menlo Park, California (*http://walrus.wr.usgs.gov/infobank/*); Monterey Bay Aquarium Research Institute, Monterey, California (*http://www.mbari.org/data/mapping/hawaii/index.htm*); University of Hawaii, School of Ocean and Earth Science and Technology, Honolulu, Hawaii (*http://www.soest.hawaii.edu/HMRG/*); National Geophysical Data Center, Boulder, Colorado (*http://www.ngdc.noaa.gov/mgg/bathymetry/relief.html*); Scripps Institution of Oceanography, San Diego, California (*http://sioexplorer.ucsd.edu/*); US Army Corps of Engineers, Mobile, Alabama (*http://shoals.sam.usace.army.mil/default.htm*); Global seafloor topography (predicted bathymetry) (*http://topex.ucsd.edu/marine_topo/mar_topo.html*).

the upper mantle to Kīlauea's summit reservoir. Also discernible are the two rift zones, which are seismically active in the 2–4 km depth range. By far the greatest number of earthquakes, and an even greater proportion of the seismic energy release, occurs at 5–10 km depth beneath the south flank. Focal mechanisms for many of the south flank earthquakes are consistent with slip on a sub-horizontal fault, which suggests seaward sliding along a shallow detachment fault, or décollement.

More direct evidence for the mobility of Kīlauea's south flank is available from repeated leveling and EDM surveys that span several decades. Comparison of leveling traverses across the historically active part of the East Rift Zone, for example, reveals the classic deformation pattern produced by intrusion of a near-vertical dike (i.e., broad uplift on either side of the dike trace punctuated by a sharp zone of subsidence directly above the dike) (Figure 7.20). Another effect of repeated intrusions along the rift zone is compression of the adjacent south flank, as recorded by repeated EDM

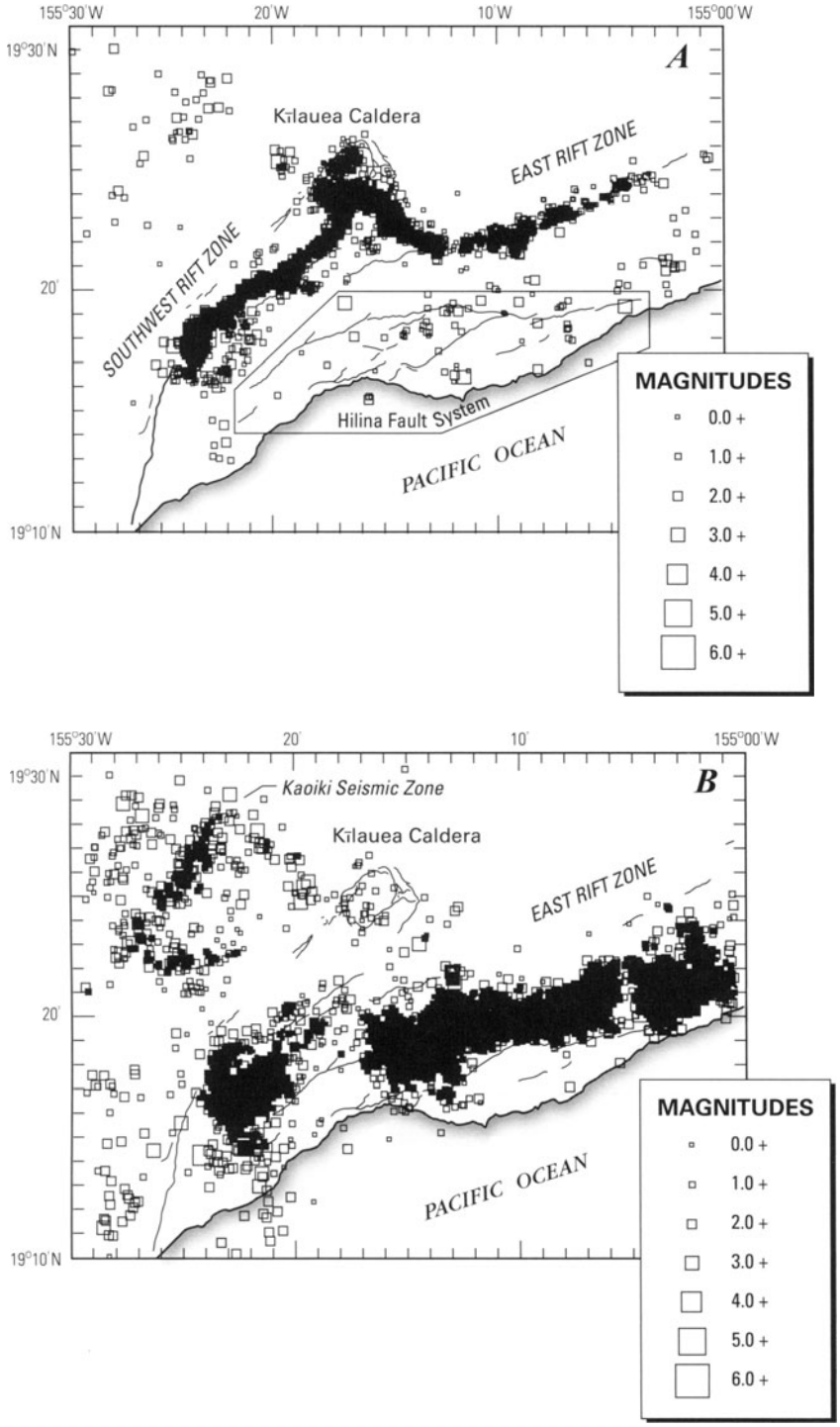

Figure 7.18. (A) Earthquake epicenters (squares) at Kīlauea Volcano in the depth range 3–4 km during 1970–1983. (B) Epicenters in the 6–7 km range for the same period. The shallower earthquakes outline the active rift zones, while the preponderance of deeper events occur beneath the volcano's mobile south flank.

From Klein *et al.* (1987).

measurements (Swanson *et al.*, 1976) (Figure 7.21). The north flank of Kīlauea is buttressed against Mauna Loa and, therefore, moves very little in response to intrusions into the rift zones. The south flank, on the other hand, is un-buttressed and also steeper than the north flank. As a result, it moves seaward under the combined influences of rift zone intrusions and gravitational stress. This motion is apparent in displacement vectors derived from repeated triangulation and trilateration surveys (Figure 7.22). With the geodetic data in mind, the significance of the strong concentration of

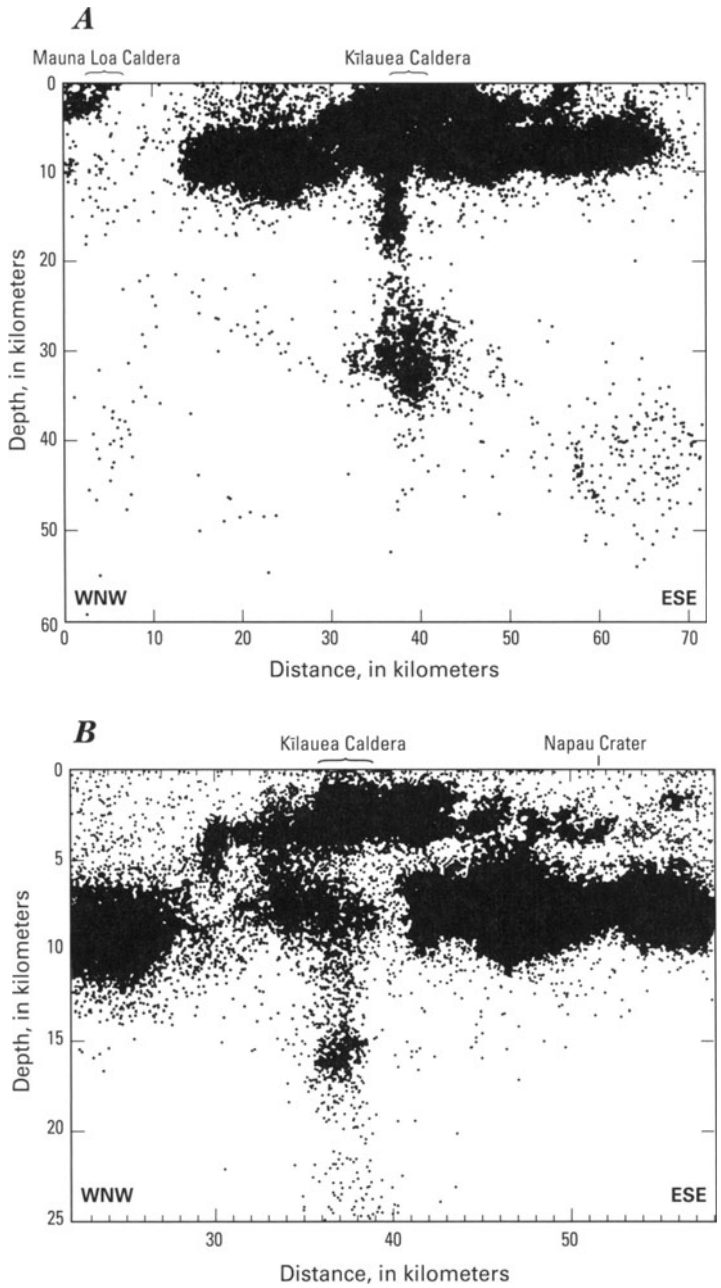

Figure 7.19. (A) WNW–ESE cross section through Kīlauea Volcano showing earthquake locations for 1970–1983. The vertical distribution of epicenters from about 40 km to 10 km depth outlines the conduit system that delivers magma from a mantle source to a reservoir beneath the summit region. Most of the earthquakes concentrated in the depth range 5–10 km occur beneath the volcano's mobile south flank. (B) Enlargement of (A) showing the concentrations of south flank earthquakes at 5–10 km depth and another at 2–4 km depth beneath the summit region and along the East Rift Zone. Napau Crater is a collapse feature (pit crater) along the rift zone.
From Klein *et al.* (1987).

earthquakes 5–10 km beneath the south flank is clear. As the flank moves seaward, it grinds over a basal décollement and deforms internally, producing thousands of small earthquakes. About once per century, the flank lurches seaward in a large event like those in 1868 and 1975.

In a pioneering paper, Swanson *et al.* (1976) reported seaward displacements of Kīlauea's south flank as large as 4.4 m from 1914 to 1970 and 2.3 m from 1958 to 1970. They noted that the direction of the displacements was similar to that of maximum stress axes derived from focal mechan-

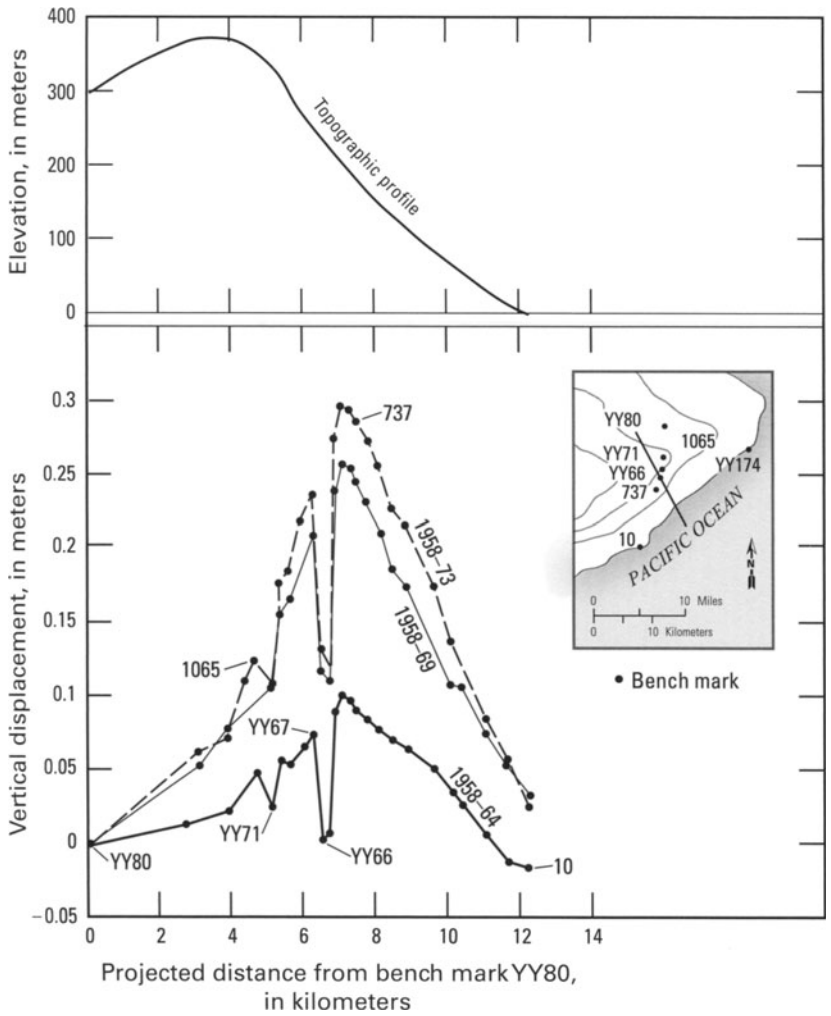

Figure 7.20. Vertical displacement and topographic profiles across the lower East Rift Zone of Kīlauea Volcano between 1958 and 1973 (Swanson *et al.*, 1976). The elevation of bench mark YY80 was held fixed. (*Inset*) The location of leveling route, key bench marks, and line of topographic profile. Contour interval of inset map is 150 m.

isms of south flank earthquakes and concluded (p. 1): '*We anticipate a subsidence event in the not too distant future, possibly similar to the damaging events of 1823 and 1868.*' The November 1975 *M* 7.2 Kalapana earthquake occurred while their paper was in press.

A major change in Kīlauea's behavior occurred on 3 January 1983, when the volcano entered an extended period of almost continuous eruption from vents along the East Rift Zone (Wolfe, 1988). By September 2002, 2.3 km^3 of lava had covered 110 km^2 and added 220 hectares (2.2 km^2 or ~540 acres) to Kīlauea's south shore – ranking the Pu'u 'Ō'ō-Kūpaianaha eruption as the longest and largest rift zone eruption of Kīlauea Volcano in more than 600 years (Heliker *et al.*, 2003; Heliker and Brantley, 2002; USGS Hawaiian Volcano Observatory, 2002). In the process, lava flows destroyed 189 buildings, many of them houses, and buried 13 km of highway with as much as 25 m of lava. A wealth of geodetic information reveals that the eruption was accompanied by steady subsidence of the summit area and rift zones and by continued seaward motion of the south flank. From 1976 to 1996, the summit widened by more than 250 cm and subsided more than 200 cm, while the adjacent south flank rose more than 50 cm (Delaney *et al.*, 1993, 1998). Summit widening slowed from about 25 cm yr^{-1} in 1976 to about 4 cm yr^{-1} in 1983, at the beginning of the Pu'u 'Ō'ō-Kūpaianaha eruption. Likewise, the average subsidence rate along the upper East Rift Zone slowed from ~9 cm yr^{-1} during 1976–1983 to about 4 cm yr^{-1} during 1983–1996. Horizontal motions across the East Rift Zone and south flank were correspondingly large. Delaney *et al.* (1998, p. 18,003) concluded that: '*Because the magnitudes of these contractions and extensions [across the subaerial south flank] are much less than the extension across the rift system, the subaerial south*

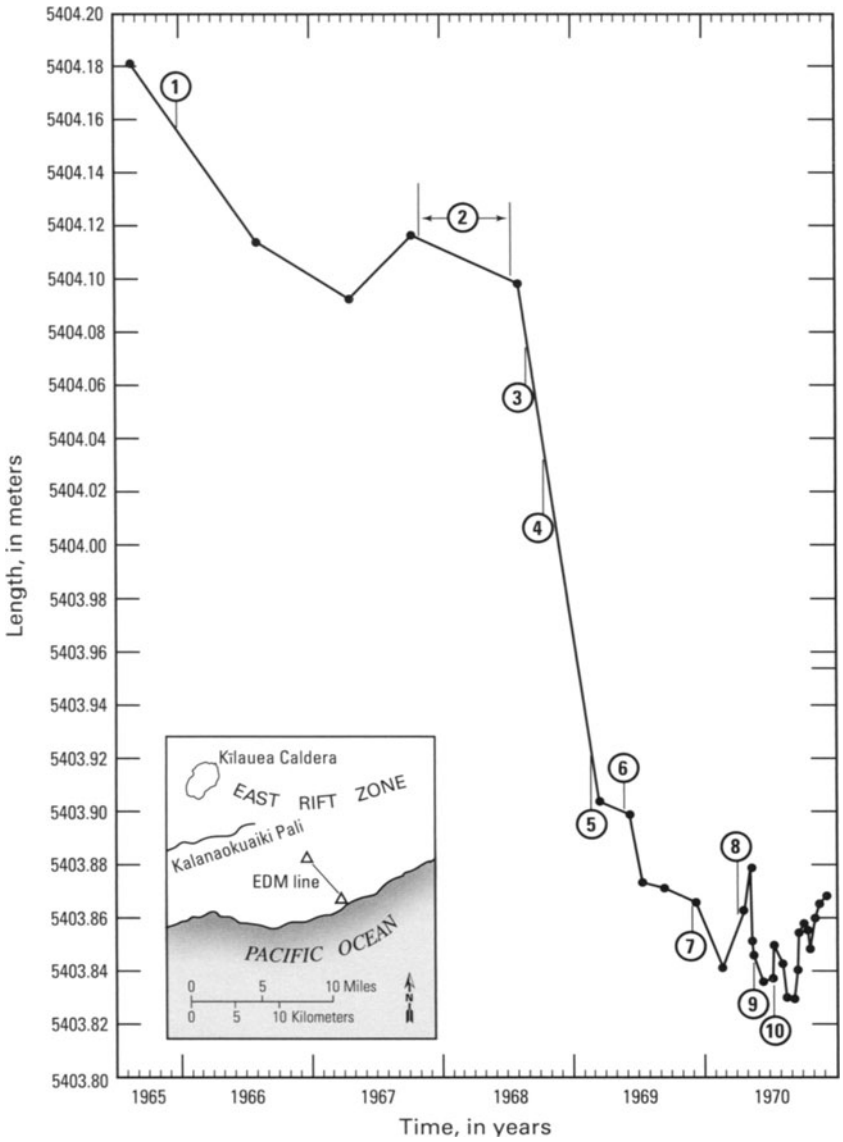

Figure 7.21. Contraction of a 5.4-km-long EDM line (*inset*) on the south flank of Kīlauea between August 1965 and December 1970. Major magmatic and structural events (circled numbers) during this period were: (1) December 1965 eruption and ground cracking; (2) November 1967–July 1968 summit eruption; (3) August 1968 eruption; (4) October 1968 eruption; (5) February 1969 eruption; (6) beginning of May 1969–October 1971 Mauna Ulu eruption; (7) new fissure north of Alae Crater, December 1969; (8) new fissure and cracks in and west of Aloi Crater, April 1970; (9) intrusion and cracking in southern part of Kīlauea Caldera, May 1970; and (10) new fissure east of Mauna Ulu, July 1970. See table 1 in Swanson *et al.* (1976) for additional information. Contraction is attributed to forceful intrusions along the East Rift Zone.

Modified from Swanson *et al.* (1976).

flank is apparently sliding seaward on its basal décollement more than it is accumulating horizontal strains within the overlying volcanic pile. Kilauea suffers from gravitational spreading made even more unstable by accumulation of magma along the rift system at depths in excess of about 4–5 km in the presence of hot rock incapable of withstanding deviatoric stresses.'[2]

Repeated GPS surveys and a growing network of continuous GPS stations have also tracked continued south flank motion during the Pu′u′Ō′ō-Kūpaianaha eruption. For example, Owen *et al.* (1995, 2000a) analyzed repeated GPS surveys from 1990 to 1996 and showed that the south flank moved seaward at an average rate of ~8 cm yr^{-1}. This is substantially slower than immediately after the 1975 earthquake, but still amazingly fast by most geodetic and geologic standards. While the south flank slipped seaward, the summit subsided ~8 cm yr^{-1}, the upper East Rift Zone subsided a few cm yr^{-1}, and the south coast rose 1–2 cm yr^{-1}. These movements are modeled very well by deep opening along the East Rift Zone, slip along a décollement near the base of the volcano, and deflation beneath the summit area (Figures 7.23 and 7.24). It is not yet known

[2] The term 'deviatoric stress' is quoted here from the original literature. The current author is aware of the article by Engelder (1994) entitled 'Deviatoric stressitis: A virus infecting the earth science community,' which points out widespread misuse of the term and attempts to set the record straight. In this case, the intended meaning seems clear.

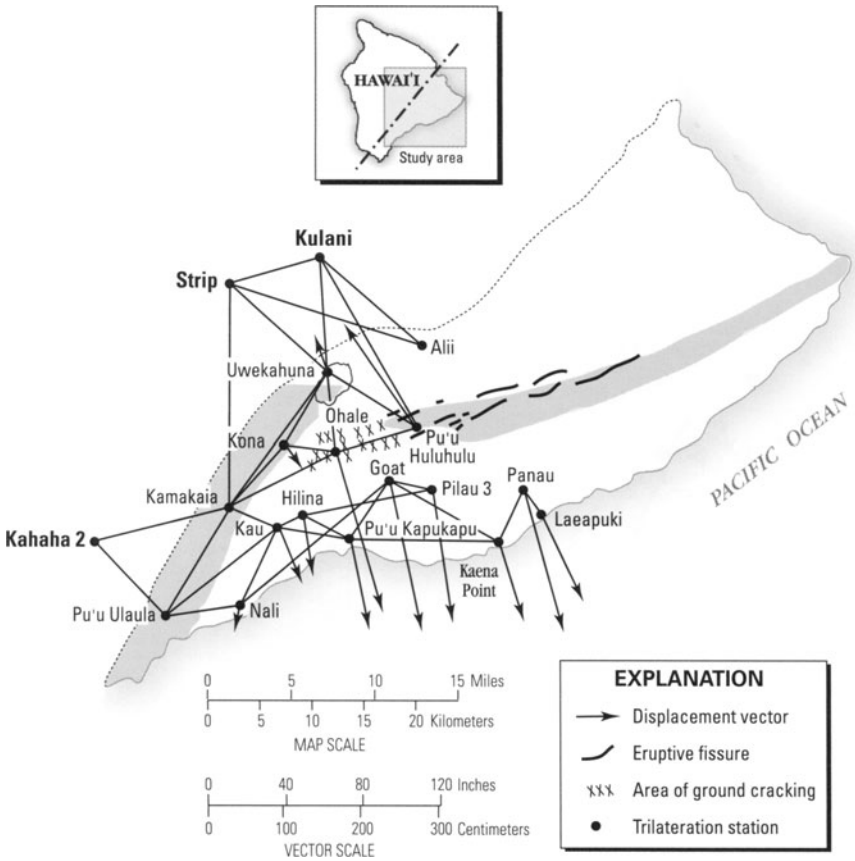

Figure 7.22. Horizontal ground displacements (arrows) at Kīlauea Volcano for the period 1961–1970, which included several eruptions along the East Rift Zone (Swanson *et al.*, 1976). Displacements were derived from comparison of a triangulation survey in 1961 and a trilateration survey in 1970. Stations in bold were held fixed. Shading represents the approximate extents of the Southwest Rift Zone and active part of the East Rift Zone. Also shown are areas of ground cracking and eruptive fissures during the survey interval.

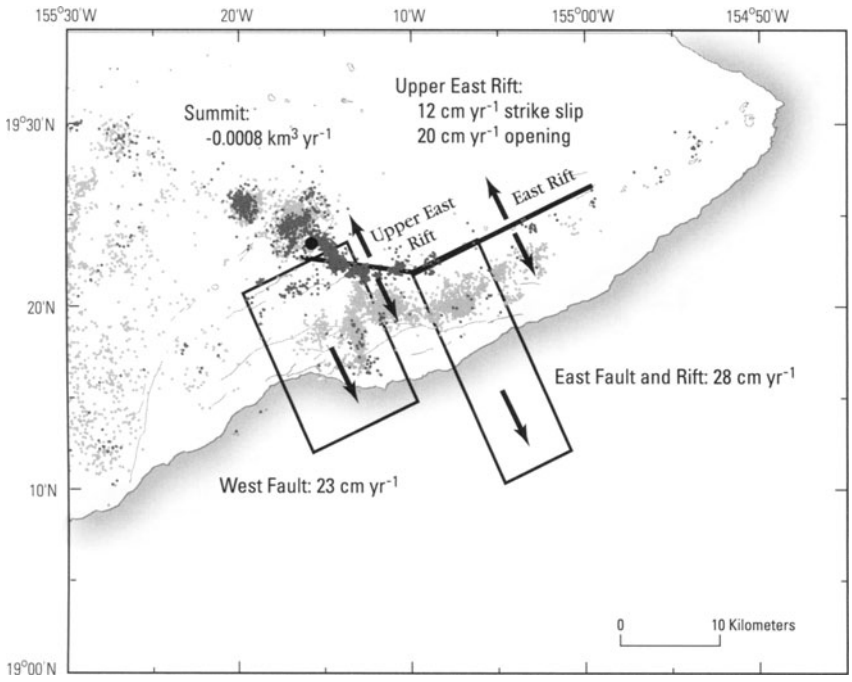

Figure 7.23. Elements of a best-fit model for deformation of Kīlauea Volcano measured by repeated GPS surveys from 1990 to 1996 (Owen *et al.*, 2000a). Rapid seaward motion of the south flank was accompanied by subsidence in the summit area and along the upper East Rift Zone, and by uplift of the south coast (Figure 7.24). These movements are consistent with deep opening along the rift zone (opposing arrows), slip along a décollement near the base of the volcano (arrows inside rectangles, which are the surface projections of two model dislocations), and deflation beneath the summit area (large solid circle). Light shaded dots represent earthquakes that occurred between 5 and 12 km depth; dark shaded dots represent earthquakes that occurred between 0 and 5 km depth.

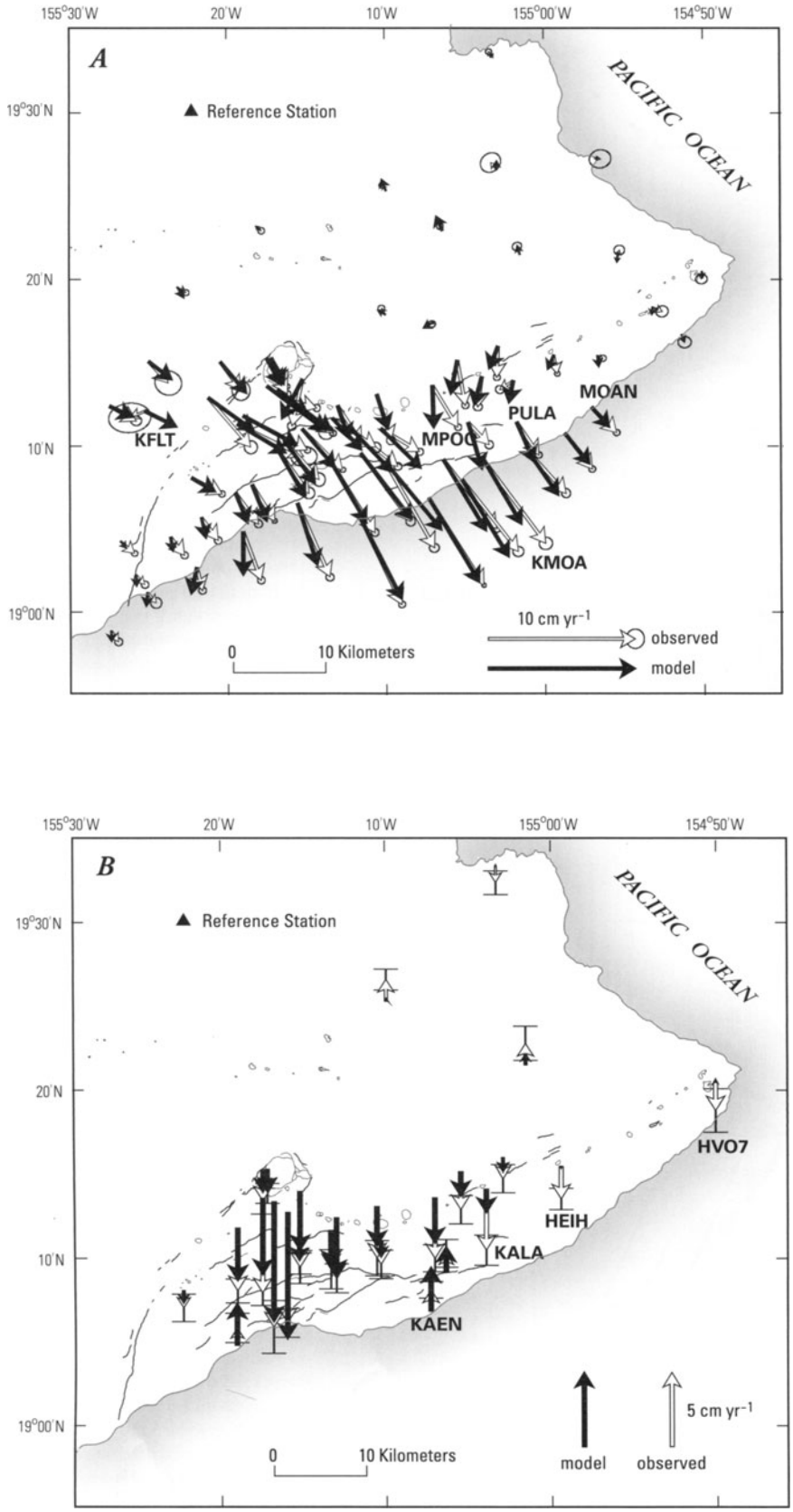

Figure 7.24. Model and observed horizontal (A) and vertical (B) displacement rates at Kīlauea Volcano based on repeated GPS surveys from 1990 to 1996 (Owen *et al.*, 2000a). Uncertainty in observed horizontal rates given by circle at arrow head (A). These results make a compelling case for deep opening along the rift zone, slip along a décollement near the base of the volcano, and deflation of the summit area.

how this motion is partitioned among after-slip from large earthquakes, steady gravitational spreading, and the ongoing Pu′u ′Ō′ō-Kūpaianaha eruption. One thing is crystal clear, though: Kīlauea's south flank has been and still is slipping into the sea at a remarkably high rate. What might be the implications of such rapid motion over geologic timescales?

7.2.2 Colossal prehistoric landslides and sea waves

We know that small, routine movements of the south flank are marked by earthquakes in the *M* 3–4 range and accumulate at a rate of about 1 meter per decade. Single earthquakes in the *M* 7–8 range have produced coastal displacements of several meters three times in the past 200 years. Could it be that 'mega-landslides' occur on the south flank with even longer recurrence intervals? The answer is yes, and the evidence is irrefutable.

The pattern of south flank movements revealed by repeated geodetic surveys led Swanson *et al.* (1976) to interpret the seaward-facing scarps of the Hilina fault system as headwalls of huge landslide blocks that are reactivated when cumulative lateral and upward displacement of the south flank renders the un-buttressed and over-steepened parts of the south flank unstable (Figures 7.25 and 7.26). This interpretation gained wide acceptance and posed some obvious questions. How large were the submarine landslide blocks hidden off the south coast of Hawai′i? Were the historical subsidence events of 1823, 1868, and 1975 typical of this process, or had much larger events occurred in the prehistoric past?

More than a decade earlier, Moore (1964) had correctly inferred, based on bathymetric evidence, the presence of two giant submarine landslides on the Hawaiian Ridge adjacent to the islands of Oahu and Molokai. In what turned out to be a particularly prescient discussion of the origin of these remarkable features, Moore concluded (p. D97): '*Because the Hawaiian Ridge is one of the earth's steepest and youngest major topographic features, it is a region favorable to large-scale landsliding.*' Earlier, I referred to the discovery of huge landslides off the south flank of Kīlauea as a compelling geologic detective story. Moore's 1964 paper meant that

Figure 7.25. Aerial view of several *en echelon* faults of the Hilina fault system on Kīlauea Volcano, Hawai′i. Pu′u Kapukapu is the nearest and most prominent fault scarp; Hilina Pali is the most distant. These historically active scarps are interpreted as headwalls of giant landslide blocks, most of which are submarine. This USGS photograph, taken by D.A. Swanson in 1971 before a *M* 7.2 earthquake in November 1975 caused coastal areas to subside more than 3 m, along these and other faults, drowning the coconut grove near the small island in the center foreground (circle).

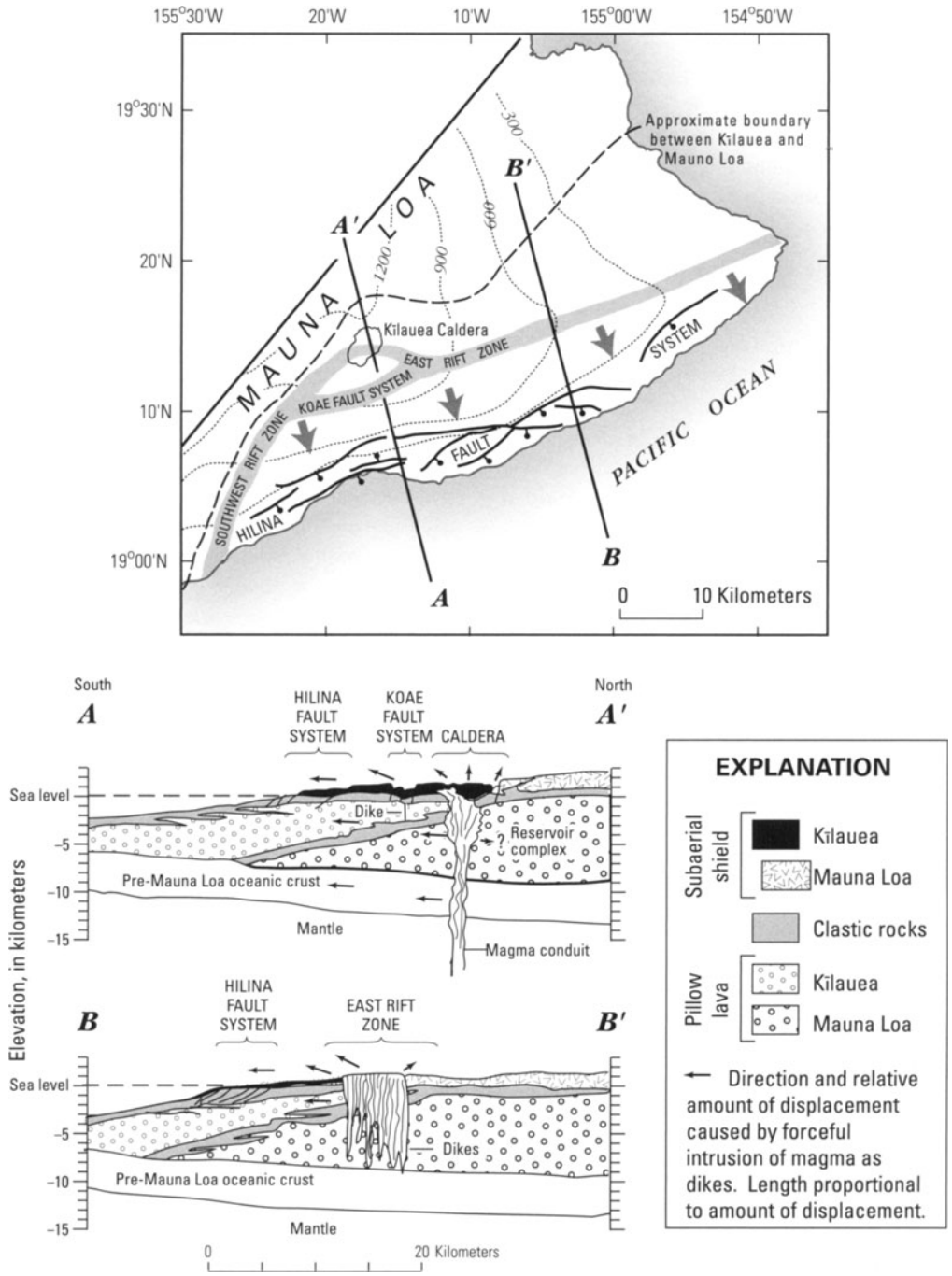

Figure 7.26. Index map and cross sections of Kīlauea illustrating the role of south flank landslides in seaward growth of the shield (Duffield *et al.*, 1982). The mobile south flank is bounded by the East Rift Zone, the Koae fault system, and the Southwest Rift Zone. Magma intruded as dikes into the rift zones from a summit reservoir wedges the south flank seaward and upward. The north flank is buttressed by much larger Mauna Loa and therefore is relatively stable. Contours in meters. Dashed line approximates the contact between Mauna Loa and Kīlauea lavas.

the case had been cracked, but the full story was yet to be told.

During 1976 and 1978, the research vessel *S.P. Lee*, operated by the USGS, studied areas of inferred submarine landslide deposits off the coasts of both Kīlauea and Mauna Loa. The voyage, which was inspired by the work of Moore (1964) and Swanson *et al.* (1976), produced a dramatic discovery: echo

sounding and seismic reflection profiling revealed the presence of slump and slide features extending as far as 80 km offshore! These were the largest submarine landslides known at the time.[3] Their discovery confirmed the landslide origin of the Hilina fault system on the island's southeast flank, and the Kealakekua and Kahuku faults on the southwest flank. However, a more complete understanding of the morphology, chronology, and impact of Hawai'i's giant landslides would take at least another decade.

The next bit of evidence came not from Hawai'i itself, but from the nearby island of Lanai. There, a widespread gravel deposit containing limestone derived from coral reefs was thought to have been deposited along ancient marine strandlines that formed during worldwide high stands of the sea. However, Moore and Moore (1984) used dated submerged coral reefs and tide gauge measurements to demonstrate that the island was sinking so fast under the weight of the Hawaiian Ridge that former high stands of the sea now lay below sea level. If the limestone-bearing gravel, found at a maximum height of 326 m above sea level, was deposited while the sea was essentially at its modern level, how were bits of coral reef carried to such a height?

The authors came to an astounding conclusion: The gravel was deposited by the surge of a giant ocean wave that swept several hundred meters up the flanks of Lanai and nearby islands about 100,000 years ago. Marine material in the deposit was ripped up from the littoral and sublittoral zone and mixed with basaltic debris as the wave swept inland, then deposited high above sea level as the wave receded. What could have caused such a tremendous wave? Its great run-up suggests it was not a tsunami caused by a submarine earthquake, because the largest historical tsunami recorded in Hawai'i reached only 17 m above sea level in 1946. Moore and Moore (1984, p. 1314) reasoned: '*Either the impact of a meteorite on the sea surface or a shallow submarine volcanic explosion could have generated the Hulupoe wave. We believe, however, that a more likely explanation is a rapid downslope movement of a sub-sea landslide on the Hawaiian Ridge, which is among the steepest and highest landforms on Earth . . . We infer that rapid movement of a submarine slide near Lanai displaced seawater forming a wave that rushed up onto the islands, carrying with it rock and reef debris from the near-shore shelf and beach.*' It was time to take a closer look at the seafloor around Hawai'i.

In 1986, the research vessel *M.V. Farnella* surveyed the offshore west flank of Mauna Loa using the sidescan sonar system GLORIA, echo sounding, and seismic-reflection profiling (e.g., Moore *et al.*, 1989). The results were striking. The GLORIA images revealed that the Alika slide off the southwest coast of Hawai'i was even larger and morphologically more complex than previously thought (Figure 7.27). Its hummocky surface resembles that of subaerial debris avalanches such as the famous 1980 deposit at Mount St. Helens. Rather than a prolonged or repetitive sequence of slump or creep events comparable in magnitude to the November 1975 event, '. . . *the Alika slide represents several geologically rapid events involving mass flowage*' (Lipman *et al.*, 1988, p. 4285). In other words, the slide consists of far-traveled debris from several catastrophic mass movements in which part of the west flank of Hawai'i literally slumped into the sea. What is more, the Alika slide is associated with less rapidly emplaced gravitational slump and slide features that occupy virtually the entire submarine west slope of Hawai'i (Lipman *et al.*, 1990, 2002).

Subsequent GLORIA data revealed similar large flowage deposits off the southeast slope of Hawai'i that head in the area of the Hilina fault system. Finally, a conjecture based on a structural interpretation and supported by both geodetic data and the occurrence of a large earthquake was verified by direct observation. The recurrence interval for catastrophic debris avalanches in Hawai'i seems to be on the order of 100,000 years, while that for events on the scale of November 1975 is approximately 100 years. It is especially remarkable that this fascinating story was pieced together both before and after the 1980 debris avalanche at Mount St. Helens, which so vividly demonstrated the importance of flank failures in the development of many stratovolcanoes. Thanks to decades of persistent detective work, we now know that the same is also true for the gently sloping shield volcanoes of Hawai'i.

[3] Other enormous submarine landslide deposits were discovered soon thereafter, including the 5,600 km^3 Storegga Slide off the western coast of Norway (Bugge, 1983), which left evidence of a tsunami along the eastern coast of Scotland about 7,000 years ago (Dawson *et al.*, 1988; Long *et al.*, 1989). Masson (1996) and Masson *et al.* (2002) identified several large submarine landslides and associated deposits offshore the western Canary Islands, including the large ~15 ka El Golfo debris avalanche off the flank of El Hierro Volcano, and a 1,000 km^3 slide offshore the Oratava and Icod valleys on Tenerife from Las Cañadas Volcano (Watts and Masson, 1995).

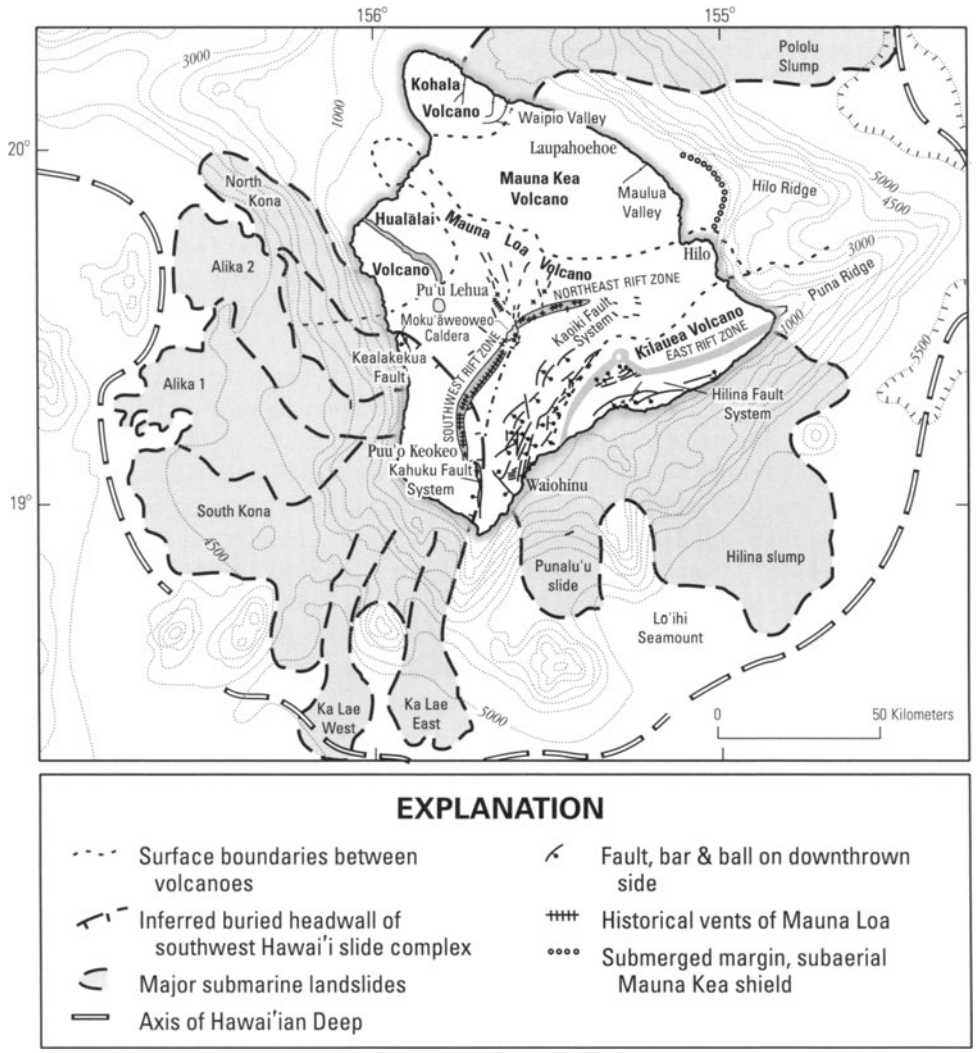

Figure 7.27. Major submarine landslides (stippled) surrounding the Big Island of Hawai'i. Contour interval is 500 m. Modified from Lipman *et al.* (1990, 2002).

7.3 YELLOWSTONE – THE UPS AND DOWNS OF A RESTLESS CALDERA

On 1 March 1872, the US President Ulysses S. Grant set aside 2.2 million acres (8,900 km^2) of wilderness for '*... the benefit and enjoyment of the people*' and declared Yellowstone to be the world's first national park. The event followed several million years of persistent and at times frenetic groundwork by tectonic, volcanic, and hydrothermal processes that formed Yellowstone's spectacular landscape and continue to shape it today. Even so, the region's geologic heritage is mostly lost on millions of visitors each year, who fail to make a connection between the Park's renowned hydrothermal features and the world-class magmatic system that lies hidden below the surface. Fortunately, this is changing for the better as more is learned about Yellowstone's tumultuous geologic past, including evidence for dramatic ground movements that continue to the present day.

7.3.1 Tectonic setting and eruptive history

The scenic Yellowstone Plateau lies along the northeastward extension of the eastern Snake River Plain – a region of young extensional tectonics and basalt–rhyolite volcanism in the western USA (Figure 7.28). The Yellowstone Plateau is generally acknowledged to be a 'hotspot' that marks the location of either a buoyant plume originating in the mantle (e.g., Pierce and Morgan, 1992; Smith and Braile, 1994), or a melting anomaly that reflects feedback between upper-mantle convection and regional lithospheric

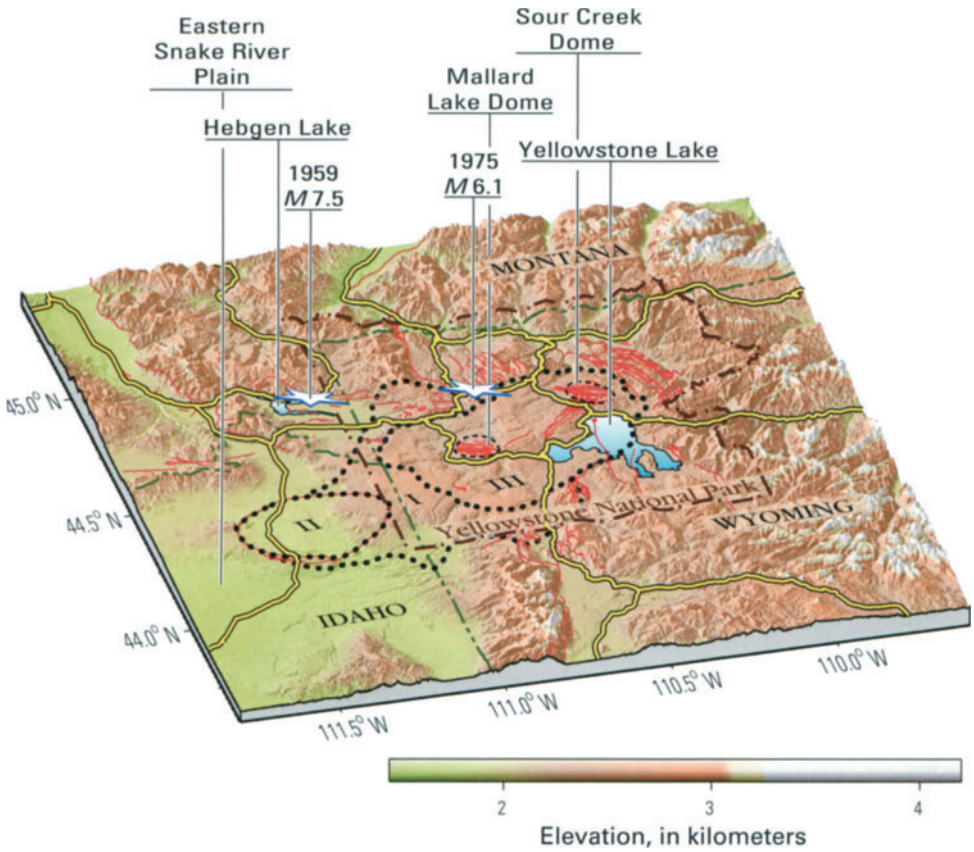

Figure 7.28. Eastern Snake River Plain and Yellowstone Plateau with outlines (heavy dotted line) of three youngest calderas: (I) 2.0 Ma Huckleberry Ridge; (II) 1.3 Ma Mesa Falls; and (III) 0.64 Ma Lava Creek. Also shown, outlines of the Mallard Lake and Sour Creek resurgent domes (light dashed line). White stars indicate epicenters of 1959 M_s 7.5 Hebgen Lake earthquake and 1975 *M* 6.1 Yellowstone Park earthquake.
Graphic created by C. Wicks, USGS.

tectonics (Christiansen, 2001; Christiansen *et al.*, 2002). The 700-km by 90-km northeast-trending Snake River Plain–Yellowstone Plateau volcanic province marks the southwestward track of the North American plate over the plume or melting anomaly during the past ~16 million years. According to Morgan and McIntosh (2005, p. 288): '*Passage of the North American plate over the melting anomaly at a particular point in time and space was accompanied by uplift, regional extension, massive explosive eruptions, and caldera subsidence, and followed by basaltic volcanism and general subsidence.*'

For the past 2 million years, explosive rhyolitic volcanism has been focused at the Yellowstone Plateau, including Yellowstone National Park. The dominantly extensional tectonic regime at Yellowstone reflects the influence of northeast–southwest Basin and Range extension in the region. Yellowstone seismicity is characterized by swarms of $M < 3$ earthquakes within the 0.64 Ma caldera (see below) and between the caldera and the eastern end of the 44-km-long rupture of the M_s 7.5 Hebgen Lake earthquake (Waite and Smith, 2004) (Section 7.3.3).

For the interested reader, I recommend the book *Windows into the Earth* by Smith and Siegel (2000), which tells the geologic story of Yellowstone and Grand Teton National Parks in vivid detail. For a more technical treatment of Yellowstone geology, USGS Professional Paper 729-G, *The Quaternary and Pliocene Yellowstone Plateau volcanic field of Wyoming, Idaho, and Montana* (Christiansen, 2001), is the definitive work.

Three times during the past 2 million years – 2.0, 1.3, and 0.64 million years ago – large rhyolite magma bodies formed in the upper crust beneath Yellowstone, eventually fueling immense explosive eruptions that resulted in caldera collapses (Christiansen, 1984, 2001). The current Yellowstone Caldera, 45 km wide by 75 km long, formed about 640,000 years ago during the eruption of 1,000 km^3

of rhyolitic ash flows constituting the widespread Lava Creek Tuff. Soon thereafter, structural resurgence formed the Sour Creek and Mallard Lake resurgent domes, and rhyolitic volcanism resumed within the caldera. Renewed doming in the western part of the caldera culminated with extrusion of 1,000 km^3 of intra-caldera rhyolite flows that virtually buried the Yellowstone Caldera between 150,000 and 75,000 years ago. Abundant geophysical evidence exists for the presence of partial melt beneath the caldera (e.g., Benz and Smith, 1984; Miller and Smith, 1999; Husen *et al.*, 2004) and the consensus among those who have studied the area is that the Yellowstone magmatic system will almost surely erupt again. We just don't know when.

7.3.2 Results of repeated leveling surveys

In view of Yellowstone's explosive past, characterizing the current state of the Yellowstone magmatic system and assessing its potential for future eruptions has been a priority of the USGS Volcano Hazards Program for several decades. The USGS initiated a program of detailed geologic mapping and exploration of Yellowstone's hydrothermal system in the 1960s, and since then numerous investigators from around the world have studied the Park's geology, geophysics, geochemistry, and hydrology. In cooperation with the USGS, the University of Utah operates a regional seismic network to record Yellowstone's frequent and sometimes damaging earthquakes. In 2001, the USGS, University of Utah, and National Park Service formed a partnership to create the Yellowstone Volcano Observatory (YVO).

From a geodetic perspective, an important milestone was reached during 1975–1977 when a 1923 leveling survey throughout Yellowstone National Park was repeated for the first time. The resulting discovery of rapid uplift within the caldera set the stage for a more vigorous leveling effort starting in 1983. The Yellowstone leveling network consists of approximately 380 km of interconnected loops and spurs along all major roads and one back-country trail in Yellowstone National Park. Most of the network was measured in 1923, in increments from 1975 to 1977 (hereafter called the 1976 survey), and in 1987; partial surveys were conducted in 1936, 1941, 1955, 1960, and most years from 1983 to 2000 (see below).

During the interval between the 1923 and 1976 surveys, the central part of the Yellowstone Caldera rose as much as 726 ± 21 mm with respect to K12 1923, a reference bench mark located about 8 km outside the east caldera rim (Pelton and Smith, 1979, 1982; Figure 7.29). The maximum uplift measured was at bench mark B11 1923, near LeHardys Rapids (variant names, Le Hardys Rapids, LeHardy's Rapids) at the base of the Sour Creek resurgent dome in the eastern part of the caldera. By the time of the next complete survey in 1987, bench mark DA3 1934 near LeHardys Rapids had risen an additional 115 ± 5 mm with respect to 36MDC 1976 (near K12 1923). The average uplift rate from 1976 to 1987 was 10 ± 1 mm yr^{-1}, apparently less than from 1923 to 1976 (14 ± 1 mm yr^{-1}). However, we know from annual surveys starting in 1983 that uplift stopped during 1984–1985 and subsidence began during 1985–1986, so the average uplift rate for 1976–1987 underestimates the actual rate for the early part of that period.

Each year from 1983 to 1998, except 1994, 1996, and 1997, we measured part or the entire leveling traverse between Lake Butte and Mount Washburn to first-order, class II standards (Chapter 2). We chose this route because it is approximately perpendicular to the uplift axis determined by the earlier surveys, and because it includes the area of maximum uplift near LeHardys Rapids. Leveling at Yellowstone in late summer, when the season's highest temperatures and heaviest traffic have receded and the Park starts to hunker down for another brisk Rocky Mountain winter, is pure delight for a volcanologist interested in ground deformation. Over a period of several days, we survey from Lake Butte, a high point on the caldera rim overlooking the glistening expanse of Yellowstone Lake, down into the caldera and across its floor to Mount Washburn on the opposite rim. Along the way, we skirt the shore of Yellowstone Lake, pass by the drowned hydrothermal explosion craters of Indian Pond and Mary Bay, cross Fishing Bridge at the lake outlet, and follow the Yellowstone River through herds of bison in Hayden Valley to the brightly colored canyon that inspired Yellowstone's name. From Canyon Junction, we climb the flank of Mount Washburn to a final bench mark overlooking Washburn Hot Springs, one of countless areas in the Park where hot water and magmatic gases seep out of the ground along fractures that mark the caldera boundary. A year later, we do it all over again, and then compare the two surveys to see how much the ground surface has risen or fallen while we were gone.

During the 16 years spanned by our surveys, vertical displacements of Canyon Junction and Mount

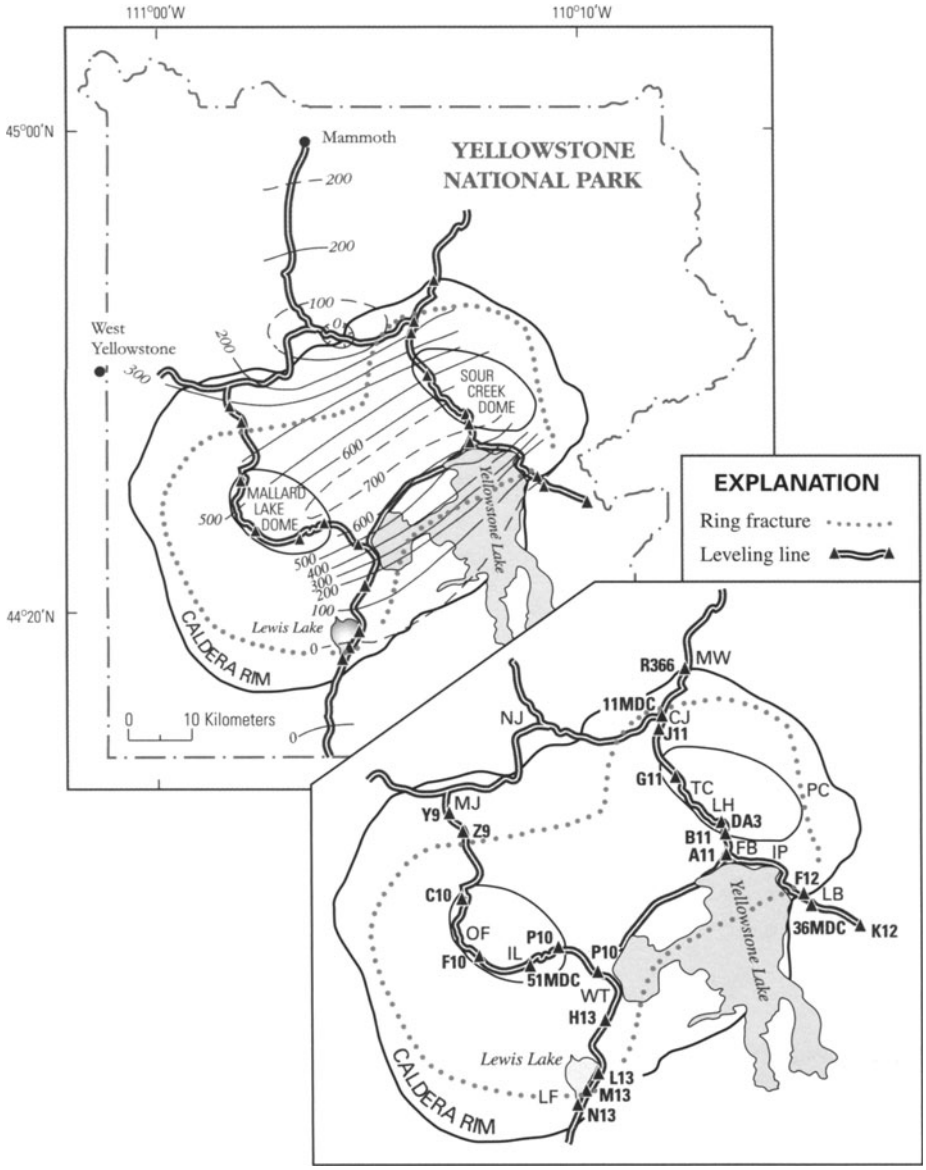

Figure 7.29. Vertical displacements in Yellowstone National Park derived from comparison of leveling surveys in 1923 and 1975–1977. Uplift contours in millimeters are from Pelton and Smith (1982). Localities (Lake Butte to Mount Washburn): LB, Lake Butte; IP, Indian Pond; FB, Fishing Bridge; LH, LeHardys Rapids; TC, Trout Creek; CJ, Canyon Junction; MW, Mount Washburn; (Lewis Falls to Madison Junction): LF, Lewis Falls; WT, West Thumb; IL, Isa Lake; OF, Old Faithful; MJ, Madison Junction; (other): NJ, Norris Junction; PC, Pelican Cone. Triangles represent bench marks (Lake Butte to Mount Washburn): K12 1923, 36 MDC 1976, F12 1923, B11 1923, DA3 1934, G11 1923, J11 1923, 11MDC 1976, R366 1987; (Lewis Falls to Madison Junction): N13 1923; M13 1923, H13 1923, P10 1923, M10 1923, 51MDC 1976, F10 1923, C10 1923, Z9 1923, Y9 1923.

Washburn relative to Lake Butte were generally less than two standard deviations of the measurements. So the caldera rim has been relatively stable while virtually the entire caldera floor has moved up and down (Figure 7.30). Between the 1976 and 1984 surveys, DA3 1934 rose 177 ± 5 mm with respect to 36MDC 1976, at an average rate of $22 \pm 1\,\text{mm yr}^{-1}$. To our surprise, the displacement at DA3 1934 with respect to 36MDC 1976 during 1984–1985 was only -2 ± 5 mm, and the largest displacement measured anywhere along the traverse, -7 ± 5 mm, was hardly significant. In hindsight, the uplift rate near LeHardys Rapids had probably dropped below its historical average of $14–23\,\text{mm yr}^{-1}$ by the time of our 1984 survey, and it was essentially zero during 1984–1985. We wondered how long it would be before uplift resumed.

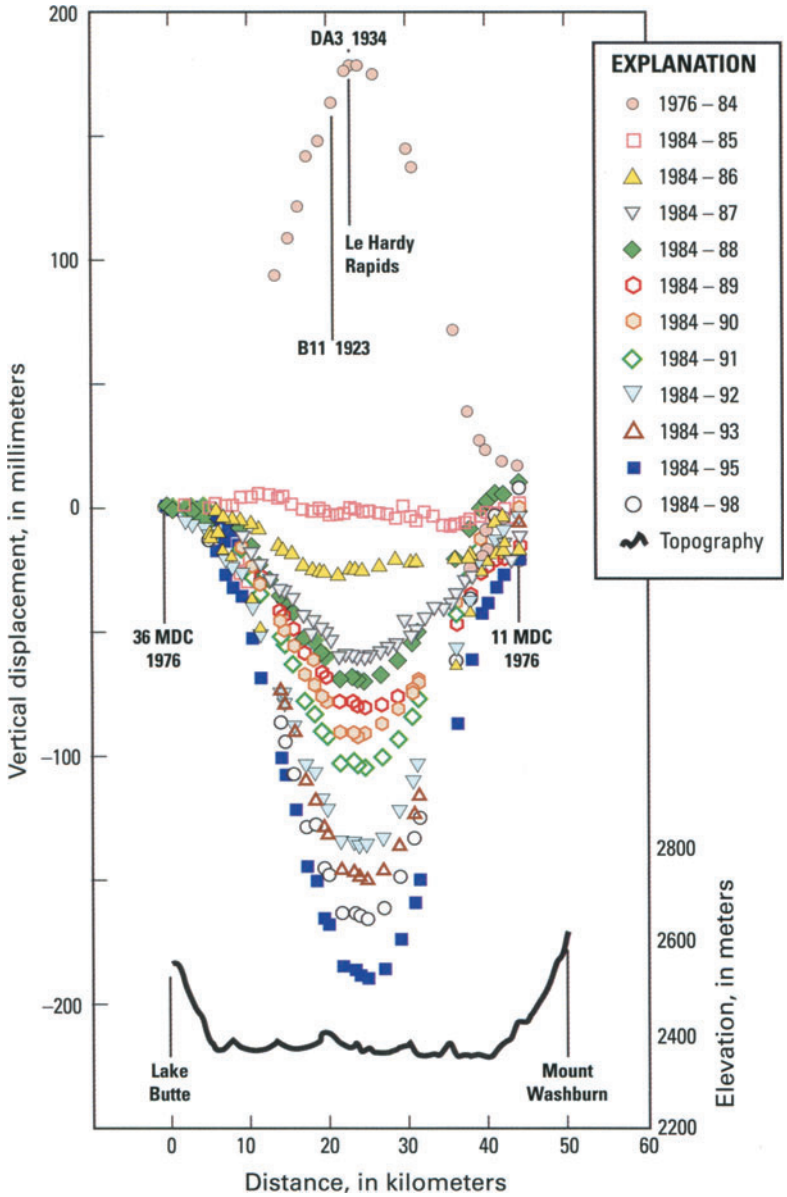

Figure 7.30. Vertical displacement profiles across the Yellowstone Caldera between two points on the caldera rim, Lake Butte and Mount Washburn, from repeated leveling surveys between 1976 and 1998. Uplift that began before 1976 stopped during 1984–1985, and the caldera floor progressively subsided during 1985–1995. Renewed uplift starting in 1995 was discovered with interferometric synthetic-aperture radar (InSAR) and confirmed by leveling.

We were surprised again when the caldera floor began to subside during 1985–1986 and continued to do so for the next decade (Dzurisin *et al.*, 1990, 1994) (Figures 7.30 and 7.31). Some of the annual displacements are less than the analytical uncertainty in the measurements, but the net displacement at DA3 1934 from 1985 to 1995, -189 ± 5 mm (-17 ± 1 mm yr^{-1}), is unequivocal. While subsidence persisted for more than a decade, its rate varied with time. For example, subsidence was relatively rapid during 1985–1986 (-25 ± 1 mm yr^{-1}), 1986–1987 (-34 ± 1 mm yr^{-1}), and 1991–1992 (-32 ± 1 mm yr^{-1}). But during 1988–1991, the annual rate was only 9–13 $\pm$ 1 mm yr^{-1}.

The shape of the 1985–1995 subsidence profile mirrors that of the 1976–1984 uplift profile, and the average maximum displacement rates for the two intervals also are similar (-19 ± 1 mm yr^{-1} and 22 ± 1 mm yr^{-1}, respectively). This suggests that the sources for uplift and subsidence have similar locations and dynamics, although the leveling data alone do not constrain the depth or geometry of the sources very tightly. A more constrained solution is obtained by modeling simultaneously the vertical displacements from leveling surveys and horizontal displacements from repeated GPS surveys (Meertens and Smith, 1991; Meertens *et al.*, 1992, 1993; Vasco *et al.*, 1990; Section 7.3.4).

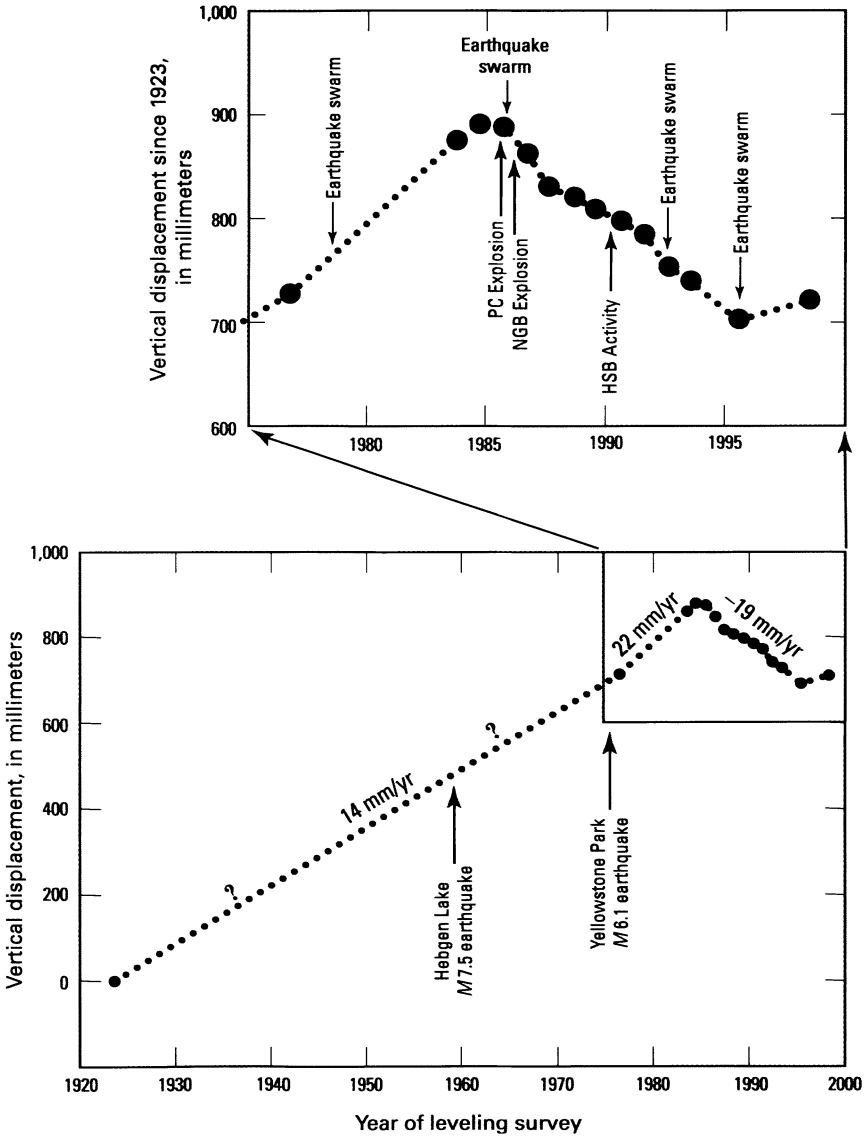

Figure 7.31. History of vertical displacements at bench mark B11 1923 near LeHardys Rapids as measured by leveling surveys from 1923 to 1998. Displacements are relative to bench marks 1923 or 36 MDC 1976, both located outside the caldera near its east rim. Arrows mark times of noteworthy events discussed in the text. Dotted lines represent one possible time history for the deformation, although the actual time dependence between surveys is unknown. PC, Pelican Cone; NGB, Norris Geyser Basin; HSB, Hot Spring Basin.

The history of vertical displacements at Yellowstone as measured by leveling surveys is summarized in Figure 7.31, which shows the elevation of bench mark B11 1923 as a function of time from 1923 to 1998. B11 1923 was chosen because, among the marks that survived from 1923 to 1998, it is closest to the area of maximum surface displacement. It is located about 2 km south of LeHardys Rapids and records about 95% of the maximum displacement measured at DA3 1934. The closely spaced data points for the years from 1983 to 1998 are satisfying, especially to someone who enjoyed carrying a leveling rod across the caldera for most of those surveys, but long intervals between the earlier surveys pose an obvious question.

7.3.3 What happened between leveling surveys?

The largest earthquake ever recorded in the Yellowstone region, the M_s 7.5[4] Hebgen Lake earthquake, occurred on 18 August 1959, about 25 km north-northwest of the northwest rim of the Yellowstone

[4] M_s refers to surface-wave magnitude, which is based on the amplitude of Rayleigh surface waves measured at a period near 20 s. Depending on how they were determined, earthquake magnitudes are expressed as local magnitude (M_L), body magnitude (M_b, based on the amplitude of P body-waves), or moment magnitude (M_w, based on the moment of the earthquake). Unless specified otherwise, earthquake magnitude M refers to local magnitude.

Caldera and 65 km west–northwest of LeHardys Rapids. Within 24 hours, six aftershocks of M 5.5 to 6.3 had occurred in an east–west-trending zone nearly 100 km long centered on the main shock. Another major earthquake, the M 6.1 Yellowstone Park event on 30 June 1975, was centered approximately 5 km beneath the north caldera rim near Norris Junction, 20 km northwest of LeHardys Rapids (Pitt *et al.*, 1979). All of these large earthquakes occurred during the 53-year interval between the 1923 and 1976 leveling surveys (Figure 7.31). Any effects they may have had on the short-term vertical displacement rate are undocumented.

No earthquakes larger than M 5.5 have occurred in the Yellowstone region since the 1976 leveling survey, but there have been many swarms of smaller earthquakes within or near the caldera. Those in 1978, 1985, 1992, and 1995 (Figure 7.31) are especially noteworthy. The May–November 1978 swarm occurred at depths of 1–5 km beneath the Mud Volcano hydrothermal area, about 5 km northwest of LeHardys Rapids. At least 8 earthquakes in the swarm were larger than M 2.5, and the largest was M 3.1. At its peak the swarm produced more than 100 events per hour. The earthquakes were followed by increased thermal activity in the Mud Volcano area starting in December 1978. Pitt and Hutchinson (1982, p. 2762) concluded that the earthquakes '*expanded pre-existing fracture systems, permitting increased fluid flow from depths of several kilometers*.' The net vertical surface displacement near LeHardys Rapids from 1976 to 1984 was 177 ± 5 mm. Any deformation that might have accompanied the 1978 swarm is otherwise undocumented.

The most intense earthquake swarm ever recorded in the Yellowstone region occurred between West Yellowstone and Madison Junction, just outside the northwest rim of the caldera, starting on 7 October 1985. Twenty-eight events larger than M 3.5 (maximum 4.9) occurred during the first three months of activity, which persisted into 1986. These earthquakes, and many others in the vicinity that occurred before and afterward, are attributed to stress release in relatively cold, brittle crust outside the caldera. Inside, the crust below ~5 km is too hot to fracture; instead, it deforms in ductile fashion without producing many earthquakes (Smith and Arabasz, 1991).

A third interesting swarm occurred about 3 km south of LeHardys Rapids on 20 July 1992. It included 8 earthquakes larger than M 1.8 (maximum 4.6), all within 4 km of the surface. These earthquakes occurred directly beneath the level line that we measured each year from 1983 to 1993, and their occurrence coincides with an increase in subsidence rate detected by the 1991 and 1992 surveys (from $-11 \pm 5\,\mathrm{mm\,yr^{-1}}$ during 1990–1991 to $-32 \pm 5\,\mathrm{mm\,yr^{-1}}$ during 1991–1992).

The second most intense earthquake swarm in the Yellowstone region since the 1959 M_S 7.5 Hebgen Lake earthquake occurred during June–July 1995 near Madison Junction, along the northwest caldera boundary. It comprised over 560 locatable earthquakes, including over 170 on 4 July alone, with a maximum magnitude of 3.1.

In addition to earthquake swarms, there have been some dramatic changes in Yellowstone's hydrothermal features since we began our annual leveling surveys in 1983. For example, in 1985, 1986, and 1990, notable hydrothermal events occurred at three widely separated locations along the caldera rim. In 1985, probably in early July, an explosion near Pelican Cone, about 5 km east of the east caldera rim, killed mature trees, formed a crater 5 m × 2 m × 2 m deep, and gave rise to a new superheated fumarole.[5] In January 1986, a larger explosion in mature forest 3 km west of Norris Junction threw debris 35 m laterally, knocked down trees, and formed a crater 10 m × 15 m × 5 m deep. Starting in early 1990 and continuing through the end of 1993, increasing ground temperatures in a part of the Hot Springs Basin thermal area near the head of Astringent Creek killed trees and led to the emergence of another superheated fumarole and a vigorous new mud volcano (Hutchinson, 1993). The active area is about 9 km east–northeast of LeHardys Rapids.

Changes in hydrothermal activity are common at Yellowstone, but the magnitude of these three events is unusual in recent history. The first occurred about 3 months before the start of the 1985 swarm and during the interval between the 1984 and 1985 leveling surveys, which showed that uplift had stopped (Figures 7.30 and 7.31). The second explosion occurred about three months after the start of the 1985 swarm and during the interval between the 1985 and 1986 surveys, which detected the onset of subsidence. The 1990–1993 activity near the head of Astringent Creek apparently started

[5] The activity in a remote part of Yellowstone National Park went unnoticed at the time, except possibly for a false report of smoke from the area on 3 July 1985. The new feature was discovered on 5 October 1986 by National Park Service geologists Roderick (Rick) Hutchinson and C. Craig-Hunter (Hutchinson, 1992).

before and continued after a period of relatively rapid subsidence during 1991–1992.

An episode of surface uplift centered near Norris Geyser Basin along the north caldera rim began in 1997, as revealed by radar interferometry (Wicks *et al.*, 2002c, 2003) (Chapter 5). The uplift affected an area of 30 km by 40 km and was accompanied by increased thermal activity, including the formation of a 75-m line of fumaroles just north of Norris Geyser Basin, an eruption of Porkchop Geyser, which had been dormant since 1989, and five eruptions of Steamboat Geyser. Major eruptions of Steamboat usually occur about once per decade and can reach heights of 90 m, prompting the US National Park Service to celebrate Steamboat as 'the world's tallest active geyser.' Modeling indicates the source depth for the Norris uplift is 10–12 km beneath the surface, which places it well below the inferred base of the hydrothermal system. The most likely cause is a magmatic intrusion near the intersection of the caldera ring fault system and the Norris–Mammoth corridor, a north–south-trending system of faults, volcanic vents, and active hydrothermal features between Norris Geyser Basin and Mammoth Hot Springs. Such intrusions undoubtedly power Yellowstone's vigorous hydrothermal system and might have escaped detection before the advent of InSAR. The Norris uplift paused during 2002–2003 (Wicks *et al.*, 2005). When and where the next episode of uplift or subsidence will occur is anyone's guess.

7.3.4 Causes of uplift and subsidence

The association of earthquake swarms, hydrothermal activity, and changes in the rate of caldera floor uplift or subsidence suggests that these three processes are connected. Although the details are still unknown, there is general agreement on a conceptual model that accounts for most aspects of the uplift, subsidence, and relative timing between seismic and hydrothermal events described above. Before discussing the model, though, it is useful to consider several potential deformation mechanisms and the role that each might play over various timescales.

Over timescales of 10^5–10^6 years, the ultimate cause of uplift and other forms of unrest at Yellowstone almost surely is episodic intrusion of new basaltic magma from the mantle into the crust beneath the caldera. Continued heat transfer to the crust by basaltic magma is the only plausible explanation for the longevity and vigor of Yellowstone's spectacular hydrothermal system (Fournier and Pitt, 1985). We know from measurements of the chloride flux from rivers draining Yellowstone that the integrated convective heat flux is about 4×10^{16} cal yr^{-1}. Withdrawing heat at that rate would completely crystallize and cool about 0.1 km^3 of rhyolite magma each year. Since the last magmatic eruption at Yellowstone about 70,000 years ago, this corresponds to a lens of cold rock about 3 km thick beneath the entire caldera. So, if it were not being reheated periodically from below, Yellowstone's hydrothermal system would be literally stone cold by now. Instead, it is vigorously active and has not shown any signs of slowing down for at least the past 50,000 years. The heat that sustains it must come from episodic intrusions of basalt into the base of the silicic magma system, and such intrusions likely cause uplift.

There is plenty of other evidence for basaltic intrusions beneath Yellowstone throughout its history. Basalt has erupted all around the Yellowstone Caldera, both before and since the caldera-forming Lava Creek eruption 640,000 years ago, and basaltic lava flows have flooded the older part of the Yellowstone magmatic system west of the caldera (Christiansen, 1984, 2001). In addition, a preponderance of geophysical and geochemical evidence indicates that a body of partly molten rhyolite still exists beneath the Yellowstone Caldera, presumably remnant from the last caldera-forming eruption (Christiansen, 1984, 2001; Smith and Braile, 1994; Smith and Siegel, 2000). The rhyolitic magma probably acts as a density shadow for basaltic magma (i.e., basalt does not rise through rhyolite by buoyant convection because basalt is denser than rhyolite). Instead, basalt tends to underplate rhyolite beneath the caldera, thereby heating and sustaining it in a partly molten state. In the process, the magmatic system pressurizes, overlying rocks are shoved upward, and the ground surface rises.

Intrusions of silicic magma into the upper crustal rhyolite body are also likely. Basalt that rises from the upper mantle becomes less buoyant in the lower crust, because the crust is less dense than the mantle. As a result, basalt tends to pond near the base of the crust. Partial melting of the lower crust by heat derived from ponded basalt generates silicic melts, which are buoyant enough to rise to the level of the sub-caldera rhyolite body. Inflation of the magma body causes surface uplift.

In summary, magmatic heat input is absolutely required to sustain Yellowstone's hydrothermal system over timescales longer than about 10^5

years, and there is ample evidence that basaltic magma has repeatedly intruded the crust in the vicinity of the Yellowstone Caldera since its formation 640,000 years ago. Accumulation of basalt, both near the base of the crust and beneath a sub-caldera zone of silicic partial melt, is the principal cause of uplift over such long timescales. It might also contribute to uplift over much shorter timescales, possibly even during historical time, but there are other mechanisms to consider before drawing that conclusion.

Another likely mechanism for historical uplift at Yellowstone is pressurization of the deep hydrothermal system, most likely as a consequence of rhyolitic magma crystallizing near the top of the magmatic system. Fournier and Pitt (1985) proposed that Yellowstone's hydrothermal system consists of a deep zone in which pore-fluid pressure is near lithostatic and a shallow zone in which pore pressure is hydrostatic. According to their model, the two zones are separated by an impermeable, self-sealing layer created by mineral deposition and plastic flow at a depth of about 5 km. Dzurisin *et al.* (1990) noted that the thermal energy carried to the surface at Yellowstone by convecting thermal water (4×10^{16} cal yr^{-1}) could be derived entirely from crystallization of 0.2 km^3 yr^{-1} of rhyolitic magma. Calculations by Fournier (1989) showed that if the magmatic fluid liberated upon crystallization of 0.2 km^3 yr^{-1} of rhyolitic magma initially containing 2 wt% water were trapped at lithostatic pressure, the net volume change at depth would be more than adequate to account for historical uplift rates measured by leveling surveys.

This mechanism is particularly appealing because it can account not only for Yellowstone's high convective heat flux and historical uplift rates, but also for episodic subsidence. If a self-sealed layer within the hydrothermal system ruptured during an earthquake swarm, the resulting depressurization and fluid loss would cause the overlying surface to subside. Subsidence would extend far beyond the epicentral area if, as suggested by Fournier and Pitt (1985), a state of hydraulic equilibrium prevails throughout the deep hydrothermal system. Thus, rupturing of the self-sealed layer *anywhere* might cause the entire caldera floor to subside. The 1978 and 1992 earthquake swarms might have been hydrofracturing events that released pressure and fluids from the deep hydrothermal system, allowing the caldera floor to subside. No subsidence was measured in the first case, presumably because uplift dominated between leveling surveys in 1976 and 1984.

The 1985 earthquake swarm near West Yellowstone seems enigmatic, because it occurred outside the caldera and might be explained by tectonic strain release in the vicinity of the Hebgen Lake fault zone. However, the swarm coincided with the onset of subsidence within the caldera and with two small hydrothermal explosions near the caldera rim. A possible link between the 1985 epicentral area and the sub-caldera hydrothermal system is suggested by results of regional trilateration surveys. Savage *et al.* (1993) showed that post-seismic strain accumulation in the epicentral area of the 1959 Hebgen Lake earthquake can be modeled as a 20-km-wide zone of extension approximately parallel to the 1959 rupture trace, extending at least 100 km S75°E to the vicinity of the Sour Creek resurgent dome (Figure 7.32). The hypothesized zone of extension is marked by: (1) a broad band of seismicity during the 1973–1988 interval; (2) the epicenters of the 1959 Hebgen Lake earthquake and the 1975 Yellowstone Park earthquake; (3) the epicentral areas of the 1985, 1978, and 1992 earthquake swarms; and (4) the sites of small hydrothermal explosions in 1985 and 1986, plus the emergence of a vigorous new mud volcano starting in early 1990. It passes a few kilometers south of Norris Geyser Basin, near the center of uplift detected by radar interferometry starting in 1997. Savage *et al.* (1993) noted that the zone cuts across the trend of major regional structures such as the Madison and Gallatin ranges, and that the evidence for extending the zone into the caldera is weak. However, if the zone *does* extend to the Sour Creek dome or beyond, it might provide a passageway for fluids to migrate from beneath the caldera to the 1985 swarm area, thereby depressurizing the hydrothermal system, inducing caldera subsidence, and accounting for the alignment of seismic and hydrothermal events noted above. At other times, its intersection with the caldera ring fracture system or with faults of the Norris–Mammoth corridor might be a preferred site for magmatic intrusion and surface uplift (e.g., uplift centered near Norris during 1997–2002).

This idea received additional support from Waite and Smith (2002), who noted that the 1985 earthquake swarm had several unusual characteristics indicative of interaction between seismicity and hydrothermal/magmatic activity. These include: (1) the swarm was roughly coincident with a reversal from uplift to subsidence inside the caldera; (2) swarm hypocenters occupied a nearly vertical north-

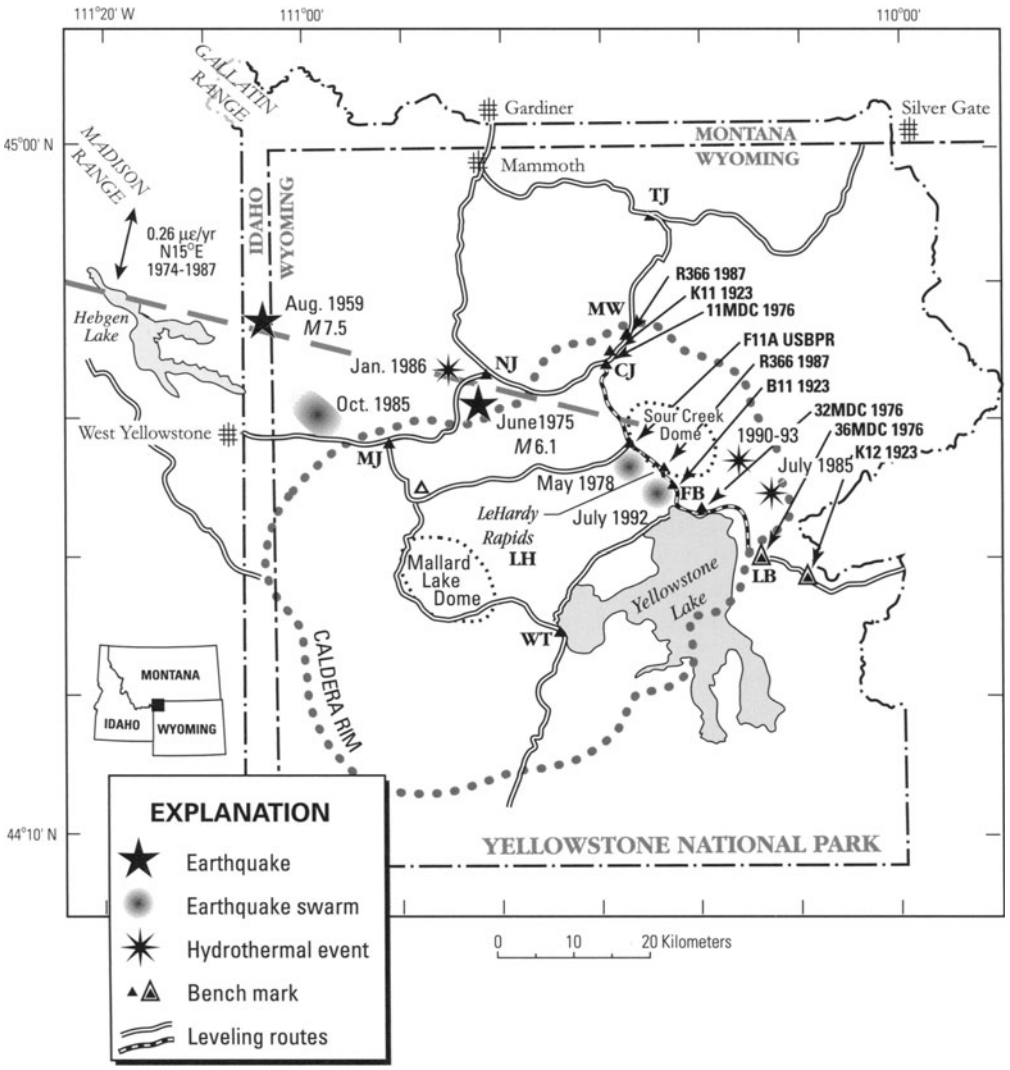

Figure 7.32. Yellowstone Caldera, leveling network, and a zone of extension inferred from trilateration measurements (Dzurisin *et al.*, 1994). Level line from Lake Butte (LB) to Canyon Junction (CJ) via LeHardys Rapids (LH) and Fishing Bridge (FB), shown as a short-dashed line with solid triangles representing key bench marks, was measured each year from 1983 to 1998 except for 1994, 1996, and 1997. Bold, long-dashed line represents a 20-km-wide zone of extension hypothesized by Savage *et al.* (1993), who described ground deformation in the Hebgen Lake area between 1974 and 1987 as roughly a uniaxial, 0.266 ± 0.014 microstrain/year, $N15°E \pm 1°$ extension that extends southeastward into the Yellowstone Caldera, possibly as far as the Sour Creek resurgent dome. Caldera rim (bold dotted outline) and resurgent domes (fine dotted outlines) after Christiansen (1984). MW, Mount Washburn; TJ, Tower Junction; NJ, Norris Junction; MJ, Madison Junction; WT, West Thumb. Reference bench marks 36MDC 1976 and K12 1923 are represented by solid triangles inside larger, open triangles.

west-trending zone, and during the first month of activity, the pattern of epicenters migrated laterally away from the caldera at an average rate of $150\,\mathrm{m\,day^{-1}}$; (3) the dominant focal mechanisms of the swarm were oblique-normal to strike-slip, contrasting with the normal-faulting mechanisms typical of the region; and (4) the maximum principal stress axis averaged for the swarm events was rotated 90 degrees from that of the normal background seismicity, from vertical to horizontal with a trend of 30 degrees from the strike of the plane defined by the swarm. Although Waite and Smith (2002) did not offer a unique explanation for the 1985 swarm, they proposed that the rate of lateral migration of the activity along a steeply dipping plane and the orientations of the principal stress axes are consistent with models of migration of magmatic or hydrothermal fluids. In their words (p. 2190 or ESE 1-14): '*The most likely scenario involves the rupture of a self-sealed hydrothermal*

layer and subsequent migration of hydrothermal fluid through a preexisting fracture zone out of the caldera.'

Three recent models based on ground deformation data suggest that the spatial patterns of uplift and subsidence are consistent with a source located at the depth and with the geometry of Yellowstone's deep hydrothermal system. Dzurisin *et al.* (1990) concluded that 1984–1987 leveling and trilateration data from the eastern part of the caldera were best fit by contraction of a horizontal tabular body located 10 ± 5 km beneath the Sour Creek resurgent dome. For the 1923–1976 uplift period, an inversion of the leveling data by Vasco *et al.* (1990) showed that the largest volume expansions were 3–6 km beneath each of Yellowstone's two resurgent domes. Meertens *et al.* (1992, 1993) showed that regional GPS data for 1987–1991 (a period when the caldera floor was subsiding) are best explained by deflation of two sub-horizontal, tabular bodies centered 3–6 km beneath the caldera floor, superimposed on a regional tectonic strain signal. They attributed the deflation to movement of hydrothermal or magmatic fluids.

It is useful to visualize these hypothetical deformation sources in the context of what is known about Yellowstone's upper crustal structure from seismic data. For example, Miller and Smith (1999) used first-arrival times from 7,942 local earthquakes and 16 controlled-source explosions (for which locations and origin times are known precisely) to model the 3-D P and S velocity structure beneath the caldera. They showed that a caldera-wide 15% decrease from regional P velocities at depths of 6 to 12 km is coincident with a −60 mGal Bouguer gravity anomaly, and they attributed both anomalies to a hot, subsolidus, granitic batholith with quasi-plastic rheology. Localized 30% reductions from regional seismic velocities and higher V_p/V_s ratios 8 km beneath the resurgent domes were interpreted as reflecting the presence of partial melts and vestigial magma systems. These latter anomalies correlate reasonably well with the two sources of deformation inferred by Vasco *et al.* (1990), Meertens *et al.* (1993), and Wicks *et al.* (1998).

Both the geodetic and seismic data point to the shallowest part of Yellowstone's magmatic system, or the deepest part of its hydrothermal system, as the source of contemporary crustal deformation. The data are not sufficiently precise to distinguish between these two sources, and in fact both may be involved, contributing to varying degrees at different times. Although the geodetic models differ in detail, all are consistent with the idea that (1) caldera uplift from 1923 to 1984 was caused at least partly by pressurization of the hydrothermal system below a self-sealed layer about 5 km deep, and (2) subsidence since 1984 was caused primarily by rupturing of the layer during shallow earthquake swarms. In addition, the regional GPS data indicate that sagging of the caldera floor in response to regional crustal extension contributed to the subsidence measured since 1984. Surface uplift centered near Norris Geyser Basin during 1997–2002 might be evidence for episodic intrusion of magma into the crust beneath the caldera. Such intrusions *must* occur from time to time to sustain Yellowstone's vigorous hydrothermal system over long timescales. Deeper intrusions might be aseismic and difficult to detect geodetically without using continuous GPS (CGPS) or InSAR. So it is possible that magmatic intrusions also contributed to the uplift measured at Yellowstone between 1923 and 1984.

The evidence from temporal gravity changes is consistent with this idea but equivocal. Smith *et al.* (1989) noted that the gradient determined at more than 100 precision-gravity and leveling stations in Yellowstone for 1977–1987, a period that was dominated by surface uplift, was significantly less than the theoretical free-air gradient ($-1.7\ \mu\text{Gal cm}^{-1}$ *versus* $-3.086\ \mu\text{Gal cm}^{-1}$). This suggests a net mass increase beneath the caldera during this period (Section 2.7.1), presumably an intrusion of hydrothermal fluid or magma, but the density of the intrusion is poorly constrained. Arnet *et al.* (1997) extended the observations through 1994 and came to a similar conclusion. During a period of uplift from 1977 to 1983, the gravity field decreased across the caldera by as much as $-60 \pm 12\ \mu$Gal. The observed gradient could not have been caused solely by pressurization of the deep hydrothermal system, without any significant mass increase. The authors (p. 2744) attributed the changes to '... *widespread hydrothermal fluid movement, which furthermore is related to input by magma.*' From 1986 to 1993, while the caldera floor subsided, the gravity field increased by as much as $60 \pm 12\ \mu$Gal and the $(\Delta g/\Delta h)$ gradient was near the theoretical free-air gradient. This indicates that subsidence was not accompanied by a measurable mass change, which Arnet *et al.* (1997, p. 2744) attributed to '... *depressurization of the deep hydrothermal system as a result of fracturing and volatile loss to the shallow hydrothermal system or, less likely, reduced input of brine to the deep system.*' They preferred the first mechanism

because it more easily explains the relatively abrupt change from uplift to subsidence between 1984 and 1986 (Dzurisin *et al.*, 1990).

The June–July 1995 earthquake swarm near Madison Junction remains enigmatic, because it coincided with the resumption of uplift that was first detected with InSAR and later verified by leveling. None of the models described above easily accounts for the fact that the most intense swarm ever recorded in the Yellowstone region (starting in October 1985) coincided with the beginning of subsidence, while the second most intense swarm (June–July 1995) coincided with the resumption of uplift. Clearly, we still have much to learn from Earth's largest restless caldera.

7.3.5 Spatiotemporal changes in deformation revealed by InSAR

As described in Chapter 5, the most recent advance in our understanding of ground deformation at Yellowstone came not from leveling surveys, but from InSAR observations starting in 1992. Radar interferograms for the periods 1992–1993 and 1993–1995 agree reasonably well with leveling results along the traverse from Lake Butte to Mount Washburn (Wicks *et al.*, 1998). However, the InSAR data also show that the center of subsidence shifted from the northeast part of the caldera, near the Sour Creek resurgent dome, during 1992–1993, to the southwest part, near the Mallard Lake dome, during 1993–1995. What is more, while the Mallard Lake dome was still subsiding, the Sour Creek dome began to rise during 1995–1996 for the first time since 1983–1984. Uplift was occurring throughout most of the caldera by 1997, but by 2000 the central part of the caldera floor was subsiding again, while a broad area centered near Norris was rising (Wicks *et al.*, 2005).

The rapidity of the change from uplift to subsidence within the caldera before and after 1984–1985, and from subsidence to uplift again from 1993–1995 to 1995–1996 suggests that the process responsible for these displacements is relatively shallow-seated and reversible. The same argument applies to the rapid lateral migration of the center of subsidence from 1992–1993 to 1993–1995. Thus, it seems implausible that changes of this magnitude could occur so quickly and reversibly if they are primarily driven by deep-seated magmatic or regional tectonic processes. Rather, the most likely source of historical surface displacements within the Yellowstone Caldera is the deep hydrothermal system, which apparently is capable of pressurizing and depressurizing over timescales of years to decades. Because uplift of the Sour Creek dome began while the Mallard Lake dome was still subsiding and the Mallard Lake dome caught up within the next year, I imagine some sort of sluggish fluid connections that convey pressure changes within the lowermost part of the hydrothermal system and perhaps the uppermost part of the magmatic system.

The fact that uplift and subsidence occur at approximately the same rate, when averaged over several years, suggests that the rate of pressure change is regulated in some way, perhaps by the complexity of the fluid pathways. Like an inflatable raft with a small inlet/outlet port, Yellowstone's hydrothermal system may inflate and deflate – essentially 'breathe' – only very slowly in most cases. Catastrophic ruptures are probably associated with large hydrothermal explosions, which are responsible for several craters and associated ejecta deposits throughout the Yellowstone Caldera. At least some of these formed when glacially dammed lakes suddenly drained, abruptly decreasing the confining pressure on the shallow hydrothermal system and triggering explosions (Muffler *et al.*, 1971).[6] Even if the hydrothermal system is responsible for most of the vertical surface displacements observed at Yellowstone in recent decades, over longer timescales magmatic intrusions undeniably play an important role as well. The recent uplift episode near Norris Geyser Basin would seem to be a case in point.

7.4 LONG VALLEY CALDERA AND THE MONO-INYO VOLCANIC CHAIN: TWO DECADES OF UNREST (AND STILL COUNTING?)

7.4.1 Eruptive history and recent unrest

Among the most detailed and long-term geodetic datasets available for any volcanic system on Earth is that for the Long Valley Caldera and nearby

[6] Muffler *et al.* (1971) identified ten hydrothermal explosion craters in Yellowstone National Park ranging in diameter from a few tens of feet (~10 m) to about 5,000 feet (1,500 m). Geologic relations at the Pocket Basin crater, in the western part of the Park about 7 miles (11 km) north of Old Faithful (Figure 7.29), indicate that the explosion there was triggered by an abrupt decrease in confining pressure when an ice-dammed lake suddenly drained during the waning stages of early Pinedale Glaciation about 15,000 years ago. The authors suggested that most of the other explosion craters in the Park could have formed in the same manner.

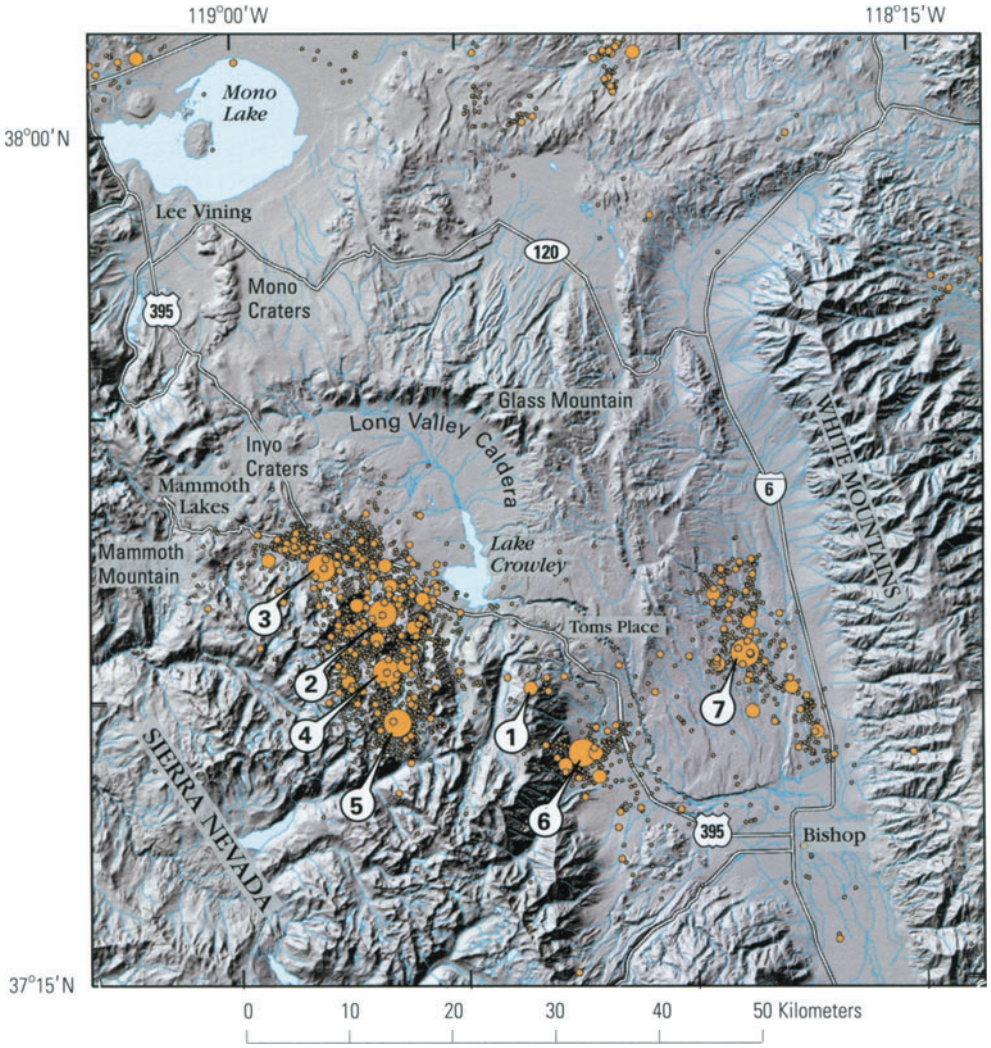

Figure 7.33. Shaded-relief map of the Long Valley Caldera–Mono Craters region showing the epicenters of $M \geq 3$ earthquakes (orange circles) for 1978–1999. Circle sizes represent earthquake magnitude in four steps from $M = 3.0$ to $M = 6.0$. Earthquakes discussed in the text include: (1) 4 October 1978 M 5.8 Wheeler Crest earthquake; (2–5) 25–27 May M ~6 Long Valley Caldera and Sierra Nevada earthquakes; (6) 23 November 1984 M 6.0 Round Valley earthquake; and (7) 21 July 1986 M 6.4 Chalfant Valley earthquake. Figure modified slightly from Hill *et al.* (2002a).

Mono-Inyo Craters volcanic chain in eastern California (Figure 7.33). The Long Valley Caldera is a 32 km × 17 km elliptically shaped depression that formed about 730,000 years ago when the roof of a large crustal magma reservoir ruptured catastrophically and collapsed, resulting in the expulsion of 600 km^3 of rhyolitic magma (Bailey *et al.*, 1976; Bailey, 1989, 2004). The resulting ash flow deposits, known as the Bishop Tuff, inundated 1,500 km^2 of the surrounding countryside and accumulated locally to a thickness approaching 200 m (Figure 7.34). Some ash flows spilled westward over the crest of the Sierra Nevada, and within the caldera they locally ponded to a thickness of more than 1,500 m. Plinian ash clouds associated with the eruption drifted thousands of kilometers downwind, depositing an ash layer that is still recognizable as far east as Kansas and Nebraska, more than 1,000 km away (Izett *et al.*, 1970; Izett, 1982). Thinner Bishop Ash deposits have been recognized in southwest California (Merriam and Bischoff, 1975) and in Pacific Ocean seafloor cores (Sarna-Wojcicki *et al.*, 1987).

Following collapse, eruptions continued within the 2- to 3-km-deep Long Valley Caldera for a few tens of thousands of years. Early postcaldera pyroclastic eruptions formed a thick sequence of intracaldera bedded tuffs that were followed by

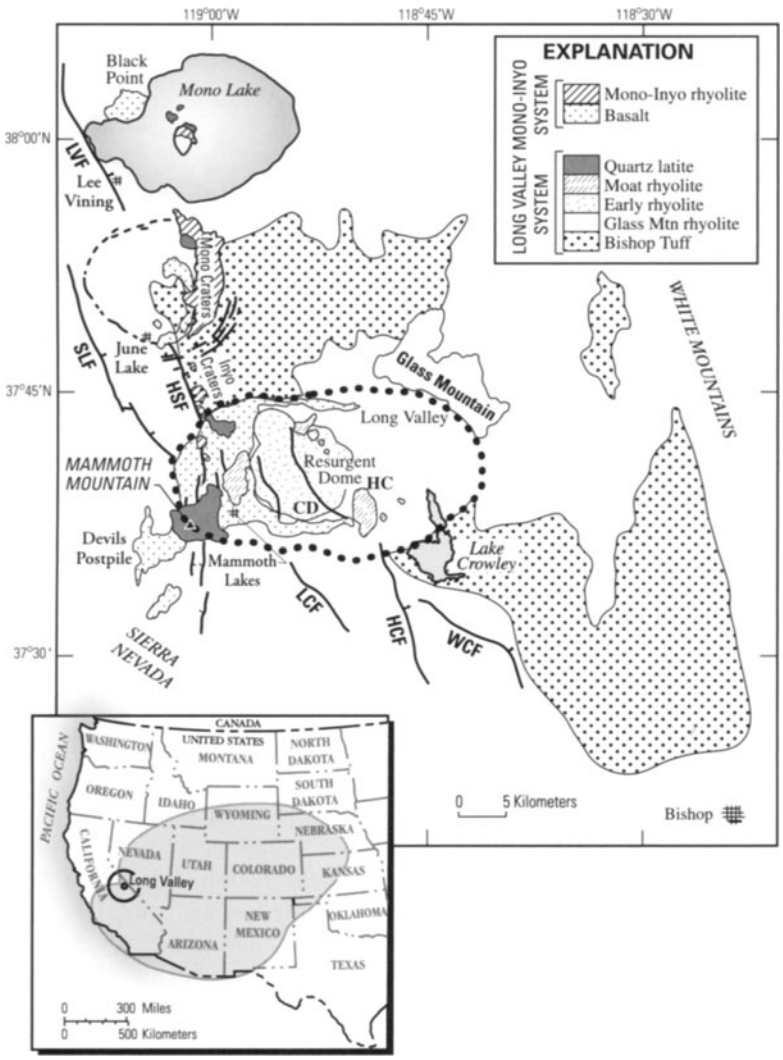

Figure 7.34. Simplified geologic map of the Long Valley region showing the distribution of volcanic rocks related to the Long Valley Caldera magmatic system and the younger Mono-Inyo magmatic system, after Bailey *et al.* (1976) and Bailey (2004). The Bishop Tuff is a welded ash flow deposit from the caldera-forming eruption 730,000 years ago. It is mostly buried by younger deposits in the vicinity of the caldera. (*Inset*) The approximate distribution of airfall ash from the caldera-forming eruption. LVF, Lee Vining fault; HSF, Hartley Springs fault; LCF, Laurel Creek fault; HCF, Hilton Creek fault; SLF, Silver Lake fault; WCF, Wheeler Crest fault (also known as Round Valley fault); CD, Casa Diablo; HC, Hot Creek.

extrusion of hot, fluid obsidian flows known collectively as the early rhyolites. Contemporaneously, renewed magma pressure at depth uplifted, arched, and faulted the central part of the caldera floor, forming a resurgent dome about 10 km in diameter and 500 m high. Early rhyolites exposed in the dome are tilted radially outward as much as 30 degrees, attesting to the intensity of deformation caused by magmatic resurgence and structural adjustments to caldera formation. Eruption of the early rhyolites and formation of the resurgent dome occurred rapidly, within 100,000 years or less after caldera collapse (Bailey, 1989).

During the rise of the resurgent dome and eruption of the early rhyolites, a large lake filled the caldera. Continued rise of the resurgent dome eventually raised the lake surface to the level of the low southeast caldera rim, where erosive overflow subsequently cut the spectacular Owens River Gorge (Figure 7.35). Glaciers flowing into the lake from the High Sierra Nevada generated debris-laden icebergs that drifted across the lake, depositing large erratics of Sierran granite on the flanks of the resurgent dome, which stood as an island until the lake drained between 100,000 and 50,000 years ago (Bailey, 1989).

Figure 7.35. The Owens River Gorge in eastern California, which was cut when resurgent doming within the Long Valley Caldera raised the surface of an intracaldera lake to the level of the low southeast caldera rim (Bailey, 1989).
USGS photograph by David E. Wieprecht.

After a pause of about 100,000 years, crystal-rich rhyolite began erupting from three groups of vents in the caldera moat peripheral to the resurgent dome. The moat rhyolites erupted at about 200,000-yr intervals – approximately 500,000, 300,000, and 100,000 years ago (Figure 7.34). Bailey and others (1976) speculated that the coarse crystallinity, presence of hydrous minerals, and relatively high vesicularity of the moat rhyolites may reflect their origin as residual magma from the caldera-forming eruption. Cooling and crystallization of residual magma concentrated volatiles and increased pressure in the magma reservoir to the extent that the ring-fracture system was repeatedly reactivated and served as a conduit to the surface for the moat rhyolite magmas.

The younger Mono-Inyo Craters volcanic chain is localized along a narrow, north-trending fissure system that extends 45 km northward from south of Mammoth Mountain through the west moat of Long Valley Caldera to the north shore of Mono Lake (Figure 7.36). This system began by erupting basalt and andesite from vents in and around the west moat of Long Valley Caldera, including those at Devil's Postpile National Monument, about 300,000 years ago. Between 200,000 and 50,000 years ago, extrusion of at least 12 rhyolite domes and flows built Mammoth Mountain, which straddles the southwest caldera rim and hosts a popular ski resort (Figure 7.37) (Bailey, 1989).

Rhyolites began erupting to form the Mono-Inyo Craters about 40,000 years ago, first at the Mono Craters and later at the Inyo Craters. The Mono Craters comprise an arcuate chain of 30 or more overlapping rhyolite domes, flows, and craters, apparently fed from the margin of a sub-circular pluton that may still be partly molten. The Inyo Craters form a discontinuous 10-km-long line of rhyolite dome-flows and craters within and immediately north of the caldera's west moat. During the past 3,000 years, the Mono-Inyo Craters have erupted at intervals of 700 to 250 years, the most recent eruptions being from Panum Crater and the Inyo Craters 650–550 years ago (Miller, 1985; Sieh and Bursik, 1986), and from Paoha Island about 250 years ago (Stine, 1990) (Figure 7.36). Research drilling beneath the Mono Craters and detailed stratigraphic studies of associated tephra deposits have shown that the eruption 650–550 years ago produced five separate dome-flows and several phreatic explosion craters, all within a span of probably no more than a few years, or possibly months, and all originating from a single dike (Eichelberger *et al.*, 1985).

Against this backdrop of frequent eruptions in the recent geologic past, a period of relative seismic quiescence that followed a sequence of M 5.5 to 6.0 earthquakes in 1941 near Tom's Place ended on 4 October 1978, when the M 5.8 Wheeler Crest earthquake struck midway between the towns of Bishop and Mammoth Lakes (Figure 7.33). Clusters of small to moderate ($M > 4$) earthquakes generally migrated northwestward toward the caldera until, on 25–27 May 1980, four $M \sim 6$ earthquakes and an intense swarm of smaller events shook the region. Two more comparably sized events struck the region on 23 November 1984 (M 6.0 Round Valley earthquake) and 21 July

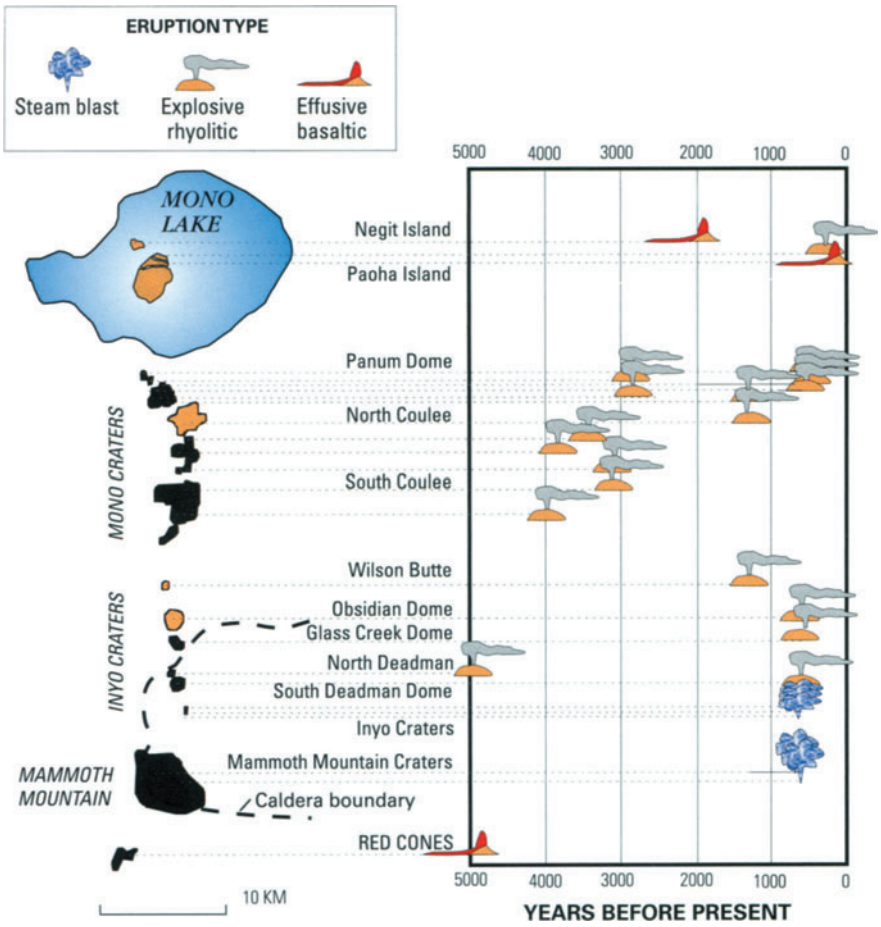

Figure 7.36. Eruptive history of the Mono-Inyo Craters volcanic chain for the past 5,000 years, from Hill *et al.* (2002a). The Mono Craters consists of 30 or more overlapping rhyolite domes, flows, and craters. An eruption 650–550 years ago formed Panum Dome and the Inyo Craters to the south. The most recent eruption, from vents on the floor of Mono Lake, formed Paoha Island about 250 years ago. Dashed line shows part of the caldera boundary.

1986 (*M* 6.4 Chalfant Valley earthquake). Frequent earthquake swarms, notably in 1983 (south moat), 1989–1991 (Mammoth Mountain), 1997–1998 (south moat), and 1998–1999 (Sierra Nevada) were accompanied by about 80 cm of uplift of the resurgent dome, changes in the shallow hydrothermal system, and increased emission of magmatic CO_2 in the vicinity of Mammoth Mountain (Hill, 1984, 1996; Hill *et al.*, 1990, 2002a, 2002b, 2003).

Because any recurrence of eruptive activity in the Long Valley area would pose a substantial threat to the community of Mammoth Lakes, to regional communications and transportation infrastructure, and to commercial air traffic (e.g., Miller *et al.*, 1982), the USGS conducts an intensive monitoring program through its Long Valley Observatory (LVO). As a result, there exists a detailed record of the unrest that has persisted for more than two decades, including repeated leveling, EDM, and GPS surveys, plus continuous data from arrays of tiltmeters, strainmeters, magnetometers, and GPS stations (Hill and Prejean, 2005). Some of the geodetic datasets are discussed individually in other chapters. Here, I briefly review the leveling, trilateration, and GPS results to illustrate the effectiveness of a thorough geodetic program for studying volcanic unrest, especially in conjunction with other monitoring techniques integrated in an observatory environment.

The May 1980 earthquake swarm at Long Valley, which ranks among the most intense episodes of non-eruptive unrest ever recorded at an active magmatic system, prompted immediate re-surveys of regional leveling and trilateration networks to help determine the cause of the activity and its implications for earthquake and volcano hazards.[7] The results showed unequivocally that

[7] The intense earthquake swarm at Long Valley, including four *M* 6 shocks during 25–27 May 1980, came little more than a week after the catastrophic eruption of Mount St. Helens on 18 May. There is no plausible connection between the two events, separated as they were by 1,000 km, and in hindsight their timing was almost surely coincidental. For those of us struggling to cope with Mount St. Helens at the time, however, the news from Long Valley was unsettling – an eerie reminder of how little we understood about volcanoes and how they behave.

Figure 7.37. Mammoth Mountain as seen looking west from EDM station CASA near the south edge of the resurgent dome at Long Valley Caldera. Mammoth Mountain rises steeply above the Town of Mammoth Lakes, which is visible near the center of the photograph. Jagged peaks to the right of Mammoth Mountain are the Minarets of the Sierra Nevada. The major road leading to Mammoth Lakes is California Highway 203, which intersects US Highway 395 in the lower left portion of the photograph. Dead vegetation immediately northeast of the intersection was killed by recent changes in the Casa Diablo geothermal area, which is tapped by three geothermal power plants with a combined rating of 40 Megawatts (*lower right*).
USGS photograph by Elliot T. Endo, 14 August 2003.

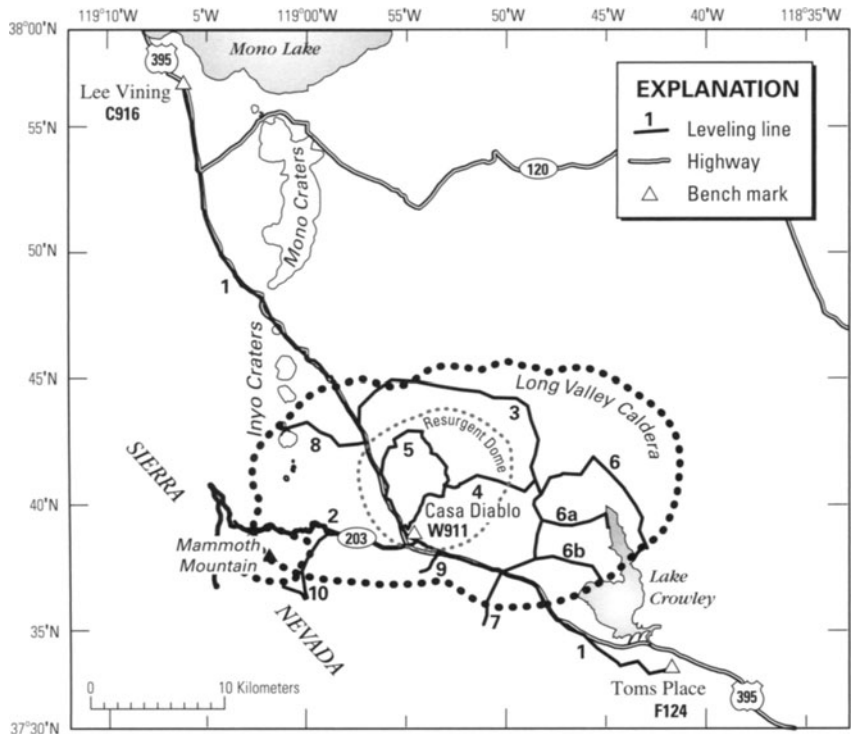

Figure 7.38. Leveling network (heavy solid lines) used to monitor vertical displacements within and around Long Valley Caldera (Hill *et al.*, 2002a). Numbers identify individual leveling loops or lines following the convention used by Savage *et al.* (1987). Bench marks C916 near Lee Vining and F124 near Toms Place are reference marks. Bench mark W911 near Casa Diablo is close to the point of maximum uplift along Highway 395. See text for discussion. The configurations of other types of monitoring networks at Long Valley (e.g., seismic stations, borehole strainmeters and tiltmeters, CGPS stations, CO_2 and hydrologic monitoring sites) are shown elsewhere by Hill *et al.* (2002a) and Dzurisin (2003).

the long-dormant magmatic system beneath Long Valley Caldera was involved in the unrest. Subsequent activity and ongoing investigations have confirmed the potential for renewed eruptive activity, and the recent geologic record points to the Mono-Inyo Craters volcanic chain as the most likely site of the next eruption in the region (Miller *et al.*, 1982; Hill *et al.*, 1985a,b).

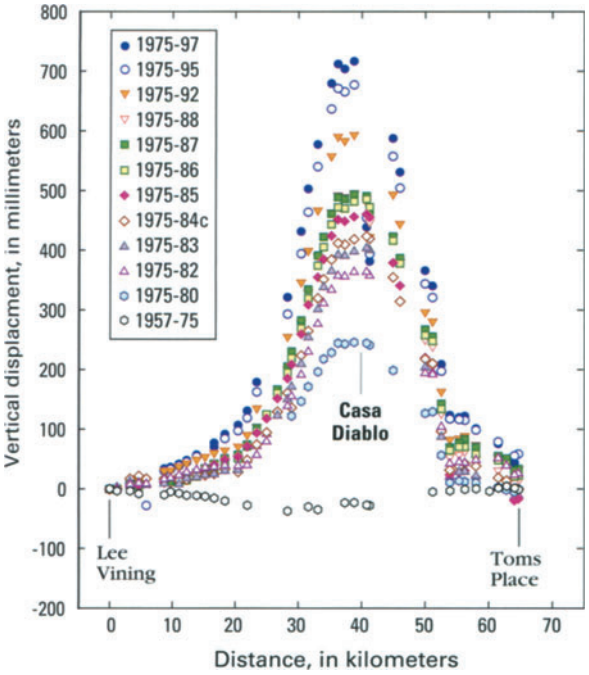

Figure 7.39. Results of first-order leveling surveys across Long Valley Caldera along Highway 395 between Lee Vining and Toms Place from 1957 to 1997. Following an intense earthquake swarm that included four *M* 6 events on 25--27 May 1980, leveling in October 1980 revealed nearly 25 cm of uplift centered at the resurgent dome near Casa Diablo since the previous survey in 1975. Uplift continued at a gradually declining rate through October 1989, when two-color EDM measurements revealed an increase in the extensional strain rate about 2 months prior to the start of a prolonged earthquake swarm beneath Mammoth Mountain on the caldera's southwest rim. Subsequent leveling surveys in 1992, 1995, and 1997 also show the effects of renewed caldera inflation. The 1984 leveling survey was contaminated by a systematic error that produced a large apparent tilt between Lee Vining and Toms Place, which has been removed from the data shown here (1984c). The dome subsided about 2 cm from early 1999 through the end of 2001, but that change was largely offset by renewed uplift starting in early 2002. Uplift stopped again in early 2003. Since then, the dome has shown only minor fluctuations in height and remains roughly 80 cm higher than in the late 1970s (current as of January 2006).

7.4.2 Leveling results: tracking caldera inflation in space and time

The first clear evidence that magma was involved in the unrest at Long Valley came from re-surveys in 1980 of a first-order leveling traverse along US Highway 395, which crosses the caldera's west moat and resurgent dome, and of a regional trilateration network designed primarily to measure tectonic strain (Savage and Clark, 1982). The Highway 395 leveling traverse between Lee Vining and Toms Place was measured partly or entirely in 1932, 1957, 1975, 1980, annually from 1982 to 1988, 1992, 1995, and 1997. No significant vertical displacements occurred from 1932 to 1975, but from 1975 to 1997 (probably starting sometime after July 1979, see below), a broad area centered on the resurgent dome rose cumulatively almost 80 cm (Figures 7.38 and 7.39).

When the traverse was first remeasured 5 months after the May 1980 earthquake swarm, bench mark W911 near Casa Diablo had risen about 25 cm since the previous survey in 1975. It rose an additional 12 cm between surveys in 1980 and 1982, and continued to rise at a slowly declining rate through 1988 (Figures 7.39 and 7.40). Two-color EDM measurements made every few days detected an increase in the rate of extension across the resurgent dome starting in October 1989 (Langbein *et al.*, 1993), and a corresponding increase in the uplift rate was measured by leveling surveys along Highway 395 in 1992, 1995, and 1997.

More extensive leveling surveys along a network of roads mostly within the Long Valley Caldera (Figure 7.38) were conducted in 1975, then annually from 1982 to 1986, 1988 and 1992. Because the network is sufficiently dense, vertical displacements

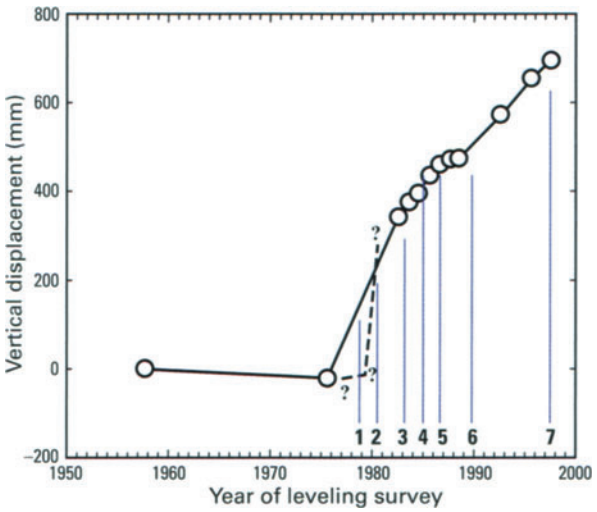

Figure 7.40. Progressive uplift of bench mark W911 near Casa Diablo with respect to bench mark C916 near Lee Vining from leveling surveys in 1957, 1975, 1982–1988, 1992, 1995, and 1997. A 1980 survey did not include C916, but W911 rose 250 mm with respect to F124 near Toms Place from 1975 to 1980 (dotted line). See Figure 7.38 for bench mark locations. (1) 4 October 1978 *M* 5.8 Wheeler Crest earthquake; (2) 25–27 May 1980 earthquake swarm including four *M* ~6 events; (3) January 1983 south moat earthquake swarm including two *M* 5 earthquakes; (4) 23 November 1984 *M* 6.0 Round Valley earthquake; (5) 21 July 1986 *M* 6.4 Chalfant Valley earthquake; (6) 1989–1991 Mammoth Mountain earthquake swarm and renewed caldera inflation; and (7) 1997–1998 south moat earthquake swarm and renewed caldera inflation.

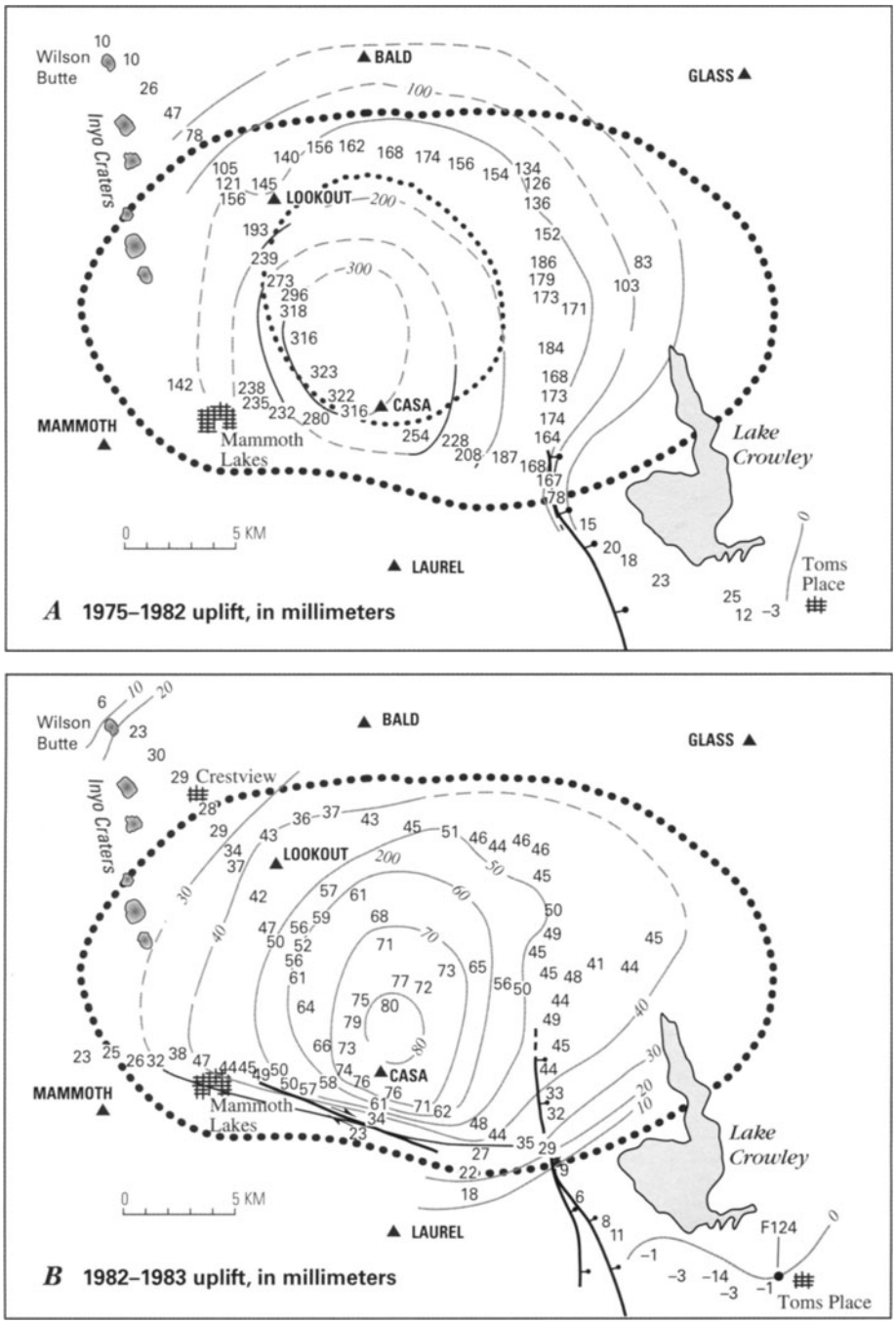

Figure 7.41. Contour maps showing uplift within Long Valley Caldera for the following periods: (A) 1975–1982; (B) 1982–1983; (C) 1983–1985; and (D) 1982–1985 (Savage *et al.*, 1987). Numbers show amounts of uplift, in millimeters, relative to bench mark F124 near Toms Place, which was assumed to have remained fixed. C916 near Lee Vining, not F124, was assumed to have remained fixed for Figures 7.39 and 7.40. Resulting differences are small compared with the amount of uplift within the caldera. The apparent westward shift of the center of uplift during 1983--1985 could be an artifact of relative rod-scale error. Triangles represent trilateration stations (see also Figure 7.43).

between surveys can be contoured to delineate both the spatial extent of the displacement field and any changes in its shape as a function of time (Figure 7.41). Such information provides a strong constraint on deformation-source models, especially in conjunction with contemporaneous data on horizontal displacements (e.g., Castle *et al.*, 1984; Savage *et al.*, 1987; Langbein *et al.*, 1995; Langbein, 2003).

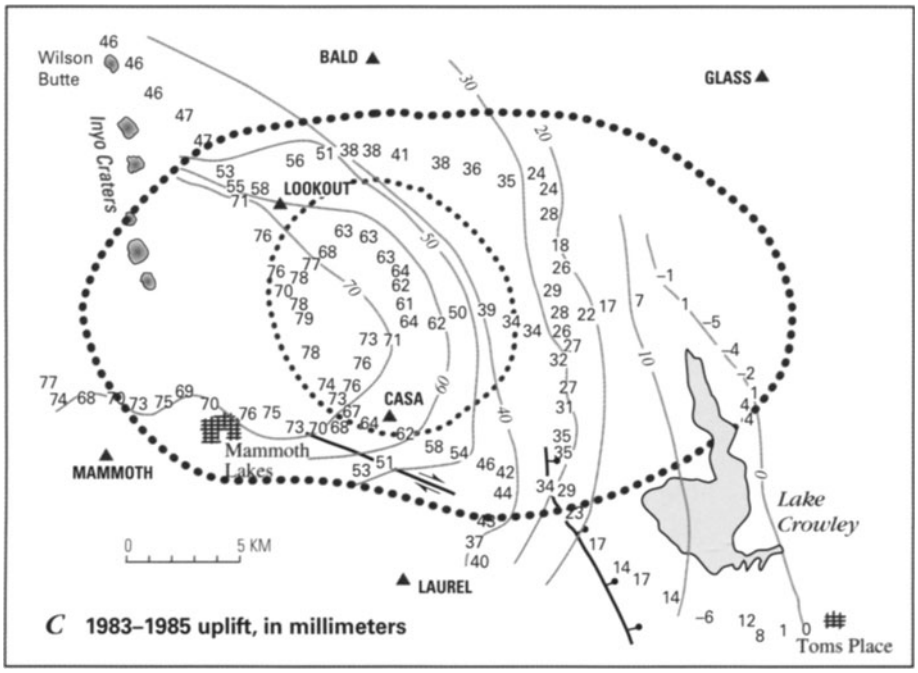

C 1983–1985 uplift, in millimeters

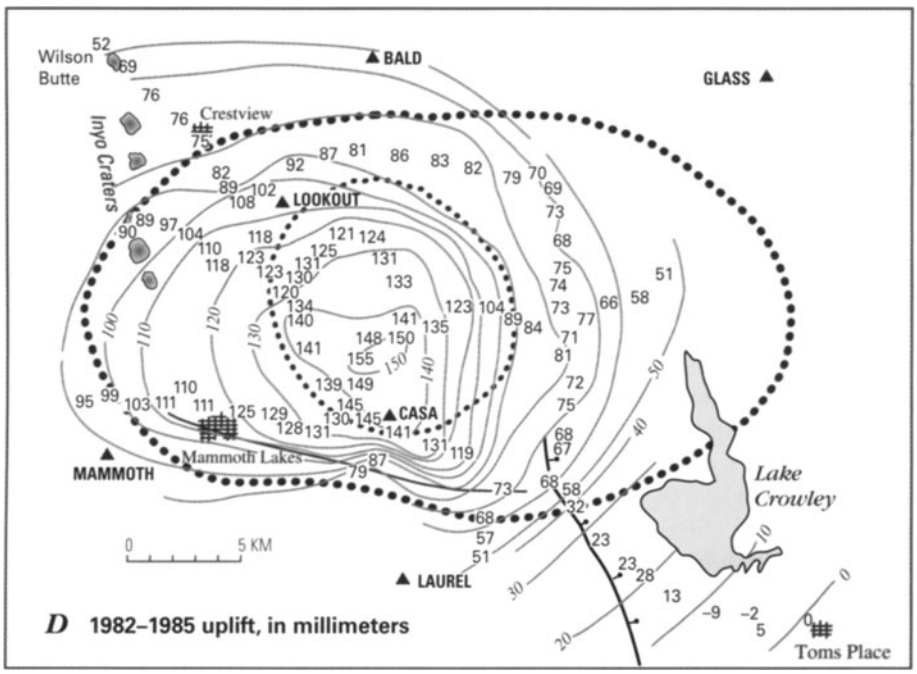

D 1982–1985 uplift, in millimeters

7.4.3 Regional and intracaldera trilateration surveys

Horizontal deformation at Long Valley has been measured with two types of precise EDM surveys: regional trilateration using a Geodolite starting in 1972, and intracaldera trilateration with a two-color EDM starting in 1983. Both approaches have yielded important insights into the processes responsible for unrest. Regional surveys in 1972, 1973, 1976, 1979, and 1980 revealed that a distinctive pattern of outward-radial displacements centered at Long Valley Caldera developed sometime between

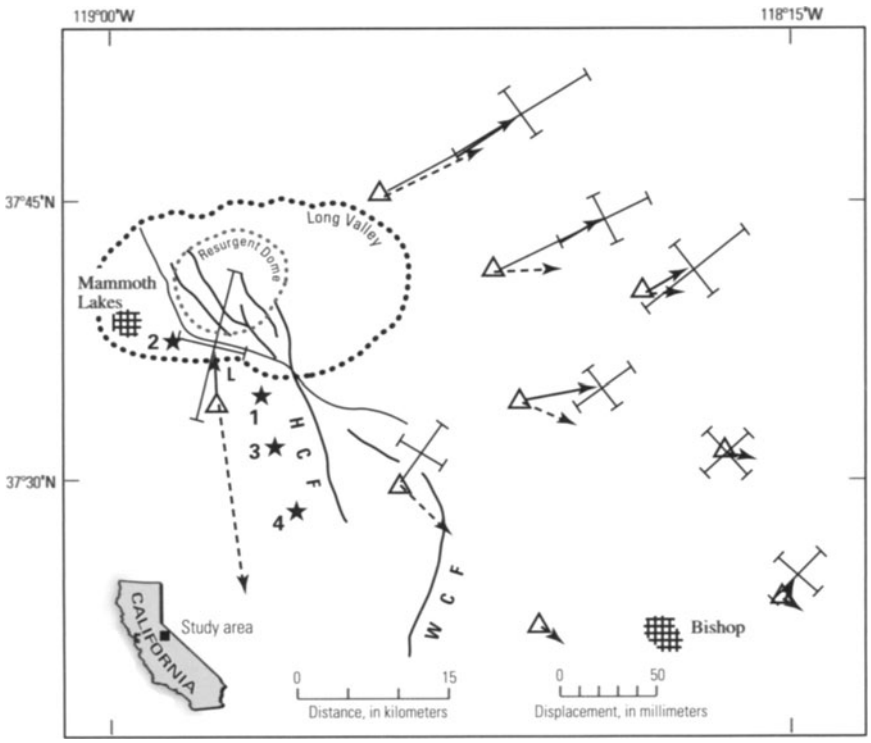

Figure 7.42. Horizontal displacement vectors determined by trilateration surveys near Long Valley Caldera in July 1979 and September 1980 (Savage and Clark, 1982). Dotted ellipse, Long Valley Caldera rim; smaller dotted circle, resurgent dome; triangles, trilateration stations; solid arrows, observed displacements with error bars showing principal axes of 95% confidence ellipse for each displacement vector; dashed arrows, model displacements predicted by inflation of a spherical magma body located 10 km beneath the caldera; stars, epicenters of four $M\sim6$ earthquakes on 25–27 May 1980, numbered in order of occurrence; HCF, Hilton Creek fault; WCF, Wheeler Crest fault (also known as Round Valley fault, e.g., Bailey, 2004).

July 1979 and September 1980 (Figure 7.42). Recall that leveling surveys along Highway 395 detected the beginning of uplift sometime between 1975 and October 1980. Savage and Clark (1982) concluded that the most likely cause of extension and uplift was inflation of a magma body located about 10 km beneath the caldera starting sometime after July 1979, just before or during the May 1980 earthquake sequence.

The same pattern of uplift and radial extension continued for several years at a gradually declining rate, as documented by annual leveling and Geodolite surveys from 1982 to 1986 (Figures 7.39, 7.40, 7.43–7.45). Savage *et al.* (1987) concluded: (1) the principal deformation sources were inflation of a magma body beneath the resurgent dome and right-lateral strike-slip on a vertical fault in the south moat of the caldera; (2) the inflation rate was roughly constant at $0.02\,km^3\,yr^{-1}$, but the slip rate on the south moat fault decreased substantially after the January 1983 earthquake swarm; and (3) there is evidence for a source of dilatation (possibly dike intrusion) beneath the south moat in 1983 and less certain evidence for a deep source (possibly magmatic inflation beneath Mammoth Mountain) in the western caldera during 1983–1985. The latter possibility was strengthened by the occurrence of a prolonged earthquake swarm beneath Mammoth Mountain in 1989–1990, which Hill *et al.* (1990) attributed to an intrusion of basalt into the upper crust.

By the early 1980s, regional leveling and trilateration surveys at Long Valley clearly showed that the locus of ground deformation was inside the caldera, beneath the resurgent dome and south moat. To better study the source area, more detailed and frequent geodetic measurements were required. Following a particularly intense earthquake swarm and possible dike intrusion beneath the south moat in January 1983, a dense trilateration network was established in the south moat in June 1983 and expanded by 1985 to cover the resurgent dome and western half of the caldera (Langbein, 1989, 2003) (Figure 7.46). A two-color EDM with a precision of 0.1 – 0.2 ppm (1–2 mm for a 10-km baseline) is used to measure several of the 42 baselines every few days, weather permitting, and the rest of the network monthly or yearly. The resulting record might be the most detailed and precise long-term, time series geodetic dataset ever obtained at a restless volcano.

The two-color EDM results clearly show that extensional strain rates in the south moat gradually decreased from as high as 5 ppm yr^{-1} several months

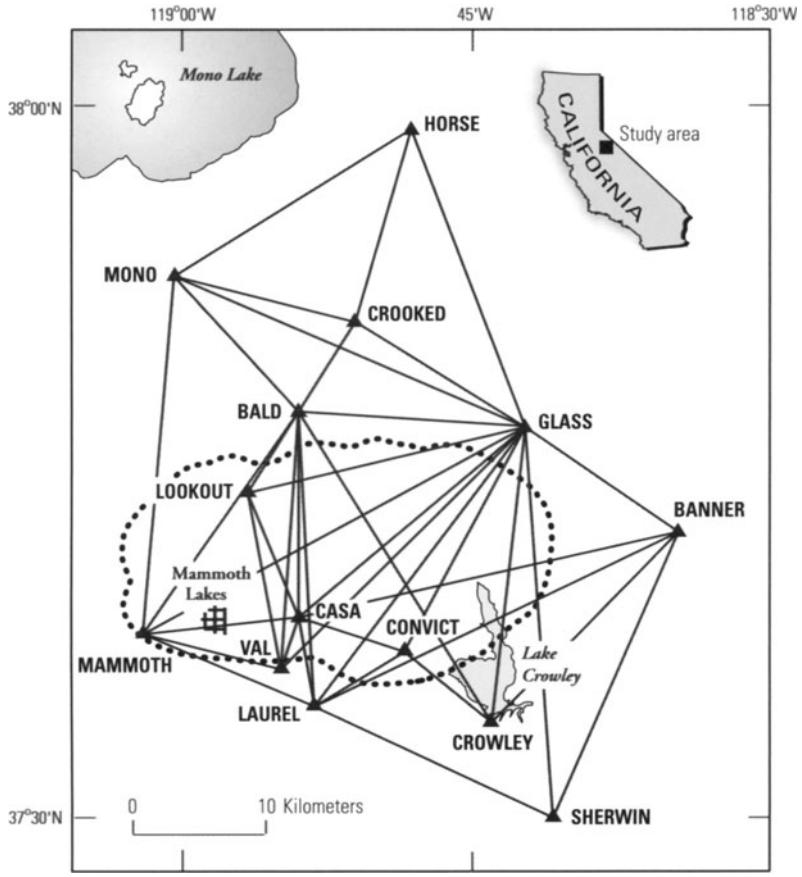

Figure 7.43. Long Valley regional trilateration network (Savage *et al.*, 1987).

after the January 1983 earthquake swarm to near zero in mid-1989 (Langbein *et al.*, 1993; Langbein, 2003). Then, starting in October 1989, a remarkable thing happened. Extension rates increased to as high as 9 ppm yr^{-1} over a period of a few weeks, while the level of earthquake activity beneath the south moat and elsewhere in the caldera remained low (Figure 7.47). About 2 weeks later, a subtle increase in the occurrence of small earthquakes beneath Mammoth Mountain was noted. This area had been relatively quiet since the beginning of unrest more than a decade earlier. Earthquake activity beneath the caldera picked up several weeks later, in December 1989, and continued at an elevated level through 1991. The two-color EDM results clearly foretold increases in earthquake activity beneath Mammoth Mountain and the caldera, but what processes were at work to cause the earthquakes?

There is compelling evidence that seismicity beneath Mammoth Mountain during 1989–1990 was caused by an intrusion of magma into the upper crust. Renewed inflation beneath the caldera starting several weeks later probably was caused by a separate intrusion into the reservoir located about 6 km beneath the resurgent dome. Evidence for an intrusion beneath Mammoth Mountain includes (Hill, 1996):

(1) a dike-like distribution of hypocenters at depths of 6–9 km with a north–northeast strike essentially perpendicular to the *T*-axes of the earthquake focal mechanisms (Hill *et al.*, 1990);
(2) deformation in the vicinity of Mammoth Mountain consistent with a north–northeast-striking dike extending to within 2 km of the surface beneath Mammoth Mountain (Langbein *et al.*, 1993);
(3) frequent spasmodic bursts suggesting rapid-fire brittle failure driven by transient surges in local fluid pressure (Hill *et al.*, 1990);
(4) an increase in $^{3}He/^{4}He$ ratios from fumaroles on Mammoth Mountain detected in late 1989 (Sorey *et al.*, 1993);

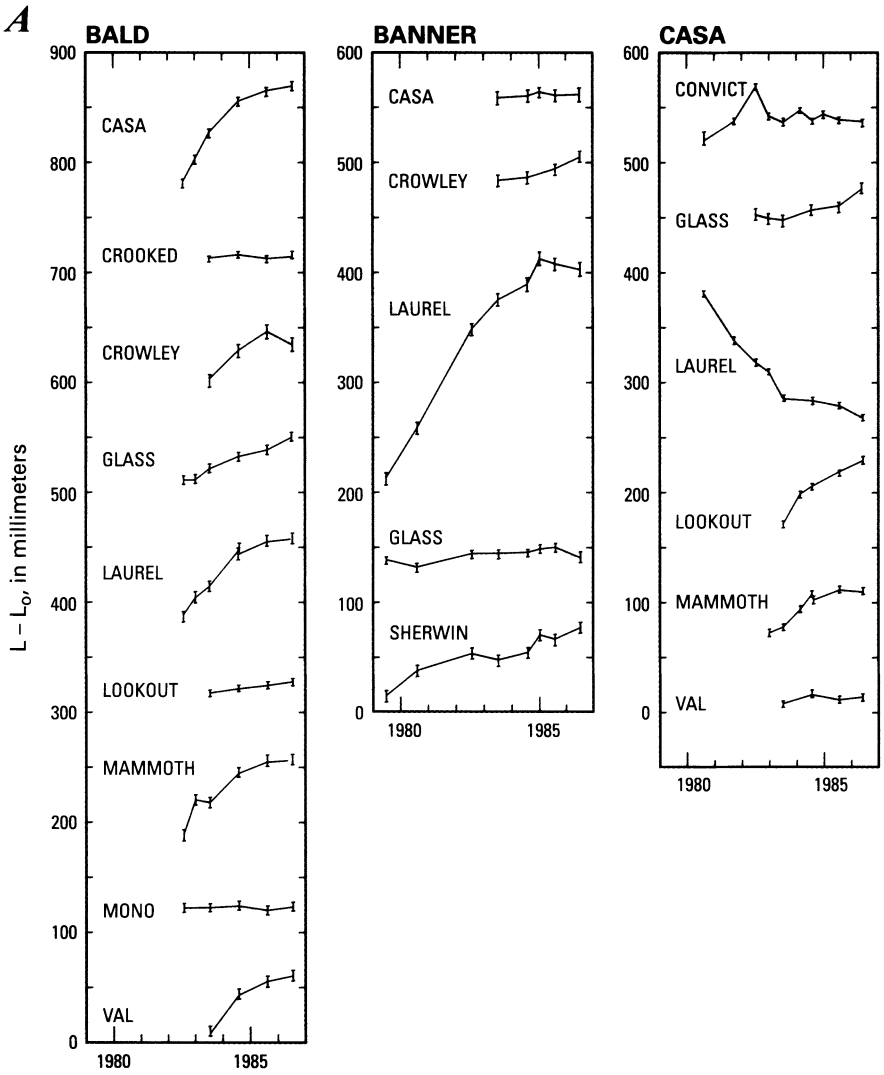

Figure 7.44. Line-length changes in the Long Valley trilateration network measured by annual Geodolite surveys, 1979 to 1986 (Savage *et al.*, 1987). (A) Lines measured from instrument stations BALD, BANNER, and CASA. (B, *opposite*) Lines measured from instrument stations CONVICT, CROOKED, CROWLEY, GLASS, HORSE, LAUREL, LOOKOUT, and MAMMOTH. See Figure 7.43 for station locations. Measured length less a constant nominal length is plotted for each line as a function of time. Error bars represent one standard deviation.

(5) a persistent sequence of LP volcanic earthquakes beneath the southeast flank of Mammoth Mountain at depths between 10 km and 30 km; and
(6) accelerated outgassing of CO_2, almost surely of magmatic origin, around the flanks of Mammoth Mountain first noticed when trees began dying in the area during 1990 (Farrar *et al.*, 1995; McGee and Gerlach, 1998b) (Figure 7.48).

Not to be outdone by Mammoth Mountain, Long Valley Caldera caused a brief stir with another earthquake swarm beneath its south moat during January–April 1996. This was followed by a period of major concern starting in July 1997 when south moat seismicity and resurgent dome swelling began to increase exponentially. As was the case prior to the 1989 Mammoth Mountain swarm, the deformation rate within the caldera began to increase as much as 2 months prior to the onset of earthquake swarm activity in July 1997 (Figure 7.49). By mid-November, the extension rate across the resurgent dome had reached $\sim 36\,\mathrm{cm\,yr^{-1}}$ ($\sim 1\,\mathrm{mm\,day^{-1}}$). Seismicity peaked on 22 November at $\sim$1,000 $M \geq 1.5$ earth-

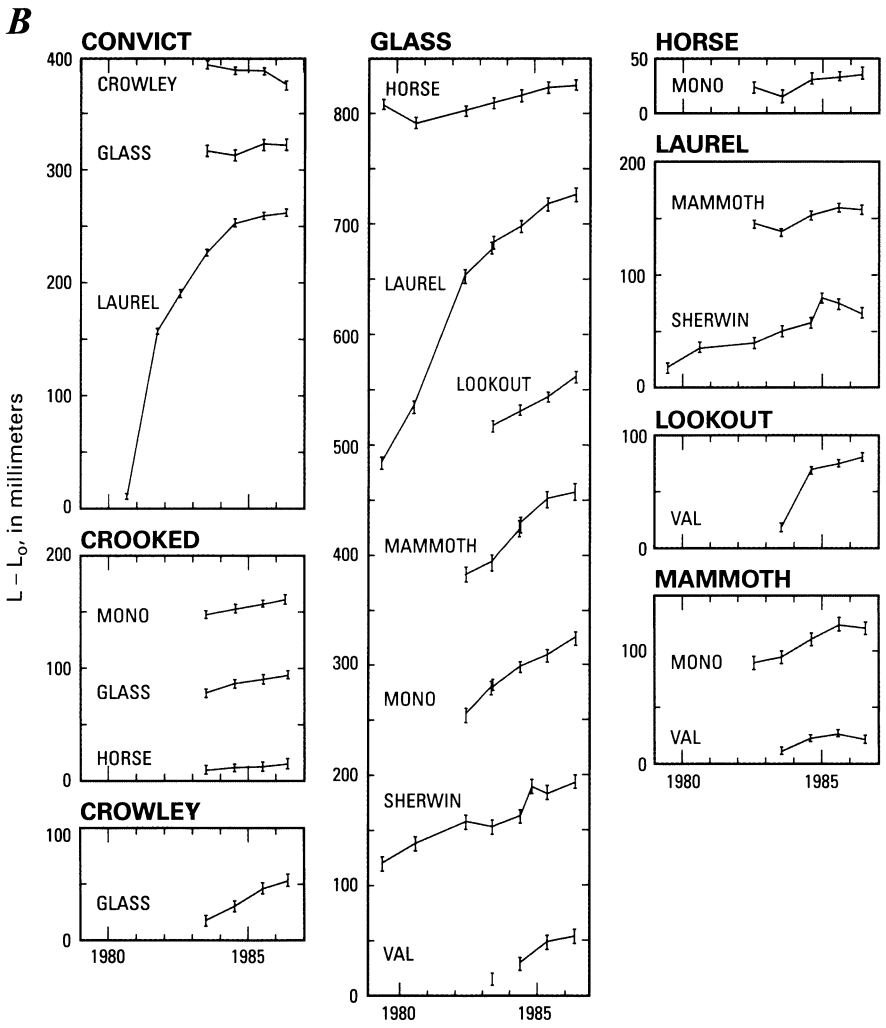

quakes day^{-1}, including $M = 4.6$, 4.9, and 4.6 events. The swarm earthquakes were concentrated in a 1-km-wide, east–west-striking lineation beneath the western part of the south moat (Prejean *et al.*, 2002; Hill *et al.*, 2003). The extension rate began to decay in early December 1997, but earthquake activity surged again at the end of December and early January 1998. By the time activity dropped to background levels in late March 1998, the resurgent dome had extended by an additional 10 cm and the cumulative number of $M \geq 1.5$ earthquakes exceeded 6,000, including 8 $M \geq 4.0$ events. Hill *et al.* (2003) concluded that the 1997–1998 episode was caused by intrusion of magma or magmatic brine beneath the south moat and that the associated earthquake swarm was largely driven by the intrusion process.

Another period of heightened activity in the region began on 9 June 1998, with a M 5.2 earthquake at the southern margin of the caldera just 2 km west of the point where the surface trace of the Hilton Creek fault intersects the caldera boundary. A typical aftershock sequence was interrupted by a second M 5.2 earthquake on 15 July, followed by another aftershock sequence. The third and largest earthquake in the series, a M 5.6 event on 15 May 1999, also was followed by an aftershock sequence and, like the earlier M 5.2 events, it was not accompanied by any response from the caldera. Hill *et al.* (2003, p. 190) concluded that '*... this sequence of M 5 earthquakes has a decidedly "tectonic" character*' and '*... the earthquakes within this Sierra Nevada sequence appear to be high-frequency, brittle-failure events with no evidence for active fluid involvement in the source process.*' Clearly, not all earthquake swarms near volcanoes have

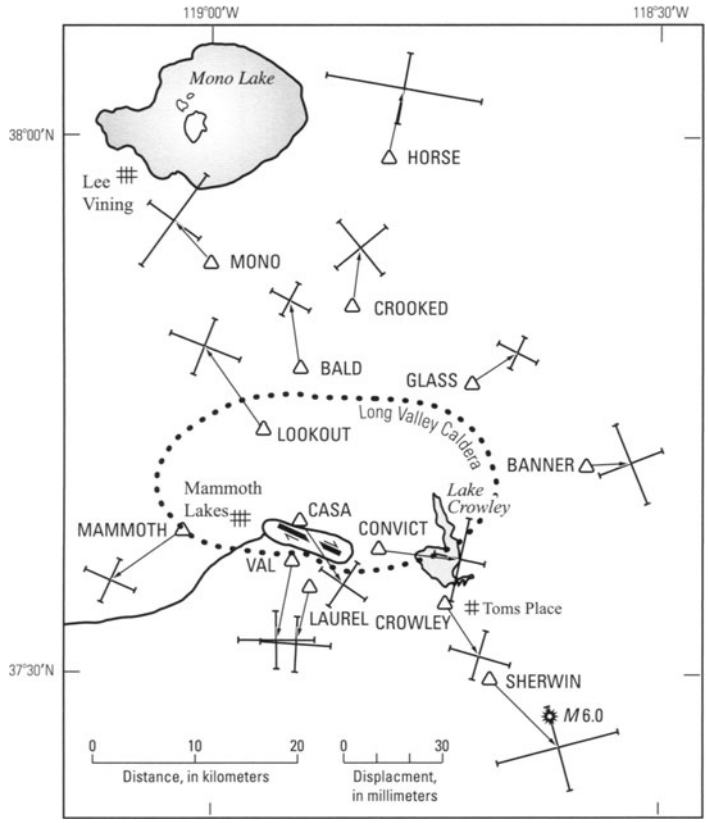

Figure 7.45. Station displacements from 1983 to 1985 determined by annual trilateration measurements (Savage *et al.*, 1987). Error bars represent the principal axes of the 95% confidence ellipse for each displacement vector. Also shown are the trace of an inferred fault in the south moat of the caldera (strike-slip symbol) and the epicenter of the 23 November 1984, *M* 6.0 Round Valley earthquake (sunburst symbol, lower right).

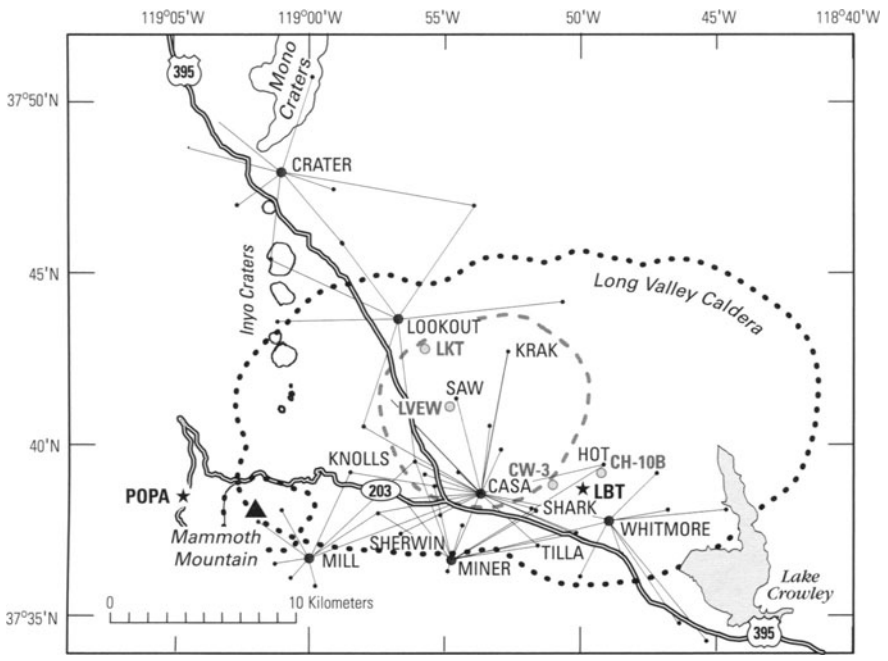

Figure 7.46. Two-color EDM network at Long Valley Caldera and Mono-Inyo Craters (Hill *et al.*, 2002a). Large black dots, instrument sites; small black dots, reflector sites. Baselines radiating from CASA are measured several times per week, weather conditions permitting; others are measured monthly or annually. Stars represent the Devils Postpile borehole strainmeter (POPA) and a long-base (0.5 km) Michelson long-base tiltmeter (LBT). Shaded circles mark the locations of four wells that have exhibited water level changes in response to earthquakes (CH-10B, CW-3, LKT, and LVEW).

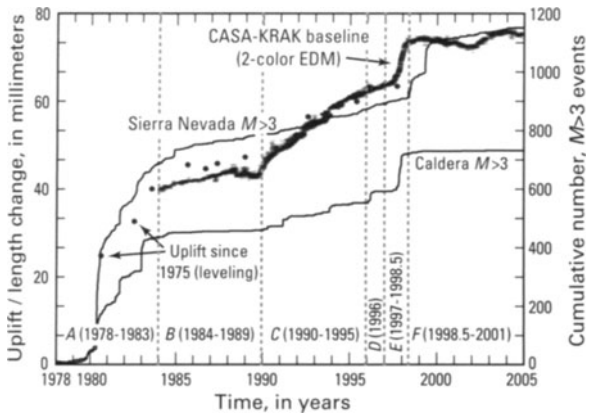

Figure 7.47. History of earthquake activity and swelling of Long Valley's resurgent dome from 1978 through 2004, updated from Hill *et al.* (2002a). Thin lines show the cumulative number of $M \geq 3$ earthquakes within Long Valley Caldera (Caldera $M \geq 3$) and within the Sierra Nevada block to the south (Sierra Nevada $M \geq 3$). Filled circles represent the uplift history of a bench mark near the center of the resurgent dome (i.e., near the intersection of lines 4 and 5 in Figure 7.38) from leveling surveys in 1980, 1982, 1983, 1985--1988, 1992, 1995, and 1997. Thick line shows the amount of extension of an 8-km-long baseline between CASA and KRAK (Figure 7.46) since 1983 based on frequent two-color EDM measurements.

the same origin, and careful detective work is needed to decipher their implications for volcanic and earthquake hazards.

7.4.4 Repeated and continuous GPS measurements

GPS has also played an important role in monitoring unrest at Long Valley – both repeated surveys of a regional network and continuous measurements at several sites within the caldera. An intriguing result was reported by Marshall *et al.* (1997), who showed that annual GPS surveys from 1990 to 1994 of a network spanning both Long Valley Caldera and the Mono-Inyo volcanic chain revealed not only caldera inflation ($0.007\,km^3\,yr^{-1}$) and Basin and Range extension (0.15 ± 0.03 ppm yr^{-1} oriented N66°W ± 1°), as expected, but also the possibility of dike intrusion beneath the Mono Craters. Their best-fit model included as much as $6\,cm\,yr^{-1}$ of opening along a north–south trending dike starting at 10 km depth beneath the Mono Craters chain.

CGPS measurements have been made at station CASA on the south side of the resurgent dome since early 1993 and at KRAK on the north side of the dome since late 1994 (Dixon *et al.*, 1997). The 3-D displacement vectors for these two stations originate at a source 5.8 ± 1.6 km beneath the resurgent dome,

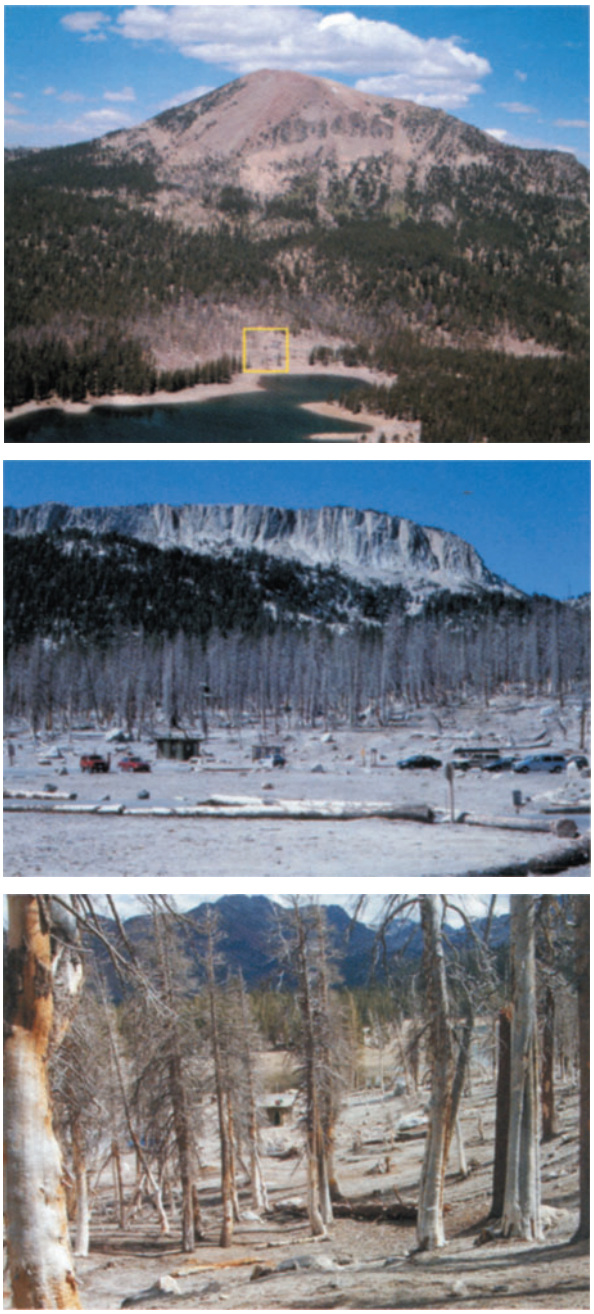

Figure 7.48. Horseshoe Lake tree-kill area, one of several zones of tree mortality around Mammoth Mountain, California, caused by magmatic carbon dioxide leaking from depth along faults and fractures and accumulating in the shallow soil layer. Soil CO_2 concentrations exceed 90% in some locations. (*top*) View looking north--northwest at Horseshoe Lake (foreground) and Mammoth Mountain (skyline); yellow square outlines area shown in middle and bottom photographs. (*middle*) View looking southwest at dead trees and parking area near Horseshoe Lake; CO_2 concentration is monitored continuously both in air inside the small building and in soil outside. (*bottom*) View looking southeast at the same CO_2 monitoring site with dead trees in foreground.
USGS photographs by Michael P. Doukas, August 1999 (*top*) and Kenneth A. McGee, 23 September 1999 (*middle and bottom*).

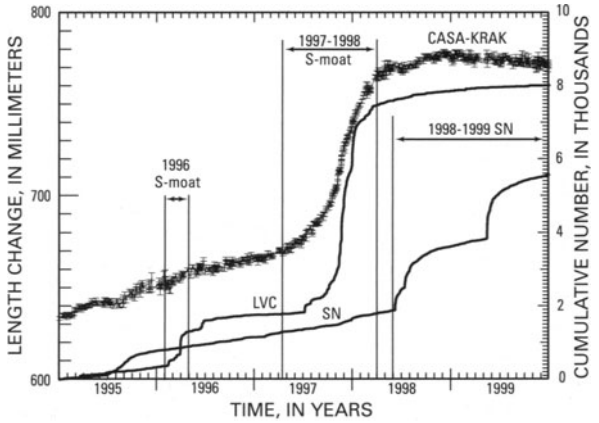

Figure 7.49. Time history of Long Valley resurgent dome inflation for 1995–1999, as represented by: (1) extension of the CASA–KRAK baseline; (2) the cumulative number of $M \geq 1.5$ earthquakes within Long Valley Caldera (LVC); and (3) the cumulative number of $M \geq 1.5$ earthquakes in the adjacent Sierra Nevada (SN) block. Vertical lines bracket the January–April 1996 earthquake swarm in the south moat (1996 S-moat), the July 1997–March 1998 south-moat seismic and deformation episode (1997–1998 S-moat), and the June 1998–May 1999 sequence of three $M > 5$ earthquakes and their aftershocks in the Sierra Nevada immediately south of the caldera (1998–1999 SN). The cumulative seismic moment releases of LVC and SN earthquakes during this time period were M ~5.4 and M ~5.8, respectively. Figure modified from Hill *et al.* (2003). Figure 7.47 shows similar information for 1978–2004.

in good agreement with the models of Langbein *et al.* (1995) and Langbein (2003) based on leveling and two-color EDM observations. Sixteen CGPS stations were operating in the Long Valley area in 2004. A subset of these include real-time, epoch-by-epoch automated data processing that promises to greatly expand the role played by CGPS in volcano monitoring (Endo and Iwatsubo, 2000).

As many as 30 additional CGPS stations and 15 borehole strainmeters will be deployed in the Long Valley area as part of the Plate Boundary Observatory (PBO). PBO is a component of the ambitious EarthScope project, which received initial funding in 2003. EarthScope is designed to investigate the structure and evolution of the North American continent and the physical processes controlling earthquakes and volcanic eruptions. In addition to PBO, the major components of EarthScope are USArray (United States Seismic Array), SAFOD (San Andreas Fault Observatory at Depth), and InSAR. Additional information about this major Earth science initiative, which promises a quantum leap in our understanding of continental structure, earthquakes, and volcanoes, can be found in reports by the US National Research Council (2001a,b) and in the scientific literature as the project unfolds.

7.4.5 Temporal gravity changes

A compelling case for magma intrusion beneath the resurgent dome at Long Valley can be made from the deformation data alone, but additional confirmation is available from repeated gravity surveys. Recall from Chapter 2 that the gravitational acceleration at any point on the Earth's surface depends on both surface elevation and subsurface mass distribution. It follows that, if elevation changes are measured independently and their effects are removed, any residual gravity changes can be attributed to subsurface mass changes. A complication arises, however, if part of the mass changes are caused by changes in groundwater level. If these, too, are measured and their effects are removed from the gravity data, what remains is a direct and rather elegant measure of additional subsurface mass changes.

The results of such an analysis for the Long Valley Caldera were initially presented by Battaglia *et al.* (1999) and later refined by Battaglia *et al.* (2003a,b). After correcting for the effects of uplift and water table fluctuations, Battaglia *et al.* (2003b) found a positive residual gravity change of up to 59 ± 19 μGal centered on the resurgent dome for the period from 1982 to 1999. The data are fit well by a vertical prolate ellipsoid centered 5.9 km beneath the resurgent dome with a volume change of 0.105 km^3 to 0.187 km^3 and a density of 1,180 $kg\,m^{-3}$ to 2,330 $kg\,m^{-3}$. This result excludes *in situ* thermal expansion or pressurization of the hydrothermal system as the primary cause of surface uplift, and confirms the intrusion of magma beneath the caldera since the onset of unrest in mid-1978. In a cautionary note, Battaglia *et al.* (2003b) stressed the importance of using an accurate source geometry for studies of this type. Relative to the best-fit prolate ellipsoid, a point source biased the source depth estimate by 2.9 km (a 33% increase), the volume change by 0.019 km^3 (a 14% increase), and the density estimate by 1,200 $kg\,m^{-3}$ (a 40% increase). Even so, the results are unequivocal. Magma, not water, is primarily responsible for surface uplift and other symptoms of unrest at Long Valley.

A similar study at Yellowstone would be very useful for distinguishing between magmatic and hydrothermal models for surface deformation there (Section 7.3.4). Leveling, GPS, and microgravity observations have been made repeatedly

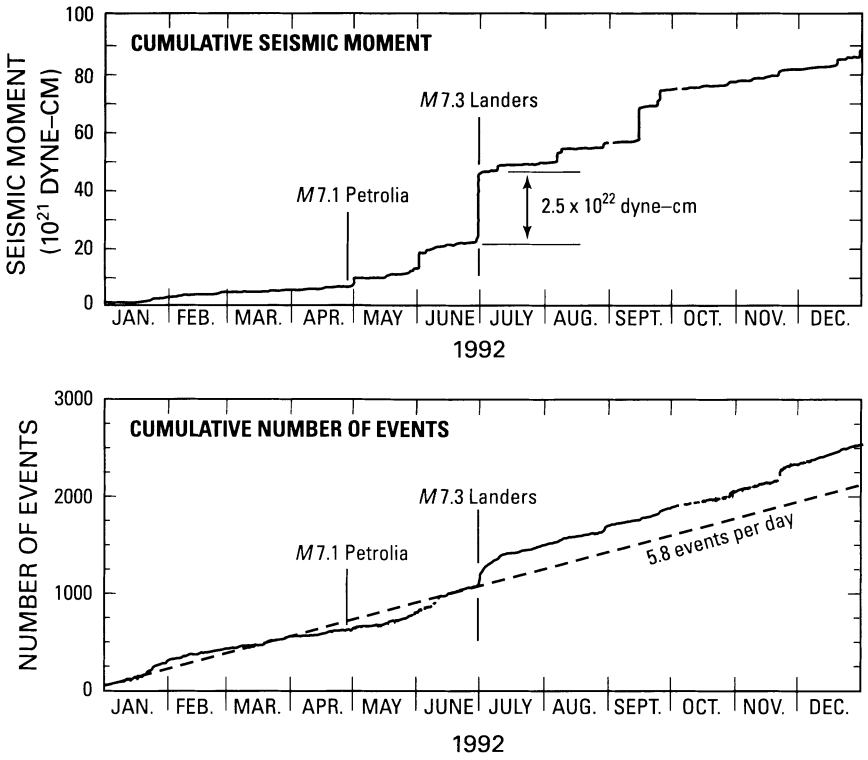

Figure 7.50. (*top*) Cumulative seismic moment for earthquakes near Long Valley Caldera during 1992. Double arrow indicates the cumulative seismic moment for seismicity triggered by the 28 June 1992, *M* 7.3 Landers, California, earthquake. (*bottom*) Cumulative number of earthquakes during 1992 for the same area. Dashed line indicates the average seismicity rate of 5.8 events per day. Vertical lines mark the times of occurrence of the *M* 7.1 Petrolia (Cape Mendocino) and the *M* 7.3 Landers earthquakes (Hill *et al.*, 1995).

at Yellowstone (e.g., Smith *et al.*, 1989; Vasco *et al.*, 1990; Arnet *et al.*, 1997), but the absence of wells suitable for making water-table measurements makes it difficult to constrain the density of fluid involved in historical uplift-subsidence cycles. However, achieving such a constraint would be diagnostic: A source density $\geq 2.3 \times 10^3\,\mathrm{kg\,m^{-3}}$ at a depth >5 km would favor the magmatic model, whereas a source density of $\sim 1 \times 10^3\,\mathrm{kg\,m^{-3}}$ at 3–5 km depth would favor the hydrothermal model. Like Long Valley, Yellowstone is a target for focused study by EarthScope, so exciting new results are likely to be forthcoming soon.

7.4.6 Borehole strainmeter and long-base tiltmeter results: implications of triggered seismicity

What could an earthquake 450 km away from Long Valley possibly tell us about the state of the caldera and the nature of recent unrest? The answer is plenty, and the story might have broad implications for the poorly understood link between regional tectonism and magmatism. The surprising response of Long Valley and 14 other sites scattered across much of the western USA to the *M* 7.3 Landers, California, earthquake of 28 June 1992, forced scientists to reconsider the possibility of long-distance interactions between large earthquakes and magmatic systems. Although the jury is still out, a plausible and particularly intriguing possibility is that large earthquakes can trigger episodic recharge of the deep roots of crustal magmatic systems, either by liquefying a partially crystallized magma body or by inducing deep magmatic intrusion (Hill *et al.*, 1995). This intriguing hypothesis suggests that intensive monitoring of magmatic systems can pay unexpected dividends, especially when the Earth conducts a natural experiment at the scale of the Landers earthquake.

Long Valley responded to the Landers mainshock with a surge in seismicity and a transient strain pulse that began while the S-wave coda and crustal surface waves were still passing through the caldera. The triggered seismicity comprised more than 200 events that occupied the entire seismogenic volume beneath the caldera; the cumulative moment was $2.5 \times 10^{22}\,\mathrm{dynes\,cm^{-1}}$, or the equivalent to a single *M* 3.8 earthquake (Figure 7.50). The POPA borehole strainmeter at the western base of Mammoth Mountain recorded a transient strain pulse that reached peak amplitude of just over 0.2 microstrain (2×10^{-7}) in 6 days, then decayed over the next 10–30 days (Figure 7.51). The seismic slip

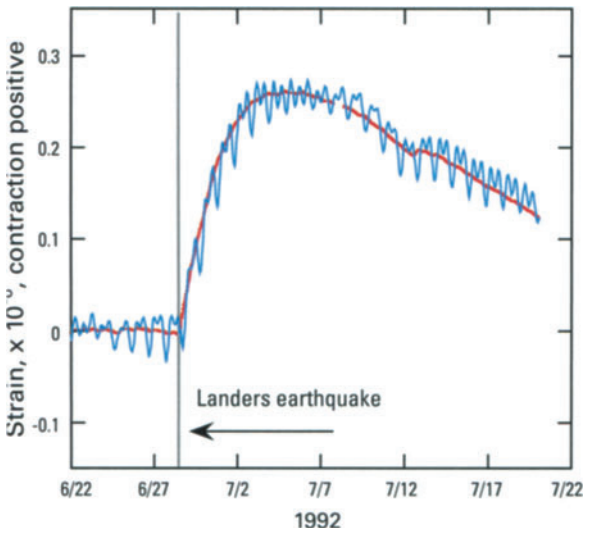

Figure 7.51. Strain transient at Long Valley Caldera triggered by the *M* 7.3 Landers, California, earthquake of 28 June 1992, as recorded by the POPA dilatational strainmeter (see Figure 7.46 for location). Data before (blue) and after (red) removal of tidal and atmospheric-pressure responses are shown. Modified from Roeloffs *et al.* (2003), after Johnston *et al.* (1995) and Hill *et al.* (1995).

represented by the cumulative moment of the triggered seismicity was too small by 2 orders of magnitude to produce the transient strain pulse recorded at POPA (Hill *et al.*, 1995).

How was the Landers earthquake able to trigger a response at Long Valley over a distance of 450 km? The observed coseismic static dilatational strain in the vicinity of the caldera from the Landers mainshock was a 0.006 microstrain (~0.003 bar) compressional step, which is about an order of magnitude smaller than daily tidal stress fluctuations and therefore not a viable mechanism for the triggered seismicity. Peak dynamic stresses,[8] however, were about 3 bars – plausibly large enough to trigger one or more responses at Long Valley (Hill *et al.*, 1993):

(1) Linde *et al.* (1994) suggested that the dynamic waves from Landers triggered a transient pressure increase in one or more magma bodies by advective overpressure (i.e., bubble formation and ascent), which in turn triggered the observed seismicity and strain.
(2) Johnston *et al.* (1995) proposed that the dynamic strains from Landers ruptured compartments of super hydrostatic fluid pressures, which are commonly encountered in volcanic and geothermal regions (Fournier, 1991). They suggested that the result was an upward surge of fluids in the crust beneath the caldera by hydraulic fracturing.
(3) Anderson *et al.* (1994) and Bodin and Gomberg (1994) hypothesized that the shear pulse from Landers initiated aseismic slip on midcrustal faults beneath the caldera, and the associated deformation induced brittle failure at shallower depths.
(4) Hill *et al.* (1995, p. 13,000) reasoned that: '*A magma body with a relatively small melt fraction transmits shear waves from local earthquakes and thus behaves as a solid under small, high-frequency strains. The large, low-frequency strains associated with the shear wave pulse and crustal surface waves from the Landers mainshock may have partially liquefied such a body, thereby releasing some of the differential stress supported by the solid phase. Alternatively, the large dynamic stresses from Landers may have induced a magmatic intrusion by disrupting the cohesive strength of an incipient or partially healed dike adjacent to a crustal or upper mantle magma source.*' According to the authors, either process, occurring at a depth of about 60 km beneath the caldera, satisfies all of the observational constraints.

All of these models explain the essential features of Long Valley's surprising response to the Landers earthquake, but one may be more generally applicable than the others. Most of the seismicity triggered by Landers was concentrated along the margins of the Basin and Range (Hill *et al.*, 1993), where deep zones of basaltic magma are likely drawn into the lower crust as part of the mass balance accompanying crustal extension (Lachenbruch *et al.*, 1976). The relaxing magma body or dike intrusion model (i.e., hypothesis 4 above) thus can account for triggered seismicity at many widely dispersed and seemingly diverse sites, as occurred in Landers' wake. As noted by Hill *et al.* (1995, p. 13,002): '*If this model is correct, it suggests that significant influx of basaltic magma into the deep roots of crustal magmatic systems occurs episodically in response to large, regional earthquakes. This in turn offers a specific link between regional tectonism and magmatism.*' It is a link being forged, at least in part, by practitioners of volcano geodesy.

[8] Peak dynamic stresses accompanied the S-wave (secondary shear wave) and the crustal Love and Rayleigh waves, which have periods of 10 to 20 seconds and wavelengths of crustal dimensions (15–50 km) (Hill *et al.*, 1995).

7.4.7 Water-level changes induced by distant earthquakes: evidence for stimulated upward movement of magma or hydrothermal fluid

Triggered seismicity is not the only response to distant earthquakes that has been observed at Long Valley. Roeloffs *et al.* (2003) reported that water levels in five wells, including the 3-km-deep Long Valley Exploratory Well and four others open to formations as deep as 300 m, responded to 16 earthquakes, both local and distant, from 1989 to 1999 (Chapter 9). Not all of the wells responded to every earthquake, but the responses mostly were consistent from event to event. Water levels in three of the wells always dropped following an earthquake, while in one well the water level always rose. The water-level changes had repeatable time histories from event to event and they generally increased with earthquake magnitude and proximity.

For example, the 1992 M 7.3 Landers earthquake produced water-level changes in all three wells being monitored at that time (Figure 7.52). A gradual water-level drop of ~0.4 m at the LKT well is the largest earthquake-induced change observed there so far (January 2006). The largest seismic event in Long Valley triggered by the Landers earthquake was M 3.7, which is smaller than any of the other local events that produced water-level drops at LKT. So it is unlikely that the post-Landers drop was caused by local triggered seismicity. Instead, Roeloffs *et al.* (2003, p. 283) attributed it to '*... seismic waves from the Landers earthquake itself or to aseismic deformation triggered by those waves.*' They noted that contractional strain that could account for an observed water-level rise at CW-3 is inconsistent with two-color EDM observations. Instead, they (p. 269) attributed the rise to '*... diffusion of elevated fluid pressure localized in the south moat thermal aquifer.*'

Based on careful analysis of the entire dataset for 1989–1999, Roeloffs *et al.* (2003) concluded that earthquake-induced water-level changes in Long Valley could be accounted for by accelerated inflation of the resurgent dome plus localized fluid-pressure increases due to thermal pressurization in the south moat. Inflation of the dome produces extensional strain near the surface, which accounts for water-level drops observed at most of the wells, and thermal pressurization accounts for the observed water-level rises at CW-3. But how could distant earthquakes trigger accelerated

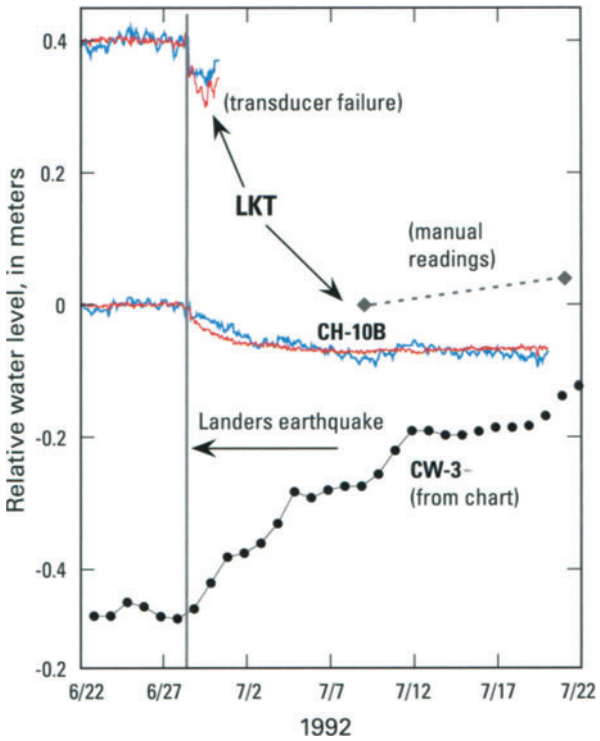

Figure 7.52. Water-level changes in three wells induced by the 1992 M 7.3 Landers earthquake, from Roeloffs *et al.* (2003). Linear trends have been subtracted from the data to minimize water-level variations in the 20 days before the earthquake. For LKT and CH-10B, data before (blue) and after (red) removal of tidal and atmospheric pressure responses are shown. See Figure 7.46 for locations of the wells. The maximum water-level decline at LKT is undetermined because the transducer failed shortly after the earthquake, but a lower bound, based on manual measurements, is 0.396 m.

inflation of the resurgent dome or thermal pressurization in the south moat? Roeloffs *et al.* (2003) noted that most of the locations in the western USA where the Landers earthquake triggered seismicity were geothermal areas (Hill *et al.*, 1993). Roeloffs *et al.* (2003, p. 301) concluded: '*Features at Long Valley that might be preferentially affected by seismic waves include fluid-filled fissures at low effective stress, recently active faults, magma in subsurface reservoirs, dikes or pipes, and young seals in hydrothermal systems. Hot magmatic fluids in the subsurface alter and weaken the rocks at their edges. These weakened rocks could be loosened or cracked by dynamic strains, clearing pathways for fluid movement ... This study provides observational evidence that seismic waves can stimulate hydrothermal systems, that such stimulation is likely related to remote triggering of earthquakes, and that the processes involved can be illuminated by hydrologic monitoring in active volcanic areas.*'

7.4.8 Long Valley summary

With additional leveling and two-color EDM data through 1992, Langbein *et al.* (1995) refined earlier models of Long Valley deformation to include: (1) an ellipsoidal source 5.5 km beneath the resurgent dome; (2) an ellipsoidal source or pipe 10–20 km beneath the locus of earthquake activity in the south moat; (3) a northwest-trending, northeast-dipping dike beneath the southwest part of the caldera; and (4) a dike from 2 to 12 km beneath Mammoth Mountain for the period of the 1989–1990 earthquake swarm. Regional GPS observations suggest another possible deformation source (i.e., dike inflation beneath the Mono-Inyo volcanic chain). With the benefit of several years' more data and additional modeling, Langbein (2003, p. 265–266) concluded: '*... inflation at about 6–7 km beneath the resurgent dome explains most of the deformation detected during two periods of unrest, the 1989–1992 and the 1997–1998 episodes. However, an additional inflation source appears to be required and the data suggest that this poorly resolved source is located in the mid-crust (12–20 km) beneath the south moat ...*' In their introduction to a special issue of the *Journal of Volcanology and Geothermal Research* dedicated to Long Valley, Sorey *et al.* (2003, p. 171) concluded: '*The studies described in this volume and in previous publications lead to the conclusion that both deformation and seismicity in the Long Valley region occur in response to the more fundamental process of magmatic intrusion into the crust. Indeed, episodes of accelerated deformation generally precede increases in earthquake activity by several weeks to months.*' That is music to a volcano geodesist's ears, and ample justification for continued intensive study of this fascinating magmatic–tectonic system.

The picture that emerges from more than two decades of detailed seismic, geodetic, geophysical, and geochemical monitoring at Long Valley is one of complex, space- and time-varying interactions among tectonic, magmatic, and hydrothermal processes. A response plan for volcano hazards in the Long Valley and Mono Craters region has been prepared and will be updated as necessary (Hill *et al.*, 2002a). Regardless of the outcome, the value of an ambitious program of geodetic measurements for monitoring unrest at large silicic calderas has been convincingly demonstrated, as it was several decades earlier for the active basaltic shields of Hawaii.

From basalt to rhyolite, intraplate to convergent margin, persistently active to long dormant, gently effusive to hyper-explosive – the four magmatic systems discussed in this chapter are remarkably diverse. So, too, are the pertinent geodetic datasets. To impose some order, and in hopes of learning more about what makes volcanoes tick, many volcanologists turn to numerical models as interpretive tools. Models are generally better behaved, more easily accessible, and less hazardous than the volcanoes they are intended to emulate. There are simple models, complicated models, forward models, inverse models – a model for every circumstance. Models are the finishing tools in the volcanologist's tool kit. A good one can help turn data into ideas, and ideas into understanding. In the next chapter, a modeling craftsman discusses the tools of his trade and displays a few of his wares. For anyone with a quantitative bent or, like me, with a longing for one, it is a show worth seeing.